FABRICATION AND OPTICAL CHARACTERIZATION OF RARE EARTH SOLIDS FOR QUANTUM APPLICATIONS

by

Dongmin Pak

A Dissertation

Submitted to the Faculty of Purdue University

In Partial Fulfillment of the Requirements for the degree of

Doctor of Philosophy

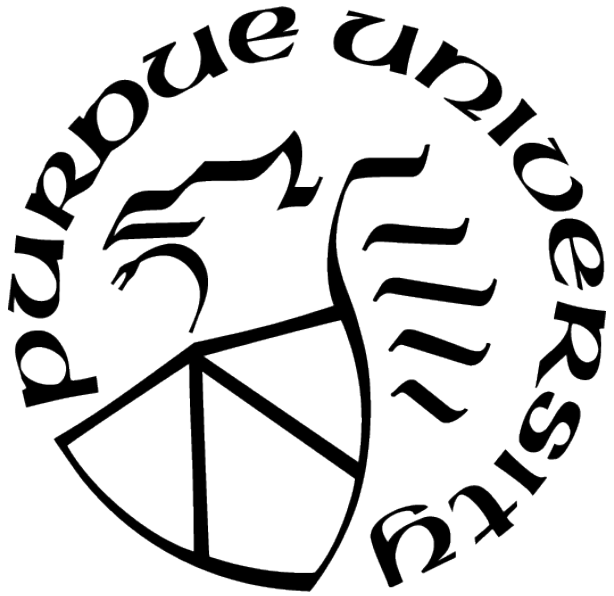

School of Electrical and Computer Engineering

West Lafayette, Indiana

May 2022

THE PURDUE UNIVERSITY GRADUATE SCHOOL
STATEMENT OF COMMITTEE APPROVAL

Dr. Mahdi Hosseini, Chair

School of Electrical and Computer Engineering

Dr. Minghao Qi

School of Electrical and Computer Engineering

Dr. Sunil Bhave

School of Electrical and Computer Engineering

Dr. Chen-Lung Hung

Department of Physics and Astronomy

Approved by:

Dr. Dimitri Peroulis

Dedicated to my family

ACKNOWLEDGMENTS

First and foremost, I would like to thank my Ph.D. advisor, Professor Mahdi Hosseini for his support and guidance during my Ph.D. studies at Purdue. I have learned a lot of valuable lessons from him, which helped me cultivate the ability to think independently. Through his guidance, I have learned how to define and approach problems, and how to solve them. Whenever I am lost and don't know where to go, he always has encouraged me to think about various ways and directed me to the correct path. Not only academic-wise but also personally, he has been a respectful person. For the last 5 years working with him, I personally have had a lot of ups and downs but he has always tried his best to keep me motivated. Also, whenever we had a disagreement on some issues, he made sure my voice was heard. Without his support and guidance, I would not have been able to finish the degree.

Along with Professor Hosseini, I also would like to thank my Ph.D. advisory committee members: Professor Minghao Qi, Professor Sunil Bhave, and Prof. Chen-Lung Hung for their valuable comments and advice that made my Ph.D. dissertation more logical and solid. Each of their valuable comments from their backgrounds made me think outside the box, which greatly helped me fill the weaknesses of my dissertation.

I also would like to thank Professor Yi Xuan. He patiently taught me basic yet critical lessons on nanofabrications, when I first strated to learn them. Also, whenever I encountered difficult problems in terms of fabrications and asked for his opinions, he has always been willing to give his opinions and suggestions.

I am also grateful to Professor Hadiseh Alaeian for enlightening discussions on the theory of collective emission. With her comments and suggestions, I was able to build huge theoretical backgrounds on my experiment.

I would like to express my gratitude to my lab colleagues in Professor Hosseini's group. They were always open to discussions and never hesitant to give constructive comments on my research. Therefore, I would like to thank all of them: Xiaodong Jiang, Haechan An, Yisheng Lei, Arindam Nandi.

I also would like to thank my collaborators at Sandia National Laboratories. It was a great privilege to work with Dr. Michael Titze and Dr. Edward S. Bielejec.

I have spent countless hours in the cleanroom to conduct my experiments at Birck Nanotechnology Center. Therefore, I cannot skip thanking all the staff members of Birck Nanotechnology Center. Whenever I had to develop a new recipe or had problems with fabrication jobs or paper works, they were always open to discussions and not hesitant to share their expertise. Therefore, I would like to thank Dr. Joon Hyeong Park, Dr. Justin Wirth, Richard Hosler, Dan Hosler, Dave Lubelski, Francis Manfred, Tim Miller, Bill Rowe, Kenny Schwartz, Kyle Corwin, Brenda Meador, Lisa Strauser, Mary Jo Totten, Lorraine Fox and all the other people at Birck for their technical support and help.

I also would like to express my gratitude to all of my friends around me in the U.S. and Korea. Whenever I had a hard time or felt lonely during my Ph.D. studies, they have always supported and encouraged me. Thanks to them, I was able to stay healthy physically and mentally, and I could successfully finish my degree at Purdue. I therefore would like to thank Dr. Jinhyun Noh, Woohyun Park, Dr. Doosan Back, Dr. Jiseok Kwon, Dr. Wonil Chung, Dr. Yunjo Lee, Dr. Sungyong You, Bonhyun Ku, Do Woo Kwak, Seongyeop Jeong, Jihoon Cha, Woohoon Jeong, Taehee Lee, Geun Il Kim, Hyungyu Lee, Dr. Sungwon Park, Sangheon Nam.

Last but not least, I would like to deeply thank my family for their support. Dad, Mom, and Sister, without your support, I would not have been able to study what I wanted until now. I would like to thank them for believing in me and giving me unconditional love and support. Therefore, I would like to devote my Ph.D. work to my family.

TABLE OF CONTENTS

LIST OF TABLES

LIST OF FIGURES

LIST OF SYMBOLS

α	absorption rate
β	branching ratio
Γ_0	ion natural decay rate
γ	non-resonant decay rate
τ_{nr}	non-resonant lifetime
τ_r	resonant lifetime
μ	dipole moment
$\mathcal{N}(\theta, \omega)$	angular distribution of atoms
κ	photon decay rate
κ_{e}	coupling loss rate
κ_0	intrinsic loss rate
κ_c	bare intra-cavity loss rate
λ	wavelength
λ_L	wavelength where the light is commensurate with the atomic lattice
$\Delta\lambda_{\mathrm{in}}$	width of inhomogeneous broadening of ions
C_a	mean atom-atom coupling
d	atom spacing
E_{peak}	peak electric field amplitude
$E(r_{yb})$	electric field amplitude at the position of the ytterbium ions
F_P	Purcell factor
g_0	atom-photon coupling parameter
M_s	number of ion segments in the ring
$n_{\mathrm{e}ff}$	effective refractive index
n_g	group index
$N_{\mathrm{e}ff}$	effective number of excitations
N	number of ions
Q_L	loaded quality factor
$Q_{\mathrm{in}t}$	intrinsic quality factor

T_{min}	minimum transmission
V_0	mode volume of cavities
Y_{Tm}	implantation yield factor of Tm ions after annealing

ABBREVIATIONS

AOM	acousto-optic modulator
BS	beam sampler
CL	commensurate lattice
CW	clockwise
CCW	counter-clockwise
FIB	focused ion beam
FSR	free-spectral range
FWHM	full width at half maximum
HSQ	hydrogen silsesquioxane
ICP-RIE	inductively coupled plasma - reactive ion etching
IDTs	interdigital transducers
LN	lithium niobate
LNOI	lithium niobate on insulator
PMMA	polymethyl methacrylate
PL	photoluminescence
Q factor	quality factor
REIs	rare-earth ions
RESs	rare-earth solids
RT	room temperature
SAWs	surface acoustic waves
SiN	silicon nitride
SRIM	stopping and range of ions in matter
TMAH	tetramethylammonium hydroxide
YSO	yttrium orthosilicate
YAG	yttrium aluminium garnet
YAG	yttrium orthovanadate

ABSTRACT

Rare-earth ions (REIs) in solids are attractive optical centers due to their stable optical transitions and long lifetimes [1], [2]. Miniaturizing solid-state devices incorporated with REIs as quantum centers can play a key role in the implementation of future multiplexed quantum optical networks. Among the solid-state host materials for REIs, the Dissertation specifically studies silicon nitride (SiN) and crystalline lithium niobate (LN) materials.

SiN and Si are a CMOS-compatible material, and leveraging the well-developed technologies from the microelectronics industry is important for practical purposes because the cost of fabrication can be significantly reduced. Also, a recent study showed that the inhomogeneous broadening of Er-doped crystalline Si can be as low as 1GHz [3]. Moreover, low-loss waveguide and high Q resonators were reported [4]–[6], making it a promising host for strong light-atom interactions.

On the other hand, LN is a promising host material for REIs due to its unique piezoelectric, electro-optic, nonlinear, and acousto-optic properties [7]. Until recently, direct etching of LN has not been realized. But recently developed lithium niobate on insulator (LNOI) platform and direct LN etching techniques made it possible to fabricate low loss and strong confinement waveguides [8], [9]. Furthermore, LN has been used for quantum light storage [10] and on-chip photon generation and wavelength conversion [11]. Motivated by these recent advances and the interesting properties of LN, the Dissertation investigates thin-film crystalline LN.

In this dissertation, the methods and processes of fabricating long waveguides and ring resonators in 1)silicon nitride and 2)lithium niobate are introduced and the study of optical characterizations of Yb^{3+} ions in two different solid-state host materials are presented, specifically including photoluminescence (PL) spectroscopy, lifetime measurement, absorption and other characterization of light-atom interactions.

Furthermore, a study of Tm^{3+} ion arrays in thin-film LN is presented, specifically including the PL lifetime comparison between the periodically ordered sample and the randomly ordered sample and the scattering/reflection measurement from periodic ion arrays, both indicating the early evidence of cooperative effects of arrays in solids. Also, the theory of

collective emission from atomic arrays is presented. Finally, I propose future plans to improve the fabrication process in these materials and possible future research directions based on the Dissertation.

1. BACKGROUND AND INTRODUCTION

1.1 Light-atom interaction and its applications

The interaction between atoms and light is important for various applications. Lasers, for example, are good applications of coherent light-atom interactions and among the products we interact with in daily life. Due to the good spatial coherence properties of the laser, the laser beam can be collimated over long distances, enabling applications such as LIDAR, communications, and more. Moreover, due to the high temporal coherence property of the laser, the laser can emit light with a very narrow spectrum, meaning only a specific wavelength of photons (color) can be emitted.

In the quantum domain, the coherent interaction of light with atoms can enable the control of optical and atomic properties. Such interaction enables generating optical qubits [12], storing optical qubits [13] and it can be tailored such that two qubits non-linearly interact with each other [14]. For quantum communication applications, photons which work as a flying qubit require coherent interaction with stationary qubits like atoms to map the encoded quantum coherent states from flying qubits to stationary qubits [15].

Quantum sensing application, which uses quantum entanglement to improve the sensitivity of measurements beyond its classical limits [16], is an important quantum application utilizing coherent light-atom interactions. There are also several other quantum applications utilizing coherent light-atom interactions at the single-photon level. One of the quantum applications which has been actively studied is quantum memory applications. Quantum memories can be developed with linear and non-linear light-atom interactions. For example, quantum memories are building blocks of quantum repeaters used for quantum communication systems. For practical quantum communication networks, a quantum repeater consisting of $\sim$100 memories per node with a storage time on the order of $\sim$sec is required [17]. Storage time in atomic memory is defined by the coherence time or inverse of the dephasing rate of its atoms. Recently, ultra-long coherence time on the order of hours has been reported using europium in yttrium orthosilicate (YSO) crystal at 2K [18]. For efficient memory applications, the impedance-matched cavity protocol has been studied [19] and for on-demand storage, external electric fields have been used to control the storage process [20].

The solid-state implementation of light-atom interactions is essential to realize practical integrated quantum systems. In this way, multiple quantum blocks, such as memories and gates can be integrated within the same chip.

Among various quantum emitters such as defect centers and quantum dots, In the Dissertation, I am specifically interested in rare-earth ions (REIs). This is due to the various advantages that REIs have, including long coherence time [18], high quantum storage efficiency [20], large quantum storage bandwidth (about 50GHz), [21] and telecom-compatible (C-band) operation [13].

1.2 Rare-earth ions in solids

1.2.1 Properties of rare-earth ions in solids

Rare-earth elements are a group of elements that share similar chemical and physical properties. The similar chemical and physical properties shared by REIs are derived from the shared electron configuration of $[Xe]4f^N6s^2$ where N is an integer value from 1 to 14.

When electrons are filled in the orbitals of REIs, 5s,6p,6s orbitals are filled prior to the 4f orbitals because their energy levels are lower than that of 4f orbital, as shown in 1.1.(a). However, since these orbitals are radially bigger than 4f orbital, the outer 5s, 5p, 6s orbitals are electronically shielding the partially filled 4f orbital, as shown in Fig. 1.1.(b). Therefore, this shielding effect results in an insensitive atomic structure to the local environment, making REIs attractive optical emitters.

For quantum applications, REIs are usually doped into solid-state crystals, such as yttrium orthosilicate (YSO) or yttrium aluminum garnet (YAG), or lithium niobate (LN) et cetera. With the ability of miniaturizing solid-state quantum devices, system integration and multiplexing of devices can be realized. When doped into the solids, the energy levels of REIs are slightly affected because of the crystal field by the hosts, but most of the properties of the free REIs remain the same [22].

When ions are doped into crystals, individual ions will experience variations in the local environment. Each individual ion has a characteristic linewidth, which we call the homogeneous linewidth (Γ_h). When the ion ensemble is considered, the absorption profile is the sum

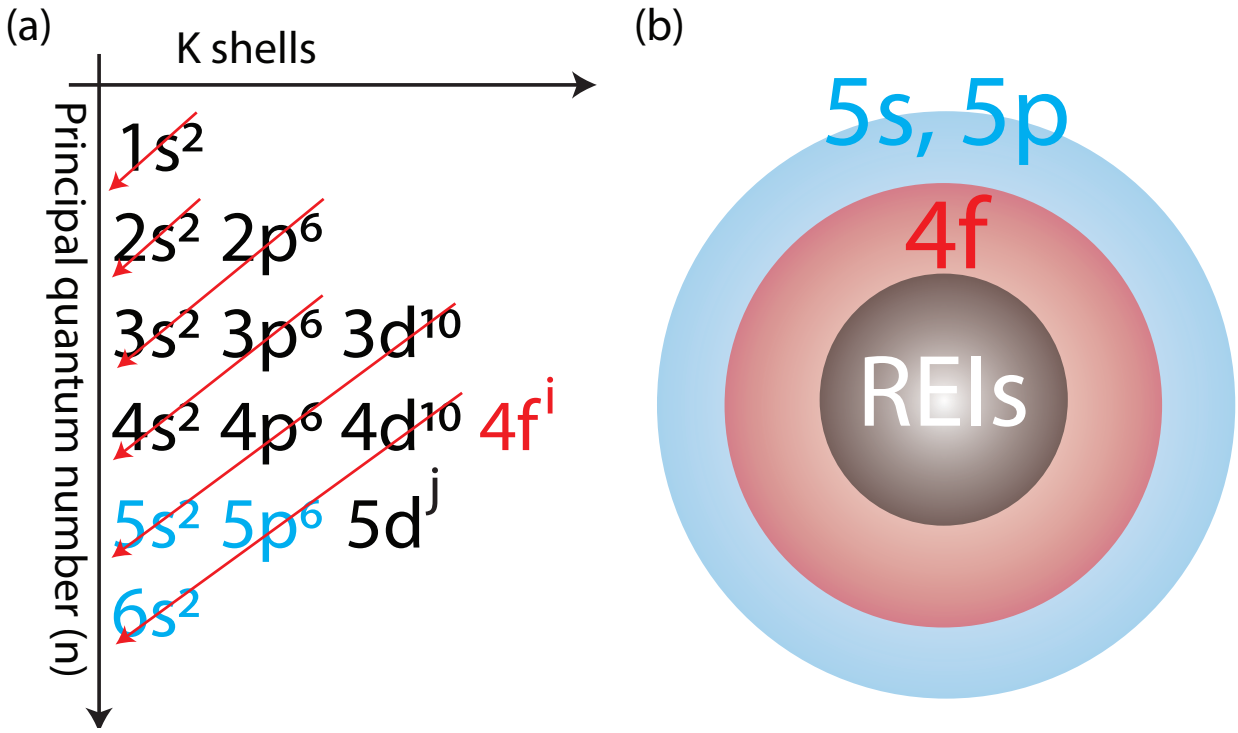

Figure 1.1. (a) the filling order of electrons to each orbital, illustrated by the red arrows; (b) Schematic orbital structure of rare-earth ions. The partially filled 4f orbital is shielded by the outer 5s,5p orbitals

of the homogeneous linewidth of each individual ion experiencing slightly different variations (e,g, different lattice locations), which we call the inhomogeneous linewidth (Γ_{inh}).

For example, the Fig. 1.2 shows the energy levels of Er^{3+} ions when doped into YSO crystal. The Er^{3+} ion has a transition at 1.54µm, compatible with the telecom C-band. First, the crystal field, caused by the surrounding environment of ions, lifts all the eight degeneracies with a transition frequency of THz range. The Kramers doublets can be further lifted by external magnetic fields. This results in Zeeman splitting, which shows a GHz range of transition frequency with the field on the order of 100mT. The odd isotope ^{167}Er with a natural abundance of 22.9% lifts additional 8 states from the spin 1/2 transition, which is due to the additional nuclear spin of 7/2 [23].

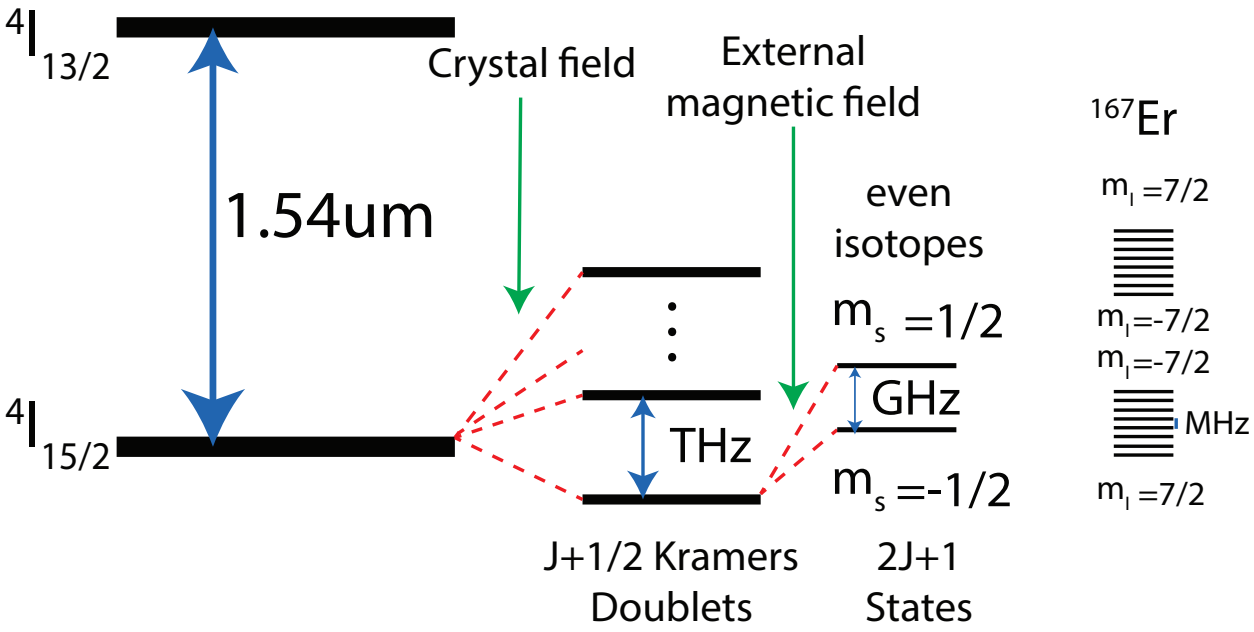

Figure 1.2. Energy level structure of Er^3 ions doped into YSO crystal and the degeneracies are lifted

1.2.2 Lifetime and Coherence time

Throughout this dissertation, the lifetime (T_1) and the coherence time (T_2) of REIs will be discussed, which both are decay mechanisms that can corrupt a quantum state. So it is worth noting the definition of lifetime and coherence time at this point.

The lifetime, which is also called the longitudinal homogeneous lifetime, is mainly associated with the population decay of the excited state. Since the atoms in the excited state have a spontaneous tendency to decay to lower levels, the total number of atoms*(1/e) in the excited state decays to the ground state after T_1 time. The T_1 time can also be written as the equation 1.1

$$\frac{1}{T_1} = \frac{1}{T_R} + \frac{1}{T_{NR}} \tag{1.1}$$

where T_R and T_{NR} denote the radiative and non-radiative decay times. Unlike radiative decay, where atoms emit photons while decaying to the ground state, in the non-radiative decay process, the atoms release small vibrational energy, so-called phonon.

However, the coherence time (T_2), which is also called the transverse homogeneous lifetime, is mainly associated with the dephasing of the state. Dephasing can happen by two mechanisms. One is the population decay and the other is the pure-dephasing rate ($1/T_2'$), not changing the population of the excited state. Therefore, the coherence time can be written as the equation 1.2

$$\frac{1}{T_2} = \frac{1}{2T_1} + \frac{1}{T_2'} \tag{1.2}$$

When REIs are incorporated in solids at room temperature, typically, the pure dephasing rate is much faster than the population decay rate ($T_1 \gg T_2'$). Therefore, the coherence time is mostly determined by pure dephasing scattering processes. So in order to reduce the pure dephasing rate and therefore to have a longer coherence time, cryogenic temperatures are important for quantum applications. The homogeneous linewidth is related to the coherence time T_2 by the equation 1.3.

$$\Gamma_h = \frac{1}{\pi T_2} \tag{1.3}$$

1.2.3 Quantum applications of rare-earth solids

Due to the unique shielding property of REIs, Rare-Earth Solids (RESs) can be used for various quantum applications. Firstly, REIs have been actively studied for quantum memory applications. Record-long 6-hour coherence time and 69% efficiency quantum storage have been reported using europium in YSO crystal and praseodymium in YSO crystal, respectively [18], [20]. Also, the memory operating at a wavelength compatible with a standard telecom

band (C-band), where we can utilize the current infrastructure, has been studied using Er [13].

Among REIs, Yb^{3+} ions specifically can be used for transduction applications. Recently, It has been shown that Yb^{3+} ions in YSO and YVO can coherently interact with both microwave and optical photons, showing the capability of microwave-to-optical transduction [24], [25]. The transduction application is important in that transduction of microwave photons to optical signals can be used for future superconducting quantum computers [26].

1.2.4 Limitations of rare-earth solids

However, REIs also have their inherent limitations. First, because of the forbidden 4f-4f transitions, the dipole transitions between ground states and excited states are weak. While this results in a long coherence time and therefore REIs can be used for various quantum applications, this weak transition strength makes the interaction probability with input photons really low.

Also, efficient hole burning can be challenging in REIs (especially erbium) in solids. This is mainly because the ground state lifetime is comparable to excited state lifetimes [27], as one can see from the Fig. 1.3.(a). This results in pumping atoms to a particular ground state difficult. Therefore, state preparation in a single ground state, which is necessary for many memory protocols, is difficult in REIs and we cannot take full advantage of many-atom systems.

The third limitation is not the limitation of REIs themselves, but it occurs when they are incorporated into the bulk crystals. The typical crystalline bulk hosts such as YSO, LN are not fabrication friendly and are known as hard-to-etch materials [27], [28]. Therefore, the bulk crystals are not optimal for integration with other optical devices in wafer-scale, which is essential to build multiplexed systems.

1.3 Device integration with cavities and miniaturization

In order to overcome the limitations associated with low interaction strengths, cavities can be implemented into the system. With cavities having a small mode volume, we can

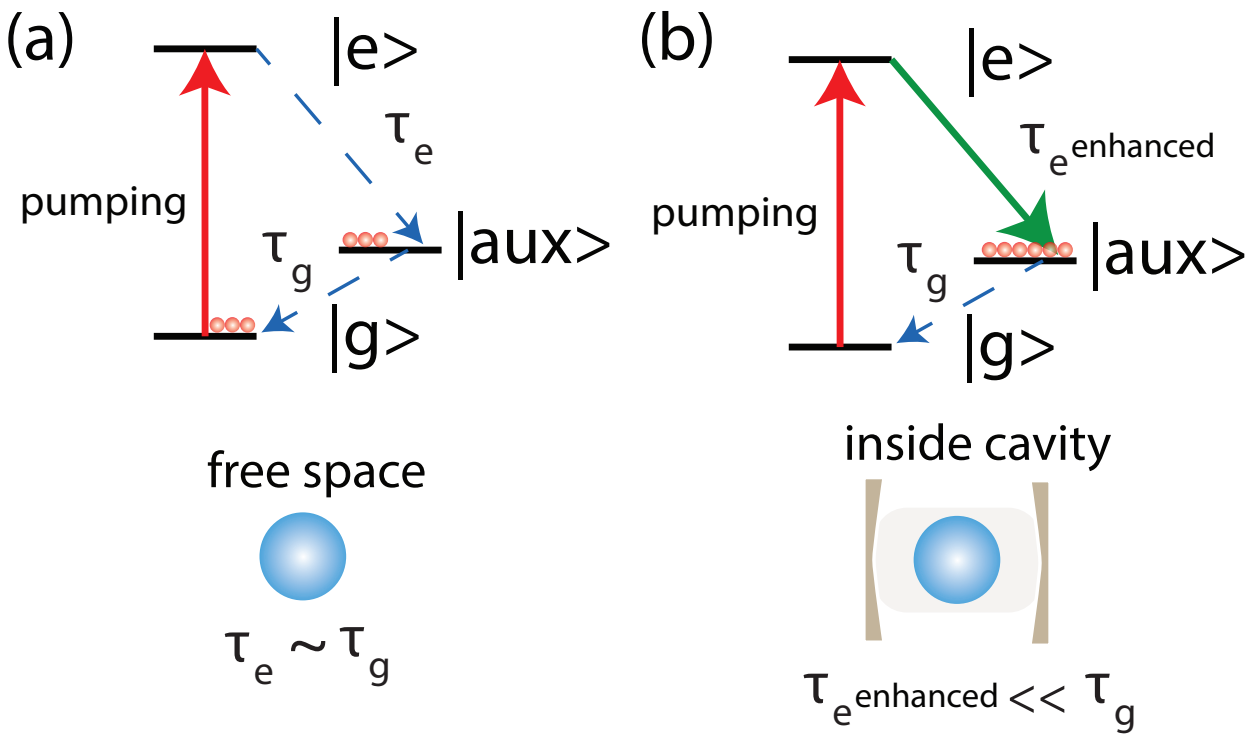

Figure 1.3. Energy level structure of Er^3 ions doped into YSO crystal and the degeneracies are lifted

increase the atom-photon coupling rate. Also, the lifetime of atoms in a cavity can be modified by the Purcell effect, which helps the preparation of many atoms in a single state of REIs, as shown in Fig. 1.3.(b). I would like to give more detailed explanations of how the implementation of cavities can mitigate the limitations of REIs.

I would like to first explain how cavities help state preparations. The Purcell effect is known to shorten the excited state lifetime. The reduced lifetime is due to the interaction with a high Q cavity. The spontaneous emission rate of the excited state is governed by Fermi's golden rule and is proportional to the density of states of the coupled radiation field. By modifying the local density of states by the cavity resonance, the spontaneous emission rate can be modified in the cavity.

Here I would like to provide a more detailed description of the Purcell factor based on Refs. [29], [30]. Multidimensional decay of rare-earth ions in microphotonics [30] provides

a complete picture to describe the Purcell factor in all dimensions. The maximum Purcell factor [29] with a D-dimensional mode confinement can be described as :

$$F^{(D)} = \frac{3}{4\pi^{D-1}}(\frac{\lambda}{n})^{D}\frac{Q_D}{V_D} \tag{1.4}$$

where the mode volume, V_D, can be calculated by the equation 1.5.

$$V_D = \frac{\int \epsilon|E(r)|^2 dV}{max\left(\epsilon(r)|E(r)|^2\right)} \tag{1.5}$$

The experimentally measured Purcell factor, $F^{(e)}$, will be lower than this maximum value, if 1) the position of the atom, r_0, is different from the location of the maximum field, r_m and/or 2) the dipole moment, μ, is misaligned with the local electric field $\overrightarrow{E}(r_0)$. Here, r_m refers to the position where the mode field energy density, $\epsilon(r)|E(r)|^2$, is maximized. Therefore the experimental Purcell factor, in this case, is described as :

$$F^{(e)} = F^{(D)} f(r_0) cos^2\theta \tag{1.6}$$

where θ is defined as the angle between μ and $E(r_0)$ and $f(r_0)$ is demonstrated as:

$$f(r_0) = \frac{\epsilon(r_0)|E(r_0)|^2}{\epsilon(r_m)|E(r_m)|^2} \tag{1.7}$$

The atomic dipole is depolarized by decoherence processes during the atom-mode coupling and therefore the Purcell factor is indirectly influenced by it through the $\cos^2\theta$ term. Here, a degree of polarization Θ ($0 \leq \Theta \leq 1$) is introduced to quantify the degree to which the atom maintains its initial dipole direction during its lifetime. For a structure with 1D, 2D, and 3D Purcell effects and with modes polarized along the x, y, and z directions, the

total Purcell factor can be given by a sum of contributions over 1D, 2D, and 3D dimensions and modes [29]:

$$F = \frac{1}{3}\sum_{D=1}^{3}\sum_{\mathrm{i,j},k}[F_{\mathrm{i}}^{D,x} f_{\mathrm{i}}^{D,x}(r_0)(1-\Theta) + F_{\mathrm{j}}^{D,y} f_{\mathrm{j}}^{D,y}(r_0)(1+2\Theta) + F_{k}^{D,z} f_{k}^{D,z}(r_0)(1-\Theta)] \quad (1.8)$$

where $F_{\mathrm{i}}^{D,x}$ represents the maximum Purcell factor for the i-th order mode in D-dimension, polarized along the x direction. This equation is based on the assumption that the 1D, 2D, and 3D Purcell effects are independent of each other.

The implantation depth distribution u(y) can be approximated as an average position y_0 for each polarization of modes. Therefore, y_0 can be calculated as:

$$y_0^{\mathrm{i}} = \frac{\int \epsilon(y)|E^{\mathrm{i}}(y)|^2 u(y) y dy}{\int \epsilon(y)|E^{\mathrm{i}}(y)|^2 u(y) dy}, \mathrm{i} = TM_0 \ or \ TE_0 \quad (1.9)$$

where $\epsilon(y)$ and $E^{\mathrm{i}}(y)$ are the values of $\epsilon(r)$ and $E^{\mathrm{i}}(r)$ at x = z = 0. Neglecting the Purcell effects from higher order modes, the equation 1.8 can be simplified as [29], [30].

$$F_m = (F_p^1 + F_p^2 + F_p^3) f_p(y_o^p)(1+2\Theta)/3 + (2F_q^1 + F_q^2 + F_q^3) f_q(y_o^q)(1-\Theta)/3 \quad (1.10)$$

where p $\equiv TM_0$ and q $\equiv TE_0$. Here, F^1 and F^2 are independent of temperature, while F^3 contains the homogeneous linewidth of the ion, Γ_H(T). In the Dissertation, due to the low mode confinement in the waveguide cross-section, the effect of F^1 and F^2 are negligible and F^3 (or cavity) has the main effect on the Purcell factor. As a result, the Purcell factor is temperature-dependent [30]. It has been demonstrated that γ^*(T) $\propto$ $\mathrm{T}^{1.8}$ at high temperature due to the coupling to phonons and γ^*(T) $\propto$ $\mathrm{T}^{1.3}$ at low temperature due to coupling to tunneling systems and the crossover happens around 40K [31], where γ^* is a pure dephasing rate.

Specifically, the quality factor for 3D confinement (cavity) used in the Purcell factor equation (Eqn. 1.4) is given by :

$$Q^{3D} = \frac{\omega_c}{2\gamma_{total}} \tag{1.11}$$

where $\gamma_{total} = \kappa + \gamma + \gamma^*$, κ is the cavity decay rate , γ is the atom relaxation rate and γ^* is a pure dephasing rate.

For rare-earth ions at room temperature, the ions' homogeneous linewidth is much greater than the cavity linewidth, κ, and it suppresses the Purcell effect. At cryogenic temperatures, the homogeneous broadening or the dephasing rate is expected to significantly narrow. When $\gamma^* \ll \kappa$, the Purcell factor can be fully recovered. Such temperature dependent Purcell effect has been observed for rare-earth ions [30], [32]. Therefore, the Purcell effect is expected to suppress at room temperature (~300K) due to the increased homogeneous linewidth of rare-earth ions.

With the general equation of the Purcell factor (Eqn. 1.4), we confirm that the Purcell factor is proportional to the ratio of the quality factor to the mode volume. Therefore, cavities with a higher quality factor and a small mode volume will demonstrate a higher Purcell factor.

As a result, the excited state lifetime resonant with the cavity is reduced by $1/F_P$ compared to that of free-space. Therefore, unlike the free-space case where the preparation of many atoms in a single state is difficult (Fig. 1.3.(a)), Inside the cavity, many atoms can be prepared in a single state as illustrated in the Fig. 1.3.(b).

The other limitation of REIs, the inherent weak transition strength, can also be improved inside cavities. The atom-photon coupling rate, g_0, inside the cavity can be written as equation 1.12.

$$g_0 = \frac{1}{n}\sqrt{\frac{\mu_{12}^2\omega}{2\epsilon_0\hbar V_0}}(|\frac{E(r_{ions})}{E(peak)}|) \tag{1.12}$$

As confirmed by the equation 1.12, the atom-photon coupling rate, g_0, is inversely proportional to the mode volume (V_0). Since the weak transition dipole moment, μ_{12}, is limited by the inherent properties of REIs, by reducing the mode volume of the cavity, the atom-photon coupling rate can be increased. As a result, in order to take advantage of cavities with low mode volume, lots of research has been conducted trying to fabricate miniaturized cavities in the crystal. The photonic nano-cavity, where the mode volume is as low as $0.2um^3$, has been fabricated in bulk Nd:YSO crystal using focused ion beam (FIB) milling technique. [33]. Also, in another approach, the nano-cavity with small mode volume is fabricated on an SOI platform and then the cavity is placed onto the Er:YSO crystal. With this nano-cavity having a high Q and low mode volume, a Purcell factor of as high as 700 is reported [26].

Furthermore, one research showed that a single ion detection is possible in a nano-cavity [34]. The Purcell effect enhances the spontaneous emission rate of the ions. With a high Purcell factor, the spontaneous emission rate of the Nd ions is enhanced to the point that the linewidth of the emitter becomes radiatively limited. As a result, a single Nd ion has been detected in YVO crystal.

Lastly, the lithium niobate on insulator (LNOI) platform, developed using the smart-cut process [35], [36], was recently developed and its direct etching technique was also introduced. This progress has made low-loss, high confinement, and broad-band photonics possible using crystalline LN [28]. Recently, the wafer-scale lithium niobate photonic integrated circuits using the LNOI platform and direct LN etching technique, have been achieved [9]. This recent progress has shown the possibility of scalable and integrated quantum optical devices in wafer-scale, which has been challenging with bulk crystals.

1.4 Basic physics of photonic ring resonators

Throughout this dissertation, lots of discussions about the properties of ring resonators such as transmission, quality factor, coupling, will be listed. Therefore, It would be beneficial to introduce the basic physics of ring resonators in this section. In a simple ring resonator, consisting of a ring and a bus waveguide, as one can see from the Fig. 1.4, there are 3 important parameters. a is the single-pass amplitude transmission, r is the self-coupling

coefficient and k is the cross-coupling coefficient, respectively. r^2 and k^2 are the power splitting ratios of the coupling, and therefore assumed to be $r^2+k^2 = 1$, meaning no losses in the coupling [37]. In the real-life scenario, the coupling loss is not zero, and should be considered, which I will explain later in more detail.

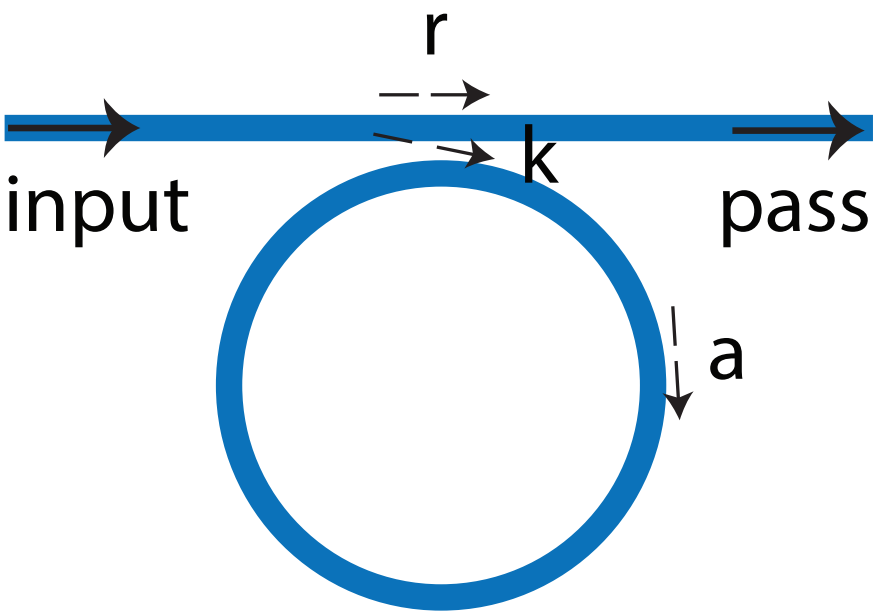

Figure 1.4. A schematic simple ring resonator with the bus waveguide and the ring

The ratio of the transmitted field to the incident field in the bus waveguide can be calculated as in the equation 1.13 [38].

$$\frac{E_{pass}}{E_{input}} = \mathrm{e}^{\mathrm{i}(\pi+\phi)}\frac{a - r\mathrm{e}^{-\mathrm{i}\phi}}{1 - ra\mathrm{e}^{\mathrm{i}\phi}} \tag{1.13}$$

where $\phi = \beta$L is the single-pass phase shift, L is the round trip and β is the propagation constant. Squaring the equation 1.13 gives the transmission intensity T.

$$T = \frac{I_{pass}}{I_{input}} = \frac{a^2 - 2racos\phi + r^2}{1 - 2racos\phi + (ra)^2} \tag{1.14}$$

From the equation 1.14, we can find out that the ring becomes on resonance when the phase ϕ has a value of m×2π, m being a positive integer, or more intuitively

$$\lambda_{res} = \frac{n_{eff} L}{m} \tag{1.15}$$

where n_{eff} quantifies the ratio of the phase delay in a unit length waveguide to the phase delay in vacuum.

When on resonance, the transmission of the resonator is written as

$$T_{res} = \frac{(a-r)^2}{(1-ra)^2} \tag{1.16}$$

where the critically-coupled condition ($T_{res} = 0$) can be achieved by calibrating the gap of the ring and bus waveguide (related to the value of r) and/or attenuation in the ring (related to the value of a). a includes propagation loss and can be denoted as $a^2 = \exp(-\alpha L)$, where the α is the power attenuation coefficient.

When the ring resonator has two bus coupling waveguides, the input field can be partially transmitted to the drop-port (Fig. 1.5) . The transmission from the input port to the pass port (T_P) and from the input port to the drop port (T_d) can be derived as below [37]:

$$T_P = \frac{I_{pass}}{I_{input}} = \frac{r_2^2 a^2 - 2 r_1 r_2 a cos\phi + r_1^2}{1 - 2 r_1 r_2 cos\phi + (r_1 r_2 a)^2} \tag{1.17}$$

$$T_D = \frac{I_{drop}}{I_{input}} = \frac{(1-r_1^2)(1-r_2^2)a}{1 - 2 r_1 r_2 a cos\phi + (r_1 r_2 a)^2} \tag{1.18}$$

In the case when the attenuation is very small (a∼1), critical coupling takes place at symmetric coupling ($k_1 = k_2$). When lossy, critical coupling happens when the losses are matching with the coupling as $r_2 a = r_1$ [37].

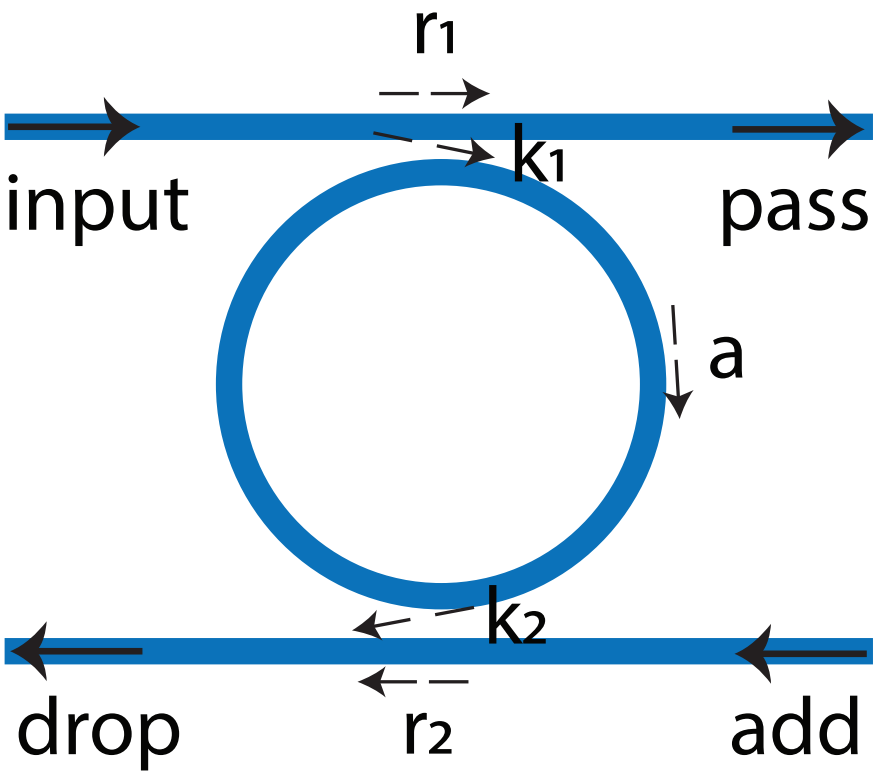

Figure 1.5. A schematic simple ring resonator with the two waveguides and the ring

At this point, the quality factor, which describes the sharpness of the resonator with respect to its resonant frequency, can be written as.

$$Q = \frac{\omega_{res}}{\Delta\omega} = \frac{\lambda_{res}}{\Delta\lambda} \tag{1.19}$$

where $\Delta\lambda$, $\Delta\omega$ are the full-width at half-maximum (FWHM) of the resonator. It is worth noting that there are two quality factors: loaded Q and intrinsic Q. The intrinsic Q describes the quality factor when the resonator is assumed not to be coupled to the bus waveguide.

As written in the section 1.3, Q can be written as ω_{res}/κ as well. The photon-decay rate of the cavity, κ, can be attributed to 2 parameters, as in $\kappa = \kappa_e + \kappa_0$, where κ_e denotes coupling loss rate, and κ_0 denotes intrinsic loss rate. Therefore, the loaded quality factor, Q_L is written as

$$Q_L = \frac{\omega_{res}}{\kappa_e + \kappa_0} \tag{1.20}$$

whereas the intrinsic quality factor, Q_I, is written as

$$Q_I = \frac{\omega_{res}}{\kappa_0} \tag{1.21}$$

Since the coupling introduces losses to the resonator, the intrinsic Q is always greater than the loaded Q. The intrinsic quality factor, Q_I, can alternatively be written using the loaded quality factor as

$$Q_I = \frac{2Q_L}{1 \pm \sqrt{T_{min}}} \tag{1.22}$$

where T_{min} refers to the normalized transmission on resonance [39]. When the resonator is under-coupled, the equation.1.22 has the plus sign and when the resonator is over-coupled, the equation.1.22 has the minus sign. Unless specifically specified, the quality factors referred throughout the Dissertation are loaded quality factors.

There are several loss contributions to the intrinsic quality factor, The intrinsic loss rate κ_0 can be separated into each loss channel as

$$\kappa_0 = \kappa_{ss} + \kappa_{sa} + \kappa_b \tag{1.23}$$

where κ_{ss}, κ_{sa}, κ_b denote surface scattering loss rate, surface absorption loss rate, and doping and impurities loss rate in a bulk crystal, respectively [39]. The surface scattering loss, κ_{ss}, as the name indicates, is related to the roughness of the surface. The surface absorption loss rate, κ_{ss}, however, mostly results from lattice reconstructions and therefore dominantly occurs at the edge of the etched sidewalls of the waveguide, where etching processes damage

the lattice structure. The doping and impurities loss rate in a bulk crystal, κ_b, can be tuned by the number of dopants and/or impurities in the bulk.

From the equation of transmission for a ring resonator with one gap (Eqn. 1.14), the full width at half maximum (FWHM) of the resonance spectrum can be derived as below [37]:

$$FWHM = \frac{(1 - ra)\lambda_{res}^2}{\pi n_g L \sqrt{ra}} \tag{1.24}$$

Similarly, using the equations of transmission for a ring resonator with two gaps (Eqns. 1.17, 1.18), FWHM can be derived for the case:

$$FWHM = \frac{(1 - r_1 r_2 a)\lambda_{res}^2}{\pi n_g L \sqrt{r_1 r_2 a}} \tag{1.25}$$

, where L represents the round trip length, here 2πR, R being the radius of rings.

The wavelength difference between neighboring two resonances or free spectral range (FSR) as a function of wavelength can be derived as below within the first-order approximation of the dispersion [37]:

$$FSR = \frac{\lambda^2}{n_g L} \tag{1.26}$$

Here, I would like to note that both FWHM (Eqns. 1.24, 1.25) and FSR (Eqn. 1.26) are related to the group index, n_g. The group index which takes into consideration the dispersion of the waveguide is defined as below:

$$n_g = n_{eff} - \lambda \frac{dn_{eff}}{d\lambda} \tag{1.27}$$

1.5 Incorporation of ion ensembles into solids

There are mainly two ways to incorporate ions in solid hosts: doping and implantation. In the doping technique, Ions are co-deposited when solid host materials are deposited. Historically, the doping technique was used to make waveguides in bulk crystals [40]. Typically, doped ions are less inhomogeneously broadened compared with implanted ions. When com-

pared, the inhomogeneous broadening of doped Yb^{3+} ions is about a factor of 2 magnitudes smaller than that of implanted Yb^{3+} ions [41], [42]. Therefore, doped ions show less decoherence compared with implanted ions. So, the doping technique can be more beneficial than the implantation technique when the applications are critically dependent on coherence properties. On the other hand, in the implantation technique, ions are bombarded into solids with high energy. In order to model the range of depths of implanted ions, The Gaussian distributions are used, and therefore the impurity concentration as a function of depth in amorphous solid can be written as the equation 1.28 [43].

$$N(x) = \frac{\phi}{\sqrt{2\pi}\sigma_p} e^{-(x-R_p)^2/2\sigma_p^2} \tag{1.28}$$

where R_p is the projected range, σ_p is the standard deviation of the projected range, and ϕ is the total implanted dose. Also, the projected range (R_p), the standard deviation (σ_p), and the impurity concentration N(x) all can easily be calculated by Stopping and Range of Ions in Matter (SRIM) simulation.

Because of the high energy by the ions, the implantation technique causes crystal damage to the structure (Fig. 1.6.(a)). However, the crystal damage caused by implantation can mostly be recovered by an appropriate annealing procedure (Fig. 1.6.(b)).

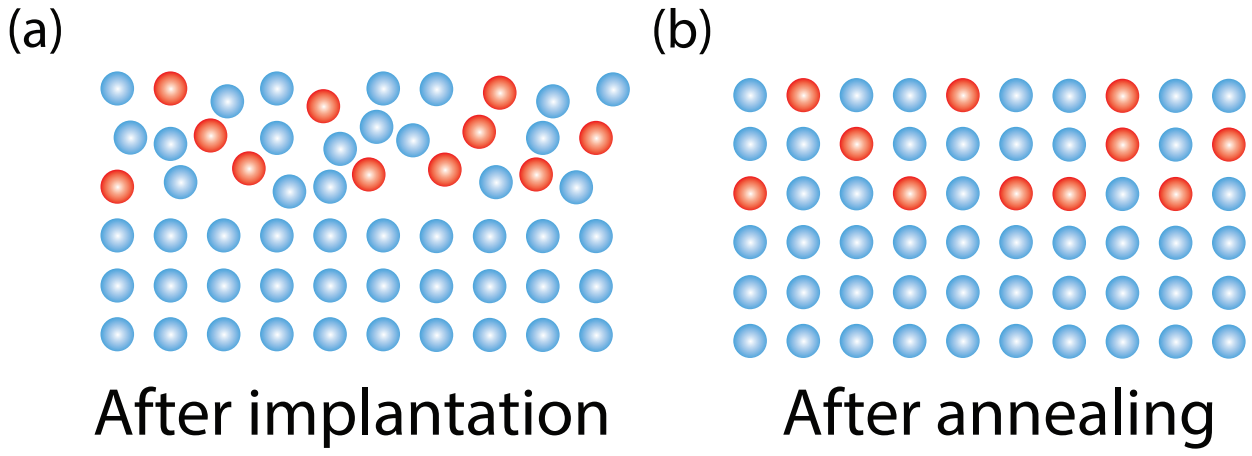

Figure 1.6. (a) Crystal damage caused by high energy ion implantation; (b) Recovered crystal structure by an appropriate annealing procedure. Red balls denote ions implanted, blue balls denote host atoms

One advantage of the implantation technique is the location of ions is controllable, by calibrating the implantation energy. For example, one research used the implantation technique to precisely locate a defect center in a 1D photonic cavity for strong light-atom interaction [44]. With this advantage of the implantation technique, In our group, we precisely implanted an array of Er^{3+} ions into the resonator modes of the silicon nitride ring resonators and studied the effect of ion geometries [45].

1.6 Outline of the Dissertation

This Dissertation mainly focuses on 1) the fabrication of SiN/LN ring resonators and 2) the optical characterizations of implanted ions in SiN/LN structures. Chapter 2 studies the fabrication method for SiN ring resonators and the emission and absorption by implanted REIs in the micro SiN structure. Chapter 3 studies the fabrication process of LN ring resonators and the emission and absorption by implanted REIs in the micro LN structure. Chapter 4 studies the collective and cooperative effects of periodic rare-earth ion arrays in the LN micro-ring resonators, and finally, Chapter 5 summarizes the dissertation and proposes future works.

2. RARE-EARTH IONS IMPLANTED PHOTONIC RESONATORS BASED ON THIN-FILM SILICON NITRIDE

2.1 Introduction

Rare-earth ions (REIs) in solids are attractive optical centers. This is because partially filled 4f orbitals of REIs are electronically shielded by outer 5s, 5p, 6s orbitals [46]. As a result, REIs are relatively insensitive to the local environment. Due to this property, REIs in crystals have shown record-long coherence time [18] and high quantum storage efficiency [20]. Therefore REIs in solids are used for many quantum applications including quantum information processing and quantum communications [47]–[49].

Many pieces of research incorporating REIs into different solid host materials have been conducted. For example, YSO [18], [33] and LN [42], [50] and YVO [34] have been used as host materials for REIs. Among these solids, SiN is a material of our interest because SiN is a CMOS-compatible material. By using SiN, we can use well-developed technology from the microelectronics industry and significantly reduce the cost of fabrication in large scales [51], which is essential for building practical quantum networks. Moreover, low propagation loss grown by LPCVD SiN waveguide [4] and micro-resonators with high quality factor have been reported [5], [6]. Lastly, parametric amplification [52] and broadband super-continuum generation [53] in SiN waveguide have been reported due to its nonlinear properties, which shows the possibility of SiN in the applications of integrated photonics.

In the quantum domain, entangled-photons generation with four-wave mixing on SiN micro-resonators has been reported [54]. Also, one study showed that entangled photons could be stored in Er-doped amorphous silica fiber [13]. Motivated by this recent progress, we decided to investigate amorphous SiN for host materials for REIs. A few REIs have been studied in thin-film SiN. In our lab, we showed controlling Er light emission by atomic geometries [45] and other researchers reported a nine-fold enhanced lifetime of Yb^{3+} ions on SiN ring resonators at sub-Kelvin temperature [30].

Here, we incorporate Yb^{3+} ions in SiN. Yb^{3+} ions are interesting because Yb^{3+} ions coherently interact with both microwave and optical photons and therefore can be used for

microwave-to-optical transduction [24], [25], which is important for future superconducting quantum computers [26].

In this chapter, the fabrication process of SiN micro-structures is introduced and we characterize the optical properties of Yb^{3+} ions in the thin-film SiN. 200nm SiN is fully etched and cm-long waveguides and micro-resonators are fabricated. Yb^{3+} ions are implanted into the micro-structures, and the PL decay and absorption properties of the Yb^{3+} ions are studied.

2.2 Device fabrication

We fabricate centimeter-long waveguides and micro-ring resonators on a SiN wafer. A 200nm thick silicon nitride film on 3µm silicon dioxide (SiO_2) on a silicon substrate is chosen for our fabrication process. The 200nm thick SiN film is deposited in the LPCVD furnace tube with a mixture of dichlorosilane (DCS) and ammonia (NH_3) at 800°C, following the reaction equation written in 2.1. Here DCS and NH_3 work as silicon precursors, nitrogen precursors, respectively [55].

$$3\,SiH_2Cl_2 + 4\,NH_3 \longrightarrow Si_3N4 + 6\,HCl + 6\,H_2 \tag{2.1}$$

To begin with, the hydrogen silsesquioxane (HSQ) film, a negative-tone electron-beam resist, is spun on the SiN wafer and the device pattern is defined by a 100kV electron beam lithography system (JEOL JBX-8100FS) with the beam current of 2nA and dose of 2000µC/cm^2, respectively. The ring radius is designed to be 75µm, and the width of the waveguide and the gap between the ring and the bus waveguide are designed to be 600nm and 250nm, respectively.

After e-beam exposure, the sample is developed in 25% Tetramethylammonium Hydroxide (TMAH) solution for 70 seconds at room temperature. In order to transfer the pattern to the SiN film, the SiN film is etched with the mixture of CHF_3 and O_2 gases using the exposed HSQ as an etch mask in an ICP-RIE tool (Panasonic P610), using the parameters on Table 2.1. The etching rate of SiN is approximately 100nm/min. The etched SiN waveguides show vertical (90°) sidewall angle, as shown in Fig. 2.1.(i).

Table 2.1. SiN etching parameters on the Panasonic P610 ICP-RIE tool

Etch parameters	Value
CHF_3 Flow rate	35 sccm
O_2 Flow rate	15 sccm
Chamber pressure	7.5 mTorr
Chamber temperature	50 $^{\circ}$C
Etch rate	100 nm/min
ICP power	550 W
RIE power	50 W

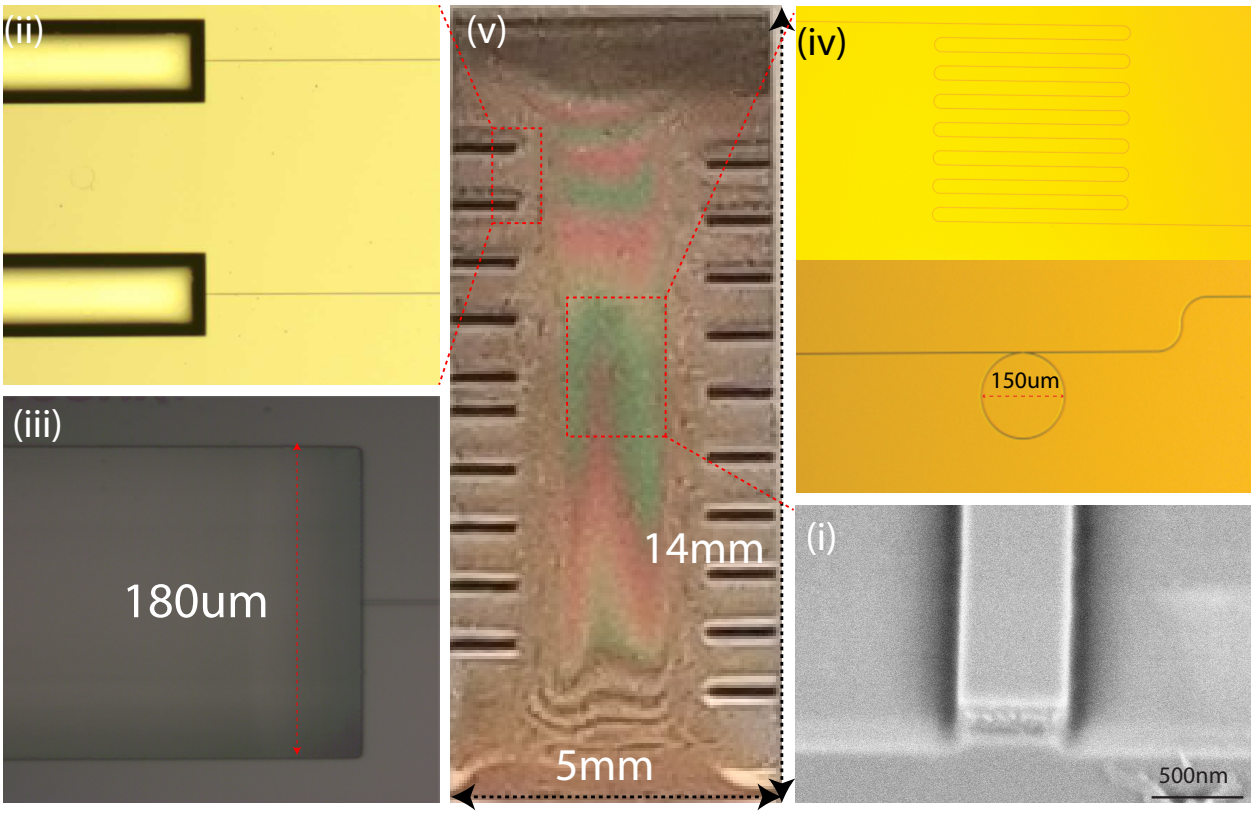

Figure 2.1. (i) SEM image showing a cross-sectional view of the SiN waveguide. The etched angle of SiN waveguide is almost vertical (∼90°); (ii),(iii) Optical microscope images of U-grooves where the lensed fibers are located for direct light coupling to the waveguides; (iv) Optical microscope image of SiN centimeter-long waveguides (top) and micro-ring resonators (bottom). The radius of the ring and the maximum gap between the bus waveguide and the ring is 75µm and 250nm, respectively; (v) A diced SiN waveguide chip after all the fabrication process.

For efficient and stable light coupling to the waveguide, U-grooves are patterned with photo-lithography using omnicoat and SU-8 photoresist. Omnicoat is used to promote adhesion of SU-8 photoresist and it also allows easy stripping of the SU8 layer on top, so it also works as a lift-off layer. Then, U-grooves are dry-etched in the silicon substrate, as seen in Fig. 2.1.(ii),(iii), using a deep RIE tool (STS-ASE). U-grooves minimize the mechanical vibration and misorientation problem to the waveguide during measurement [56]. The etched depth of the U-grooves is about 70µm, about the half diameter of an optical fiber. Therefore, we can easily align an optical fiber core to the waveguide by just locating the fiber down to the bottom of the U-grooves, which makes the fiber core semi-self-aligned to the waveguide.

Then, the fine-tuning of the fiber position using 3-axis nano-positioning stages enables relatively easy light coupling to the waveguides at cryogenic temperatures. In this way, we can fabricate long-waveguide and micro-ring resonators are shown in Fig. 2.1.(iv). Then, the SiN wafer is diced into several chips such as Fig. 2.1.(v) for easy handling and measurement.

Finally, the chip is dipped into buffered oxide etch (BOE) solution for 10 seconds to remove the left-over HSQ film on top of the LN patterns. This relatively short etching process removes only the exposed HSQ film on the top while minimizing the damage to the bottom buried oxide film.

2.3 Optical characterizations

The fundamental TE mode is well confined in the fully etched SiN waveguide for 0.9µm as shown in Fig. 2.2, but the TM modes are not confined because of the thickness of the waveguide.

2.3.1 Yb^{3+} ion implantation

The sample is cleaned with the standard solvent/piranha cleaning method to remove contaminants on the surface before ion implantation. Yb^{3+} ions are implanted into the SiN waveguide with the energy of 100keV and fluence of 1×10^{14} ions/cm^2 (Fig. 2.3. (a)). This ion fluence corresponds to a peak concentration of 0.04%. To repair crystal damage caused

by ion implantation, post-implantation annealing is conducted at 1100°C for 1 hour under a nitrogen atmosphere.

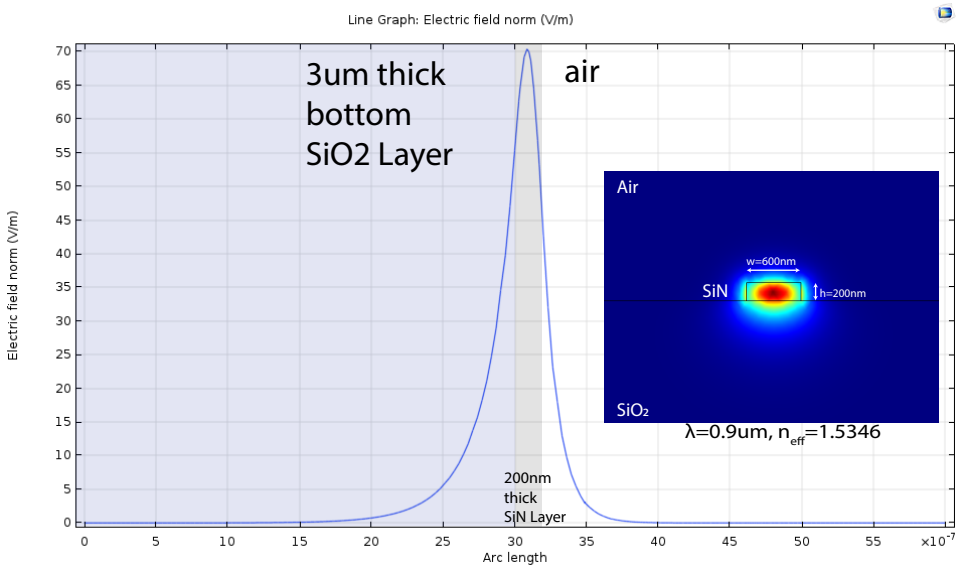

Figure 2.2. The TE electric field amplitude distribution in the SiN waveguide and the corresponding Comsol simulation of the fundamental TE mode in the cross-section of the structure at 0.9µm. The width and height of the waveguide are 600nm, 200nm, respectively.

The SRIM simulation indicates that the peak of the ion distribution is around 30nm below the top surface of the SiN film with a Gaussian distribution width of around 6.5nm (Fig. 2.3. (b)). At the position of the ions, the coupling strength of the TE electric field to the ions ($(|E(r_{yb})/E(peak)|)$) is 0.757, which can be calculated from Fig. 2.2.

2.3.2 Emission of Yb^{3+} ions

In order to observe lifetime modification by the cavity, the lifetimes of Yb^{3+} ions in the long waveguide (top image of Fig. 2.1.(v)) and in the ring resonator (bottom image of Fig. 2.1.(v) were individually measured. The chip is cooled to 4K using a table top cryostat (Montana Instrument).

We use light at 916nm as the pump which is pulsed for 3ms using an acousto-optic modulator (AOM). The AOM is used to control the pump intensity to excite the Yb^{3+} ions. The pump and PL light are coupled to/from the waveguide by means of a lensed fiber whose

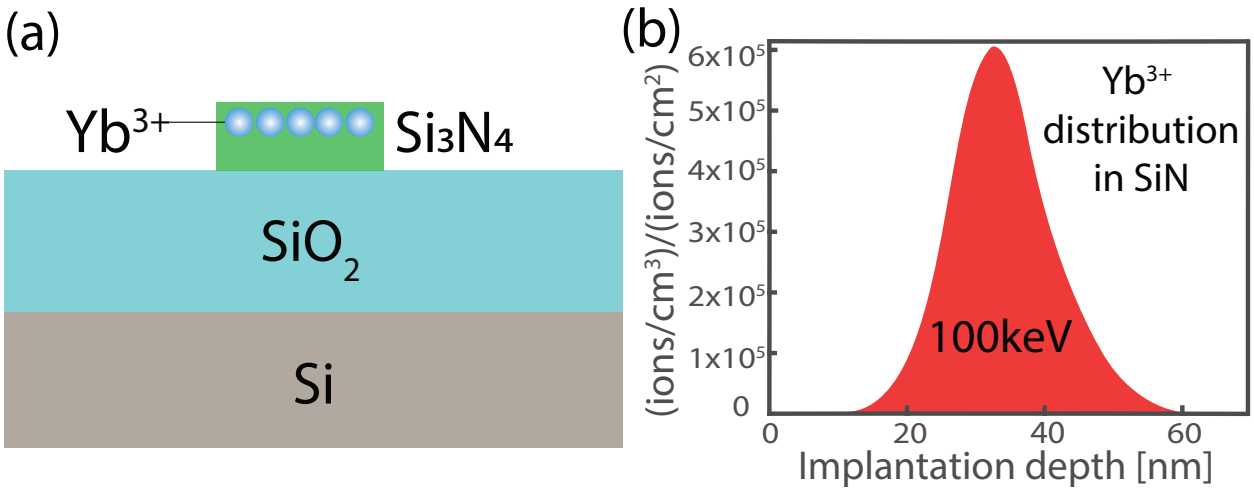

Figure 2.3. (a) The schematic cross-section diagram of Yb^3 ions implanted in SiN structure. The thickness of each layer in the diagram does not represent the actual proportion of the wafer; (b) SRIM simulation of implanted Yb^{3+} distribution in SiN is shown for energy and fluence of 100keV and 1×10^{14} ions/cm^2 respectively.

alignment is assisted by the U-groove and nano-positioning stages. The emitted signal is, then, connected to the single-photon detector (SPD) to detect the PL counts of the emitted photons from the Yb^{3+} ions in the cm-long waveguide and ring resonator.

The schematic experimental set-up for the lifetime measurement is illustrated in Fig. 2.4.(a). We observed that the lifetime of Yb^{3+} ions in the ring resonator case is a little bit reduced by the cavity effect compared with the lifetime in the long waveguide, as shown in Fig. 2.4.(b). But because of the low-quality factor of the resonator (Max Q observed ~7.0E+04), the reduction rate is pretty low. Since the lifetime modification by cavities is proportional to Q, more lifetime shortening is expected with higher Q resonators.

2.3.3 Absorption effect by Yb^{3+} ions

We try to measure the absorption effect modified by the ions by observing the cavity linewidth and the relative contrast of bus-to-ring coupling (1-T_{min}). The cavity linewidth around 918nm, where one of the Yb^{3+} absorption peaks is expected, is broader than the linewidth away from the transition as seen in Fig. 2.5.(a). We believe that the atom-induced absorption loss attributes to the broadening.

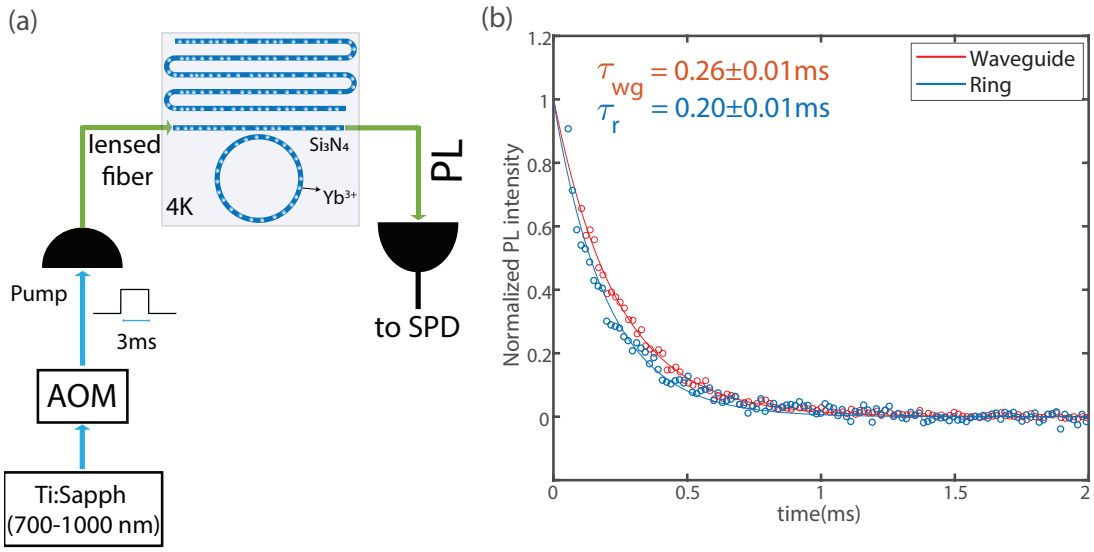

Figure 2.4. (a) The schematic diagram of experimental set-up for Yb^{3+} lifetimes; (b) The normalized PL decay curves of Yb^{3+} ions measured at 4K from the long waveguide (red), and the ring resonator (blue) are presented, showing the lifetime is shortened by resonator

In Fig. 2.5.(b), the blue dots show the intrinsic quality factor of the resonator as a function of the wavelength. The resonator linewidths for the fundamental TE mode at almost every free spectral range (FSR) are measured and their intrinsic Q factors are plotted.

From the Q value data in Fig. 2.5.(b), we believe that the atomic absorption takes place around 918nm. The red data indicate the relative contrast (or reduced transmission, $1 - T_{min}$) as a function of wavelength. In the over-coupled regime, as the intra-cavity light frequency approaches the atomic transition, the atom-induced loss is expected to bring the resonator closer to the critical coupling regime. The result in Fig. 2.5 (a) and (b) shows that the intrinsic Q and also minimum transmission drop near the atomic resonance.

Studying impedance-matched (critically-coupled) cavities is important in that atoms in cavities with critical coupling conditions can be used for efficient light storage [57]. For the general cavity, by tuning the reflectivity of the mirrors and optical depth of the crystal inside the cavity, the impedance-matched condition can be achieved [19]. Mirror reflectivity, in the ring resonator case, corresponds to the waveguide-to-ring coupling, determined by the gap between the ring and the bus waveguide, and also the optical depth, in our case, can be

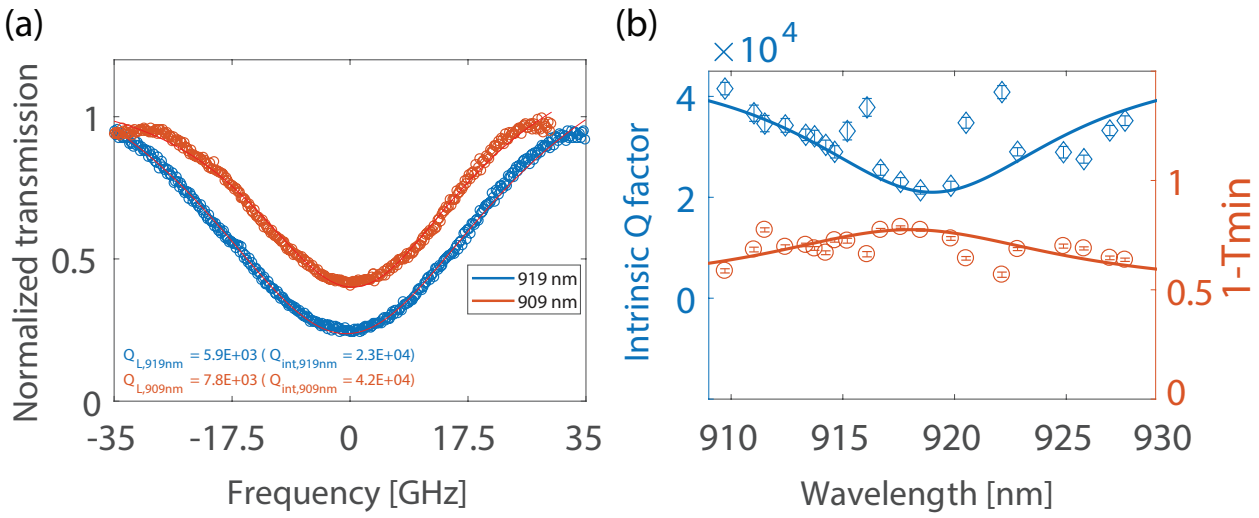

Figure 2.5. (i) Cavity transmission signals centered around 909nm and 919nm. The data show that the intrinsic quality factor at 919nm is about 2 times smaller than the intrinsic Q value at 909nm due to the atomic induced absorption loss; (ii) The blue dots show the intrinsic quality factor vs wavelength suggesting that the quality factor decreases around the expected Yb^{3+} transition. The red dots show the contrast or the minimum transmission at the cavity resonance (T_{min}) as a function of wavelength indicating the effect of atoms in reaching near-critical coupling condition.

tuned by the concentration of implanted ions. Therefore, here we have studied the near critical-coupling condition modified by atoms.

The minimum transmission can be calculated using the equation 2.2.

$$T_{min} = (\frac{\kappa_e - \kappa_0}{\kappa_e + \kappa_0})^2 \tag{2.2}$$

where κ_e and κ_0 are coupling and intrinsic loss rates. By assuming a Gaussian profile for the atomic absorption accounting for the inhomogeneous broadening of atomic transitions, we can model the frequency-dependent intra-cavity loss as $\kappa_0 = \kappa_c + \alpha(\lambda)$ where κ_c is the bare intra-cavity loss rate and $\alpha(\lambda)$ is the absorption rate defined by the optical density of atoms. The intrinsic Q factor can also be written as $Q_{int} = \omega_0/\kappa_0 = 2Q_L/(1 - \sqrt{T_{min}})$, where ω_0 and Q_L are the optical frequency and loaded Q, respectively. By fitting the data in Fig. 2.5 (b) and appropriately weighting the errors, we infer $\kappa_e/(\kappa_c + \alpha_{max}) \simeq 2.7$. Using

this calibration, the exact critical coupling condition, $\kappa_e = \kappa_c + \alpha(\lambda)$, can be engineered by careful design of the waveguide-ring gap and/or density of atoms.

2.4 Conclusion

In this chapter, a fabrication method to vertically etch SiN waveguide, ring resonator is introduced. For more secure light coupling to the waveguide, U-grooves are etched as well. The Yb^{3+} ions are, then, implanted to the SiN structures. We compared the lifetime in the waveguide with the lifetime in the resonator at 4K to observe lifetime modification by the cavity. The lifetime of Yb^{3+} ions in the resonator is slightly reduced by the cavity, but the reduction rate is limited by the low-quality factor of the resonator (maximum Q observed ~7.0E+04).

Moreover, the atomic absorption effects reduced intrinsic Q-factors, and increased relative contrast near the atomic transition were observed. With careful design of the waveguide-to-ring gap and concentration of ions, impedance-matched cavity, which can be used for efficient light storage, can be realized.

3. RARE-EARTH IONS IMPLANTED PHOTONIC RESONATORS BASED ON THIN-FILM LITHIUM NIOBATE

Credit line - This chapter is reproduced from: D. Pak *et al.*, J. Appl. Phys. **128**, 084302 (2020), with the permission of AIP Publishing.

3.1 Introduction

Rare-earth ions (REIs) in solids have many applications in nonlinear optics including lasers and optical amplifiers due to their stable optical transitions and long lifetimes [1], [2]. REIs also feature long nuclear spin coherence times [18] and weak coupling to external radiation [58], which are attractive features for applications in quantum information processing. The crystalline solids incorporated with quantum centers such as REIs enable miniaturization of quantum optical elements which will play a key role in the implementation of future multiplexed quantum optical networks. To date, the integration of nanophotonic resonators on bulk rare-earth crystals resulted in the demonstration of quantum storage [33], single-photon generation [59], strong atom-photon interactions [26], [60] and quantum transduction [25].

With growing interest in REIs, their incorporation into a variety of host materials such as silicon nitride [30], [45], yttrium orthosilicate (Y_2SiO_5) crystal [33], and bulk lithium niobate (LN) crystals [41], [50] has been considered. Among those host materials, LN crystal is an attractive option with various optical applications including quantum photonics [61], owing to its unique piezoelectric, electro-optic, nonlinear and acousto-optic properties [7]. Since LN used to be a hard-to-fabricate material, the applications of LN photonics were limited to bulk crystals until recently. Historically, for making waveguides in LN bulk crystals, methods such as Titanium in-diffusion [40], [62] and UV-laser irradiation [63] have been commonly used. Therefore, indirect approaches, such as making Si waveguides on LN layer (Fig. 3.1.(a)) and direct bonding of bulk LN crystal and SiN resonators (Fig. 3.1.(c)), are considered to make use of the advantages of LN as host materials [64].

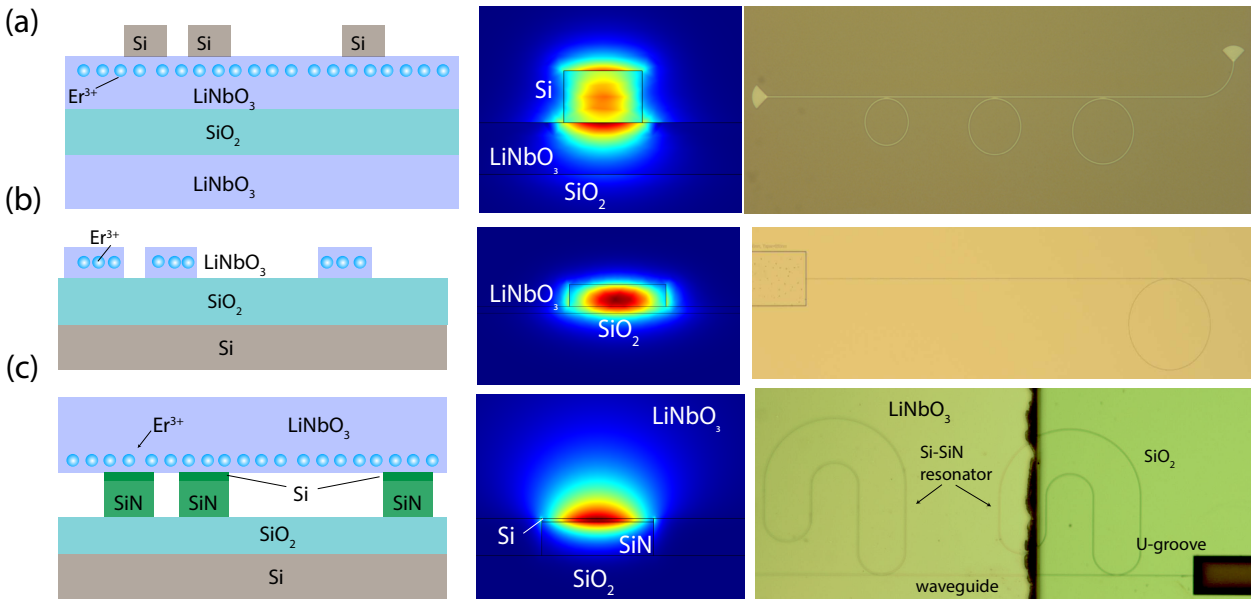

Figure 3.1. (a) A silicon resonator array is fabricated on a lithium niobate hosting Er ions evanescently interacting with the light in a silicon waveguide. (b) Direct fabrication of lithium niobate resonators with U-groove fiber couplers using reactive ion etching. (c) Direct bonding of lithium niobate with SiN resonators. Schematic cross-section, Comsol simulation, and optical microscope image of the device are shown from left to right, respectively.

However, a recently developed lithium niobate on insulator (LNOI) platform and its nano-fabrication technique, which enables direct LN etching (Fig. 3.1.(b)) , made low optical propagation loss and strong optical confinement possible [8], [9]. For example, integrated LN waveguides and resonators have been used lately for second harmonic generation [65], and quantum frequency conversion [66], [67].

Motivated by recent progress in LN nano-fabrication, we consider adopting thin-film LN as a host material for REIs. There have been a few efforts to investigate the properties of Er^{3+} and Tm^{3+} ions in thin-film LN [68], [69]. Here, we consider the incorporation of ytterbium ions (Yb^{3+}) in thin-film LN crystals. Yb^{3+} ions have interesting optical and spin properties and their integration with photonic devices is particularly important for memory and transduction applications. It was recently shown that Yb^{3+} ions in yttrium orthosilicate (YSO) crystals can exhibit both microwave and optical coherence [24], which can be used for a microwave to optical transduction [25]. As the transduction of microwave

photons to optical signals at cryogenic temperatures is important for future superconducting quantum computers and Yb^{3+} ions are promising candidates for such application [26], their integration and study of optical properties are particularly interesting. Moreover, photon-atom interaction in the strong coupling regime has been recently achieved using Yb^{3+} ions in bulk YSO crystals [60]. Therefore, investigating the properties of Yb^{3+} ions in thin-film LN crystals, where multi-functional devices can be implemented on a photonic platform, has the potential to advance quantum information processing, while bringing the advantages of both REIs and thin-film LN crystalline hosts.

In this chapter, we investigate the fabrication of LN micro-structures on a thin-film LN on insulator platform and characterize the optical properties of Yb^{3+} ions implanted into the LN film. We fully etch the LN film using an optimized etching recipe and fabricate cm-long waveguides and micro-resonators. We implant the micro-structures with Yb^{3+} ions and study the photoluminescence and absorption properties of the ions in the thin-film crystalline host.

3.2 Device fabrication

We fabricate centimeter-long waveguides and micro-ring resonators on a commercially available (NanoLN) LNOI wafer, made by the smart-cut process. A 600nm thick z-cut lithium niobate film on 2µm silicon dioxide (SiO_2) on silicon substrate is chosen for our fabrication process. The ring radius is designed to be 150µm, and the width of the waveguide and the gap between the ring and the bus waveguide are designed to be 800nm and 300nm, respectively.

The device fabrication steps are almost the same as the previous chapter 2.2 except for etching. To begin with, 1µm thick hydrogen silsesquioxane (HSQ) film, a negative-tone electron-beam resist, is spun on the LNOI wafer using the parameters on Table 3.2 and the device pattern is defined by a 100kV electron beam lithography system (JEOL JBX-8100FS) with the same parameter. Because the etching selectivity between the exposed HSQ and LN is pretty low (∼1.6:1), 1µm of HSQ film is required to fully etch 600nm LN film.

Table 3.1. 1um thick spin-coating recipe to apply HSQ - FOx-16 electron beam resist

material	ramp rate (rpm/s)	spin speed (rpm)	hold time (sec)	bake temp (°C)	bake time (min)
FOx-16	1	1000	30	120	3

Here, in the whole fabrication process, the LN etching part is the key process. We observed that etched LN particles can be easily re-deposited on the surface, as shown in Fig. 3.2. In order to obtain clean and smooth waveguides, an optimized setting of etching parameters is required. We use an ICP-RIE tool with $Ar/Cl_2/BCl_3$ plasma and HSQ as a etch mask but other researches using only Ar plasma [28], [69], [70] or different etch masks are also reported [69], [71]. The research which used ion milling to etch thin film LN is also reported [72]. The Table 3.2 shows the parameters of each etching process and their etching angle.

Table 3.2. Comparison of different LN etching processes

	This work	**Ref.[71]**	**Ref.[28], [70]**	**Ref.[69]**	**Ref.[72]**
LN cut plane	Z-cut	Z-cut	X-cut	X-cut	Z-cut
Etching method	ICP-RIE	ICP-RIE	ICP-RIE	RIE	Ion milling
Etch mask	HSQ	SiO_2	HSQ	Si	ZEP
Etching gases	$Ar/Cl_2/BCl_3$	$Ar/Cl_2/BCl_3$	Ar	Ar	Ar
ICP power(W)	1000	800	N/A	N/A	N/A
RIE power(W)	500	100	112	N/A	N/A
Sidewall angle	55°	83°	62°	45°	75°

While fully etching the 600nm LN film and at the same time to get a smooth surface, the LN film is etched with an optimized $Ar/Cl_2/BCl_3$-based chemistry [71] using the exposed HSQ as an etch mask in an inductively coupled plasma – reactive ion etching (ICP-RIE) tool (Panasonic P610). We totally etch away the 600nm LN film using 6 sccm of Cl_2, 15 sccm of BCl_3, and 30 sccm of Ar with ICP and RIE powers of 1000W and 500W, respectively. The etching rate of LN is approximately 50nm/min. After LN etching, we observed the clean surface without any re-deposited LN particles, as shown in Fig. 3.3.(a). Fig. 3.3.(b) shows the cross-section scanning electron micrography (SEM) image of the etched LN film. Unlike

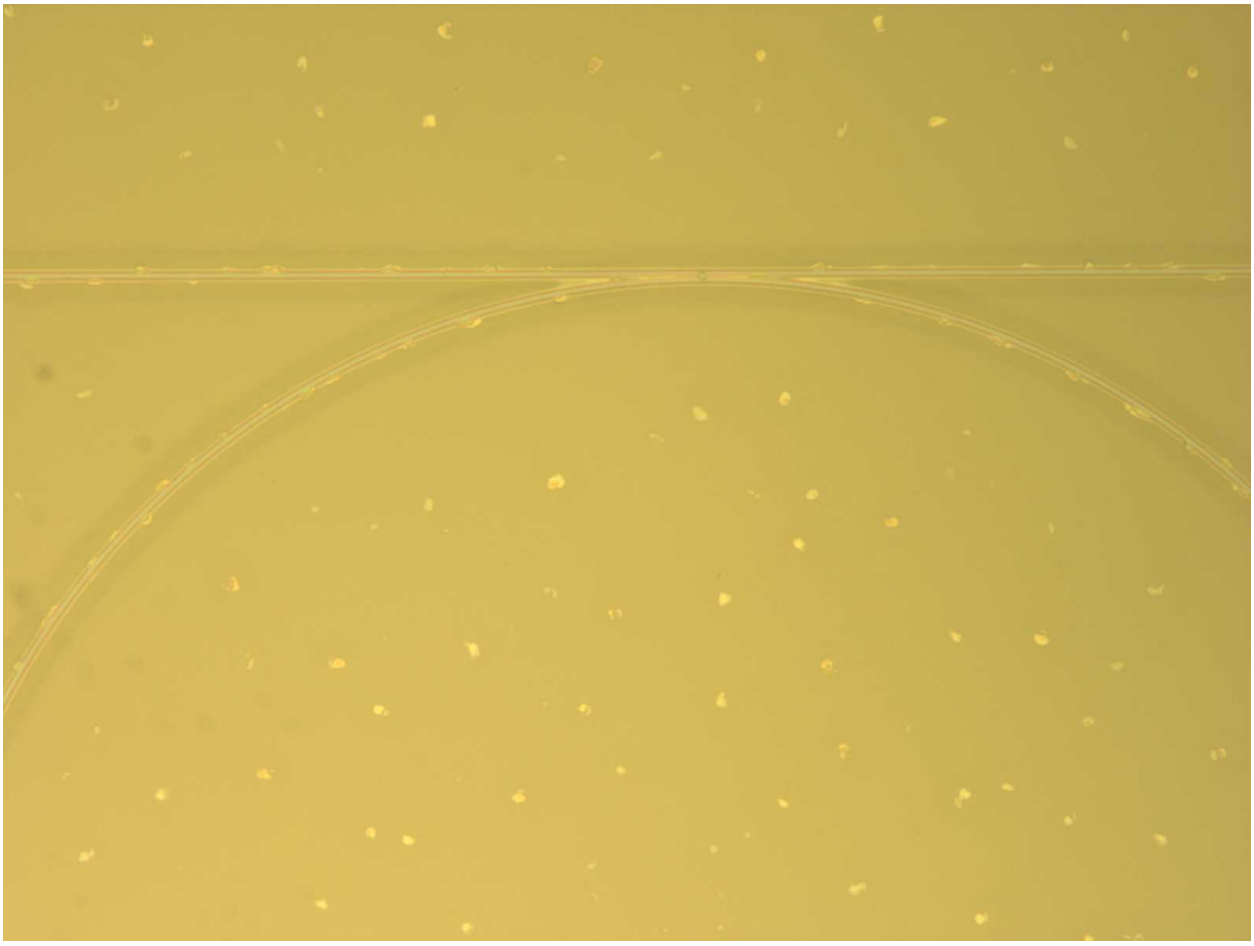

Figure 3.2. An optical microscope image showing a top view of the etched LN waveguide. Etched LN particles are redeposited on the surface. In order to obtain a smooth and clean surface, an optimized LN etching recipe is required.

the SiN waveguides, which showed the vertical sidewall angle, it can be seen that the angle of the etched LN waveguide is approximately 55°. Direct LN etching typically suffers from non-vertical side-wall angles, as you can see from the Table. 3.2.

Similarly, U-grooves are etched into the Si substrate for easy fiber-to-waveguide coupling. In order to further improve the efficiency of fiber-to-waveguide coupling, the waveguides are tapered to a width of 550nm at both ends. The TE mode area at this taper is about 0.21µm^2 at 0.9µm, which we believe can be optimized further for better fiber-to-waveguide coupling. The chip is dipped into buffered oxide etch (BOE) solution for 10 seconds to remove the left-over HSQ film on top of the LN patterns. After all the fabrication steps, we spincoat 1µm

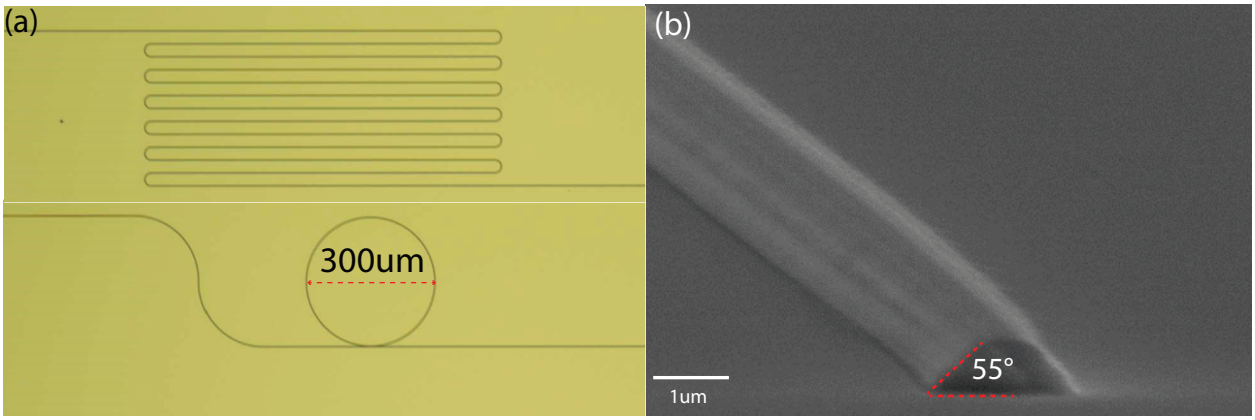

Figure 3.3. (a) Optical microscope image of LN centimeter-long waveguides (top) and micro-ring resonators (bottom). The radius of the ring and the maximum gap between the bus waveguide and the ring is 150µm and 300nm, respectively; (b) SEM image showing a cross-sectional view of the LN waveguide. The etched angle of the LN waveguide is about 55°. Reproduced from D. Pak *et al.*, J. Appl. Phys. **128**, 084302 (2020), with the permission of AIP Publishing.

thick PMMA on the chip as an upper cladding for better mode confinement and protection of the patterns.

3.3 Optical characterization of the fabricated waveguides

The fundamental TE mode is well confined in the fully etched LN waveguide for both 0.9µm and 1.5µm wavelengths (see Fig. 3.4). The design enables investigation of optical properties at both wavelengths which can be important when, for example, co-implantation of Er^{3+} is considered. Moreover, utilizing non-degenerate nonlinear processes in LN may lead to the implementation of multi-functional devices where photons at these two wavelengths are generated, one stored (0.9µm photon) and one transmitted (1.5µm photon) through the fibers. More importantly, the considered cross-section of the waveguide allows reducing scattering loss from the rough sidewalls at around 0.9µm in expense of making the resonator and waveguide multimode. The Figure. 3.5. shows the cavity lines for 0.9 µm and 1.5 µm wavelengths indicating 5 fold increase of the loaded Q factor at 0.9 µm compared to 1.5 µm.

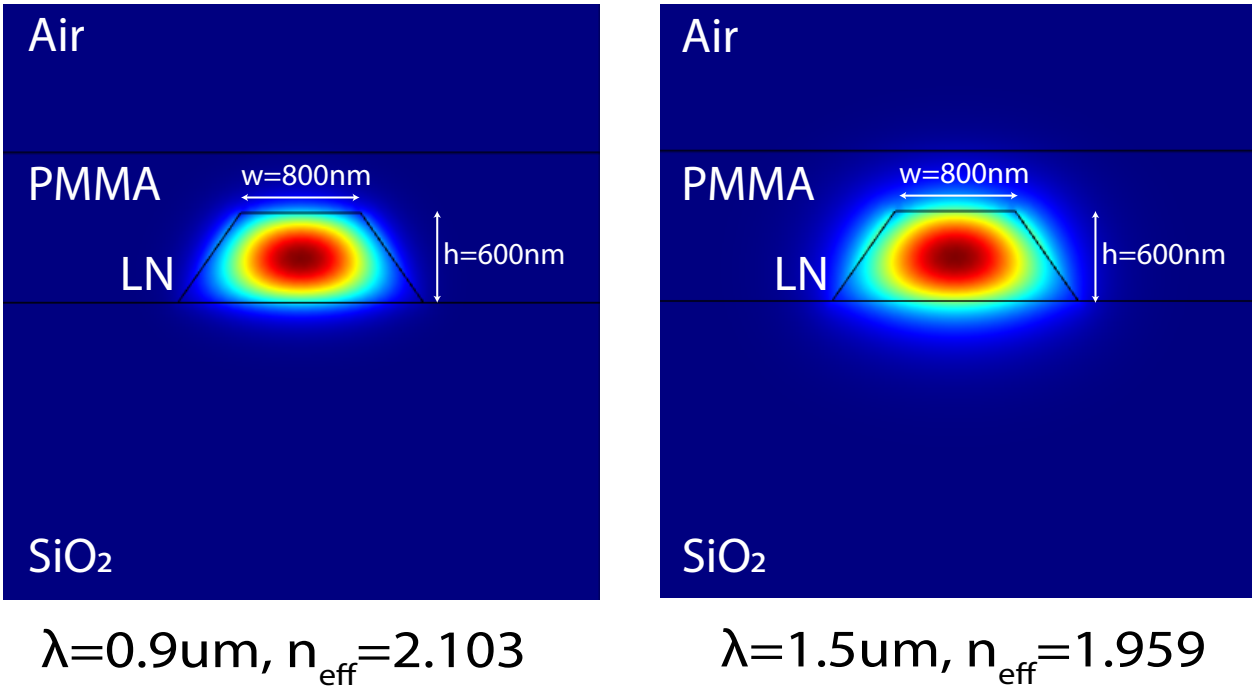

Figure 3.4. Comsol simulation of the fundamental TE mode in the cross-section of the structure at 0.9µm and 1.5µm. The width and height of the patterns are 800nm, 600nm, respectively. Reproduced from D. Pak *et al.*, J. Appl. Phys. **128**, 084302 (2020), with the permission of AIP Publishing.

We note that for applications such as light storage using an ensemble of atoms, which is one motivation of the current work, the optical mode of the signal being stored defines the mode of the collective atomic excitation and multimode waveguides do not necessarily limit the efficiency of the storage. Furthermore, in the current multimode waveguide structure, the difference in the ion interaction strength between the fundamental TE and TM modes is small and the system should be symmetric for both σ and π polarizations particularly around 920nm[41] transition (see Fig. 3.6). This may also enable the storage of polarization qubits given the large bandwidth of ions in the LN host crystals.

3.3.1 Yb^{3+} ion implantation

Before ion implantation, the chip is cleaned with the standard solvent/piranha cleaning method to remove PMMA and contaminants on its surface. Yb^{3+} ions are then implanted into the LN waveguide (Fig. 3.7.(a)) with the energy and fluence of 100keV and 1×10^{12}

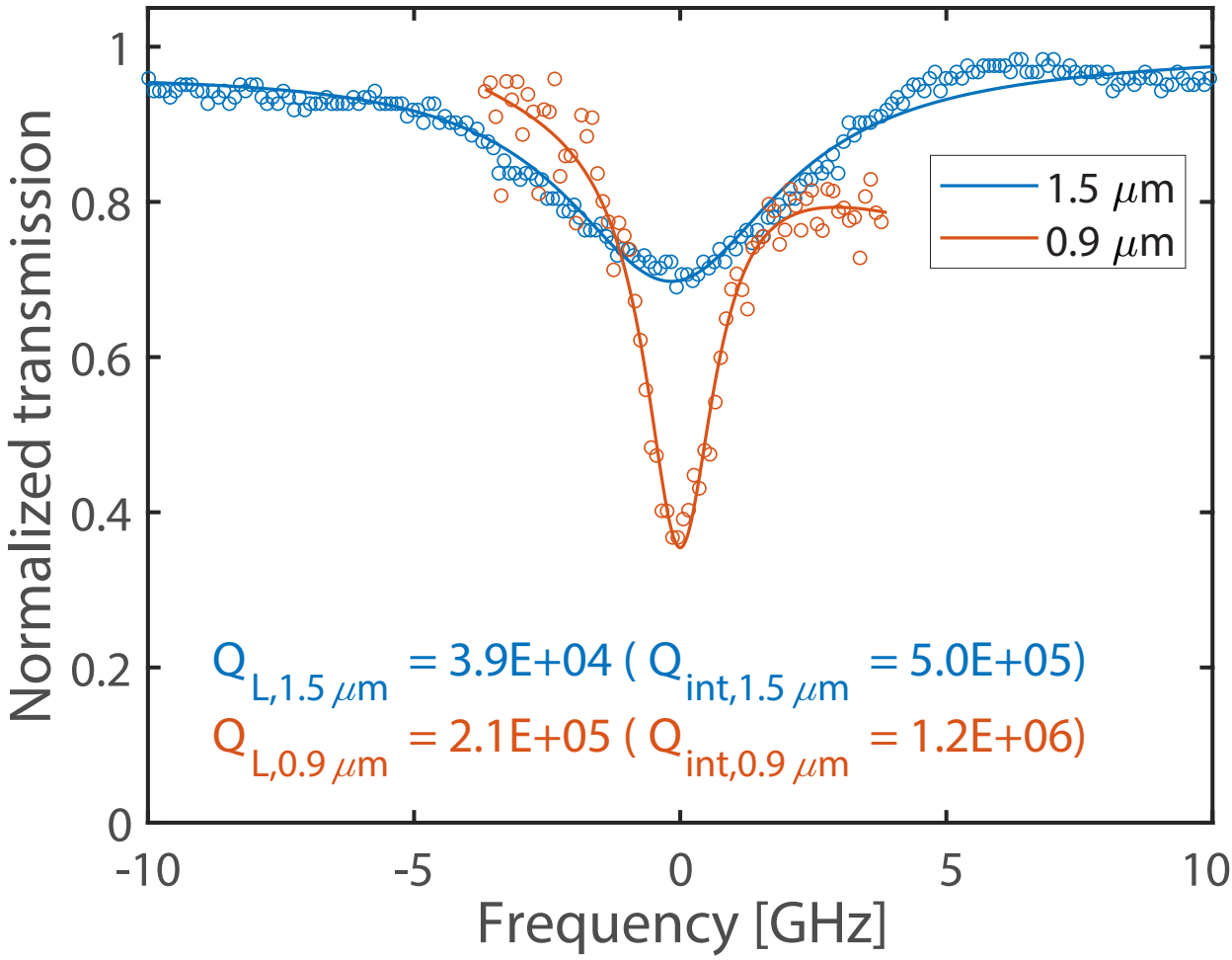

Figure 3.5. The transmission data measured for 1.5µm (blue curve) and 0.9µm (red curve) light, which is over-coupled to the LN ring resonator. Due to the less sidewall scattering at 0.9µm, the loaded Q value at 0.9µm is about 5 times higher than that of 1.5µm. Reproduced from D. Pak *et al.*, J. Appl. Phys. **128**, 084302 (2020), with the permission of AIP Publishing.

ions/cm^2. This ion fluence corresponds to a peak concentration of 0.0002%, which is 2 orders of magnitude smaller than the ion concentrations used in recent works [68], [69].

It is known that the higher the concentration of ions in the crystal is, the higher the spin diffusion and thus the higher decoherence rate is [73]. Therefore, for memory applications, it is important to study light-atom interactions at low concentrations. The low concentration, on the other hand, results in low storage efficiency. Therefore, the implementation of impedance-matched (critically-coupled) cavities hosting atoms is important for efficient

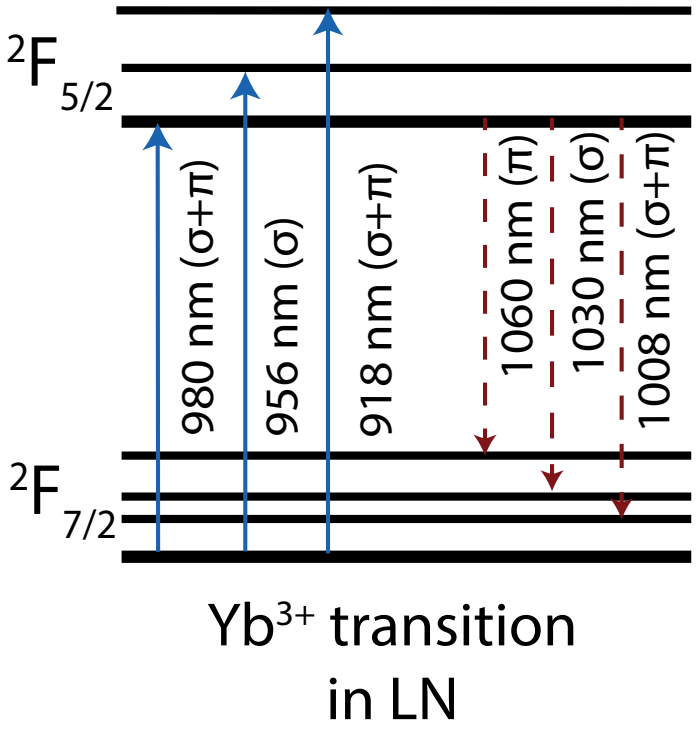

Figure 3.6. The diagram shows the schematic energy levels of Yb^{3+} ions in LN. Reproduced from D. Pak *et al.*, J. Appl. Phys. **128**, 084302 (2020), with the permission of AIP Publishing.

storage [19]. In addition, compared to bulk cavities [57], implemented micro-ring structures enable broadband storage while providing a thermally stable cavity design.

In order to repair crystal structure damage caused by ion implantation, post-implantation annealing is performed at 500°C for 8 hours under a nitrogen atmosphere. To fully recover the damage in the crystalline structure which sometimes is manifested as ion tracks (amorphous regions created by ion trajectory), a higher annealing temperature on the order of 1000°C is required [74]. However, because of the different thermal expansion rates of the wafer's LN/SiO_2 interface, the annealing temperature cannot go higher than 550°C on the LNOI platform, otherwise, the wafer is damaged [75]. We confirm this damage by annealing the LNOI wafer at 600°C as shown in Fig. 3.8.

The SRIM simulation indicates that the peak of the ion distribution is around 30nm below the top surface of the LN film with a Gaussian distribution width of around 10nm as seen in the Fig. 3.7.(b). At the position of the ions, the coupling strength of the TE electric field

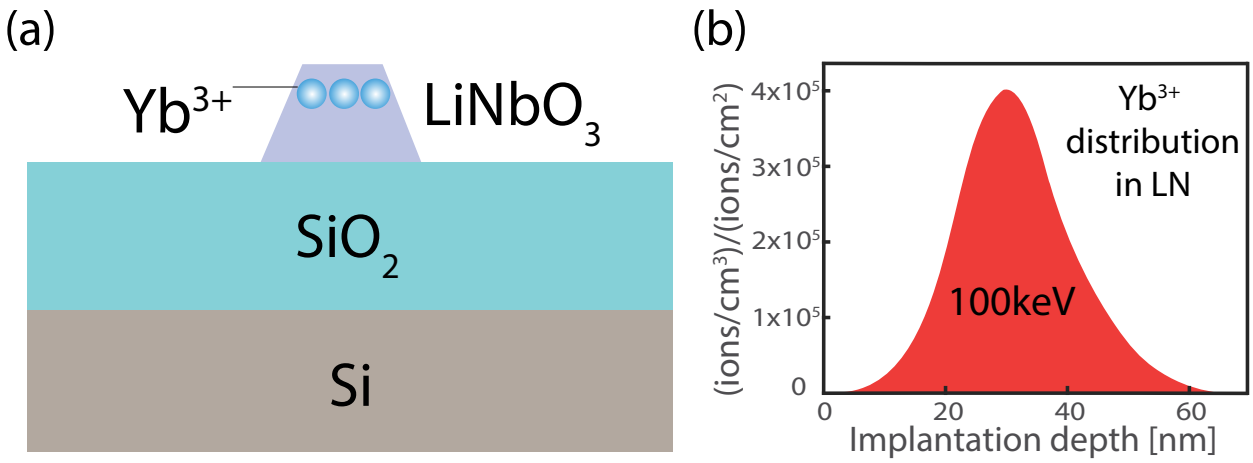

Figure 3.7. (a) The schematic cross-sectional diagram of Yb^{3+} ions implanted in LNOI structure. The thickness of each layer does not represent actual proportion; (b) SRIM simulation of implanted Yb^{3+} distribution in LN is shown for energy and fluence of 100keV and 1×10^{12} ions/cm^2 respectively. Reproduced from D. Pak *et al.*, J. Appl. Phys. **128**, 084302 (2020), with the permission of AIP Publishing.

to the ions ($|E(r_{yb})/E(peak)|$) is 0.463, as shown in Fig. 3.9. Higher implantation energies can be used to increase the coupling strength. However, as the ion energy increases, its trajectory through the crystal becomes more evident creating amorphous regions known as ion tracks. We use lower energies as coherence time and the yield factor are more important quantities for us compared to the coupling strength. Having said that, more investigation is needed to evaluate the surface effects (such as surface strain or surface charges) on coherence time and inhomogeneous broadening. We have observed approximately a factor of two higher inhomogeneous broadening compared to Yb doped bulk crystals [41] which is mostly attributed to the implantation process and the surface effects may have little impact on ion transition broadening at this depth.

Before optical measurements, 1µm thick PMMA is spincoated again as an upper cladding. This is to avoid device degradation overtime, for example due to dust particles, and also to provide better light confinement.

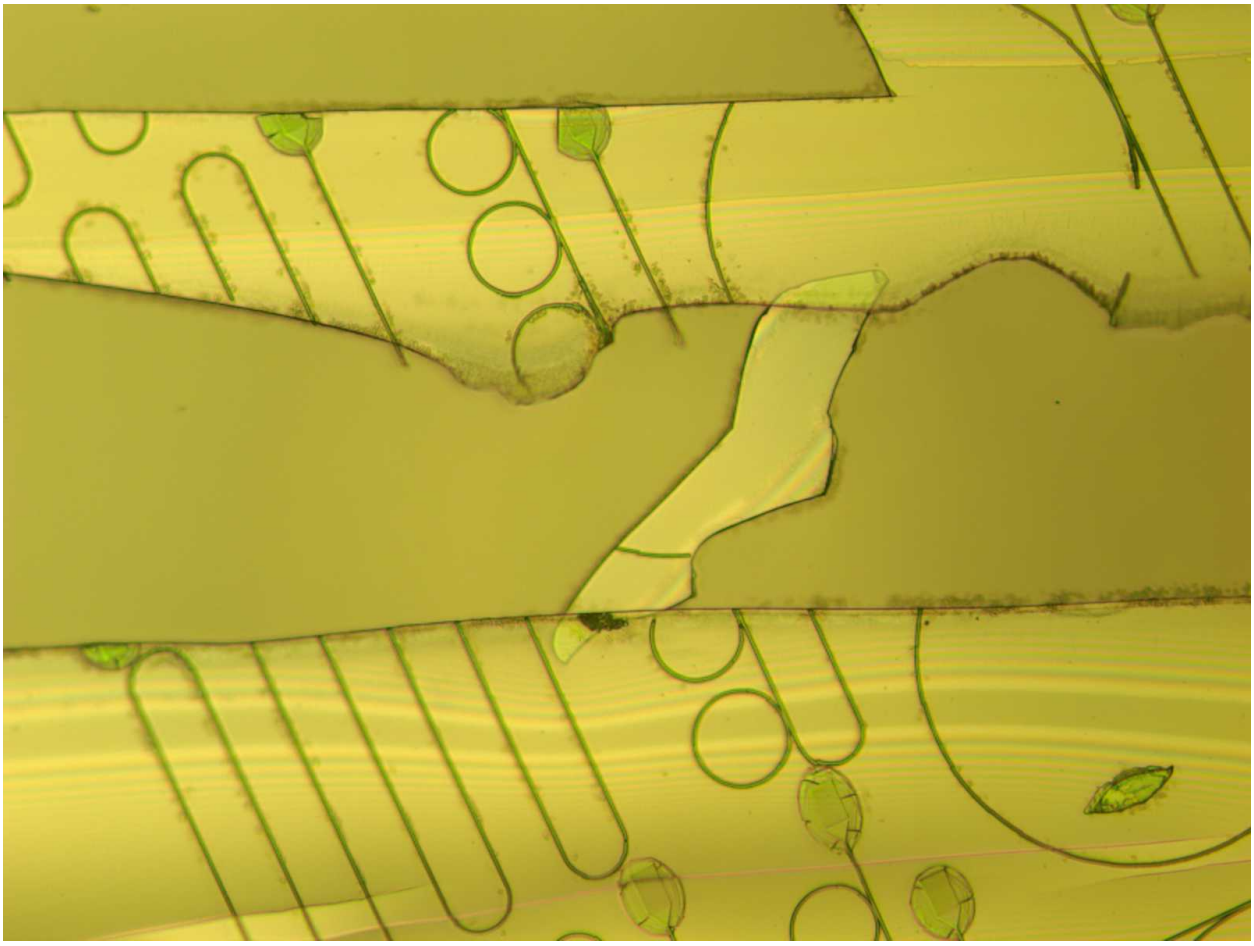

Figure 3.8. LNOI sample annealed at 600˚C, showing cracks and damage on the LN layer

3.3.2 Emission of Yb^{3+} ions

To characterize optical properties of Yb^{3+} ions, we measure the room temperature photoluminescence spectrum of Yb^{3+} ions in a 1.3cm-long LN waveguide (top image of Fig. 3.3.(a)). Similar to the previous chapter 2.3.2, We use light at 918nm as the pump which is pulsed for 3ms using an acousto-optic modulator (AOM). To filter the leakage of the pump light, we use a 1000nm edge filter at the output of the chip. The emitted signal is, then, connected to the spectrometer to detect the PL spectrum of the emitted photons from the Yb^{3+} ions in the cm-long LN waveguide. The emited photoluminescence spectrum of Yb^{3+} ions are shown in the Fig. 3.10. The excited Yb^{3+} ions decay from $^2F_{5/2}$ to $^2F_{7/2}$ via various transitions, as shown in the Fig. 3.6.

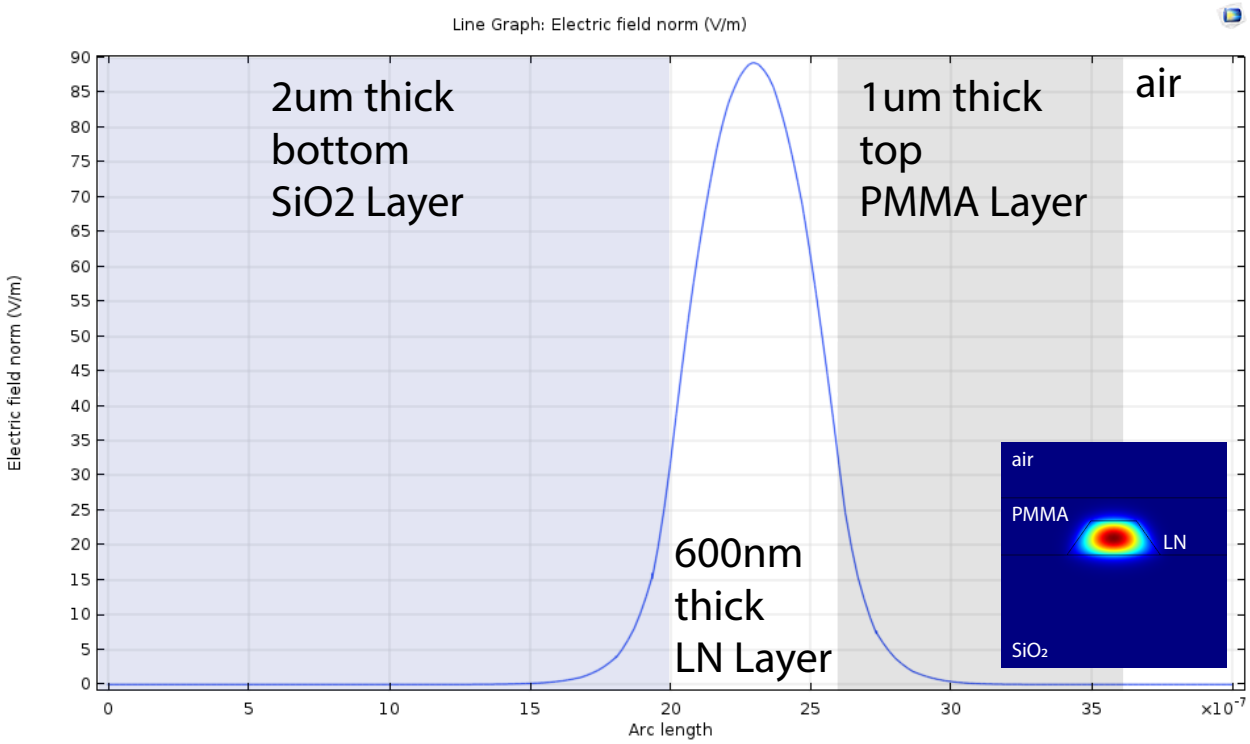

Figure 3.9. TE electric field amplitude distribution in the waveguide

The chip is cooled to 4K using a table top cryostat (Montana Instrument). To measure the PL lifetime using a single photon detector, the pump is pulsed for 3ms before collecting PL light. To perform resonant PL excitation, the 1000nm edge filter is removed. Fig. 3.11.(a) shows that PL lifetime shortened slightly when resonator is pumped on resonant compared to non-resonant pumping. The non-resonant PL lifetime of 0.50ms agrees with values obtained from bulk crystals [50] annealed at higher temperatures, suggesting negligible non-radiative decay of ions.

We attribute the lifetime shortening of the resonant PL to Purcell-enhanced emission. The average Purcell factor induced by the cavity (τ_{nr}/τ_r - 1) is about 0.45. The theoretical maximum Purcell factor taking into account the E-field at the location of the ions is about 1.12, calculated by the equation 4.24. Here, since only specific transitions of the ions are enhanced by the cavity, the branching ratio β, the probability of atoms decaying to a specific state, should be considered to the equation. The exact value of β in our case is not known and hard to calculate because of lack of information. So we attribute the discrepancy between

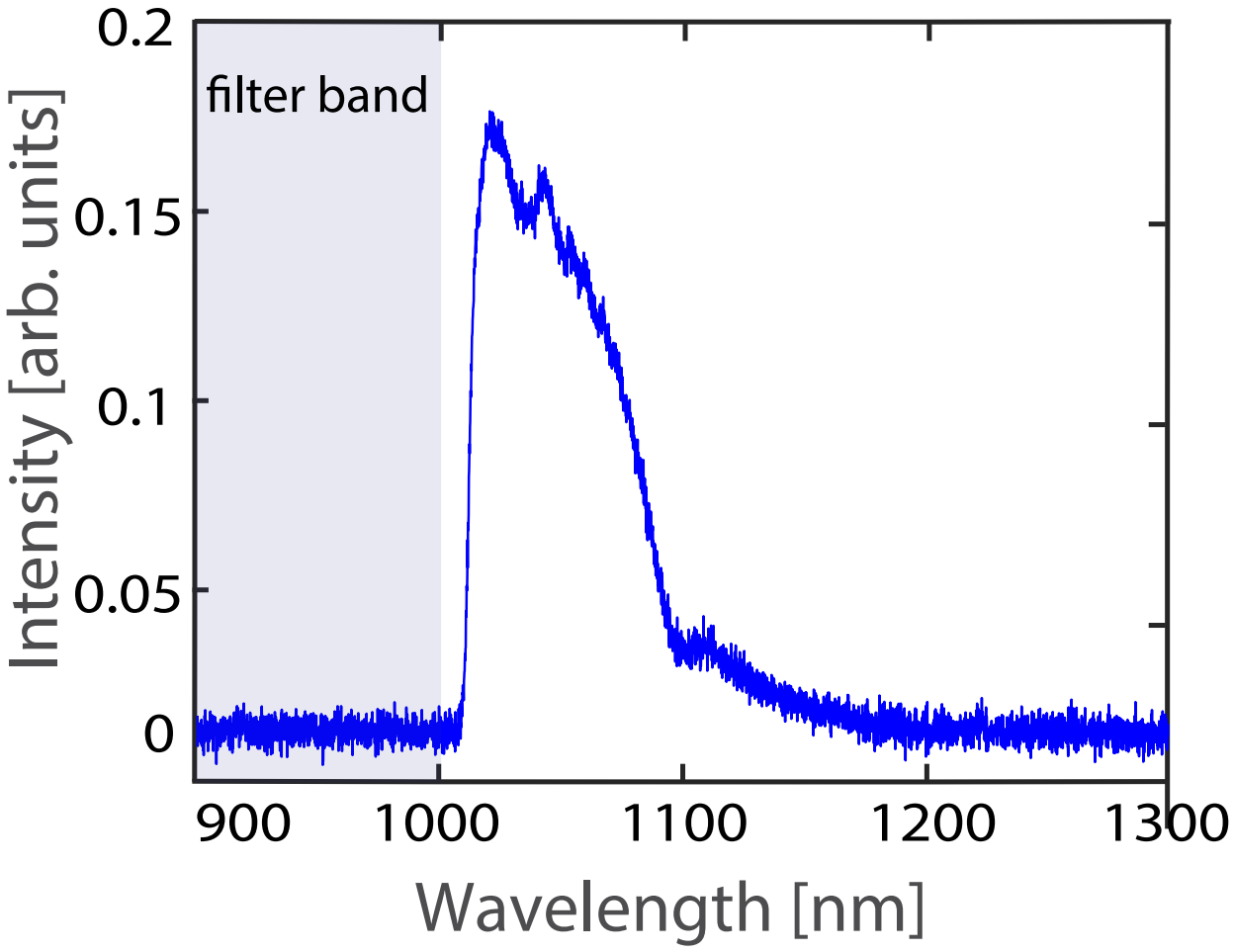

Figure 3.10. The room temperature PL spectrum of Yb^{3+} ions implanted in cm-long LN waveguides. The edge-filter filters out sub-1000nm wavelengths. Reproduced from D. Pak *et al.*, J. Appl. Phys. **128**, 084302 (2020), with the permission of AIP Publishing.

the experimental value and the theoretical value of Purcell factor to the branching ratio and the variation of ions' position.

$$F_p = \frac{3}{4\pi^2}(\frac{\lambda}{n})^3(\frac{Q}{V})(|\frac{E(r_{yb})}{E(peak)}|)^2 \tag{3.1}$$

Fig. 3.11.(b) shows the measured lifetime as a function of pump frequency with respect to the cavity resonance where the shortest lifetime was observed near resonance. The single-exponential decay of PL light (Fig. 3.11.(a)) and the trend of frequency-dependent lifetime

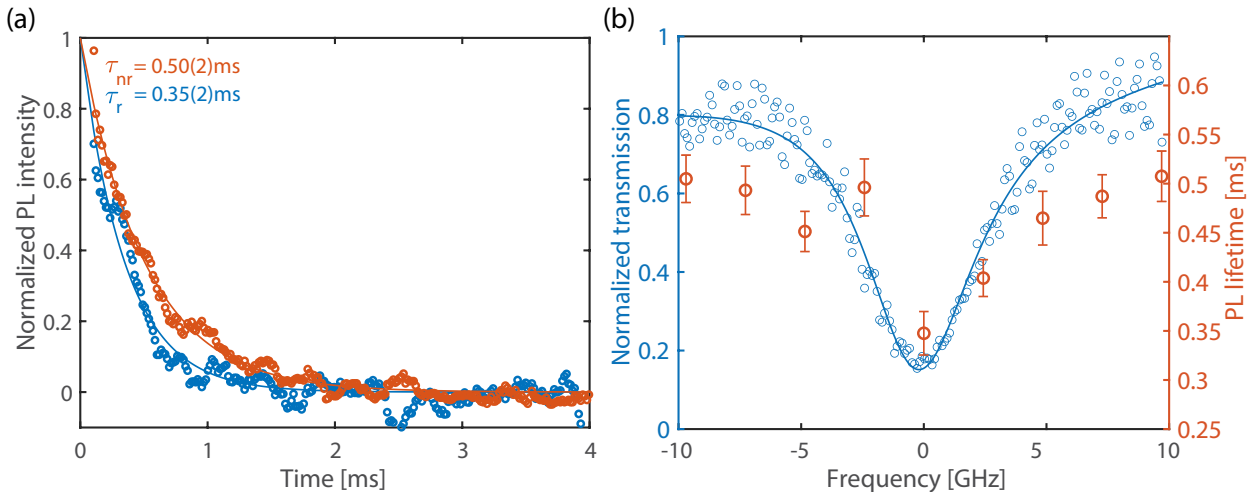

Figure 3.11. (a) Two PL decay curves of Yb^{3+} ions measured at 4K from the LN ring resonator are shown. The red data correspond to the PL decay with pump detuned by 10GHz from the cavity resonance around 920nm while the blue data correspond to the PL decay using resonant pump. The fitted lifetime of the non-resonant and resonant decays are 0.50ms and 0.35ms, respectively; (b) The transmission signal of 919nm cavity resonance (blue data) and the corresponding PL lifetime (red data) are shown as a function of pump frequency detuning with respect to the cavity resonance. Reproduced from D. Pak *et al.*, J. Appl. Phys. **128**, 084302 (2020), with the permission of AIP Publishing.

(Fig. 3.11.(b)) indicate negligible effect from the atoms in the bus waveguide. In order to further investigate the cavity effect, the total PL counts measurement was conducted on 919nm cavity dip. We detected more total PL emission counts when the pump is resonant with the resonator as shown in Fig. 3.12. It is because of increased intra-cavity pump power on resonance.

We note that the ring in this case is over-coupled and it is not designed to achieve highest Purcell factor. Although an order of magnitude higher Purcell factor is achievable by going to the under-coupled regime, we chose this regime to study critical coupling condition modified by atoms as described below.

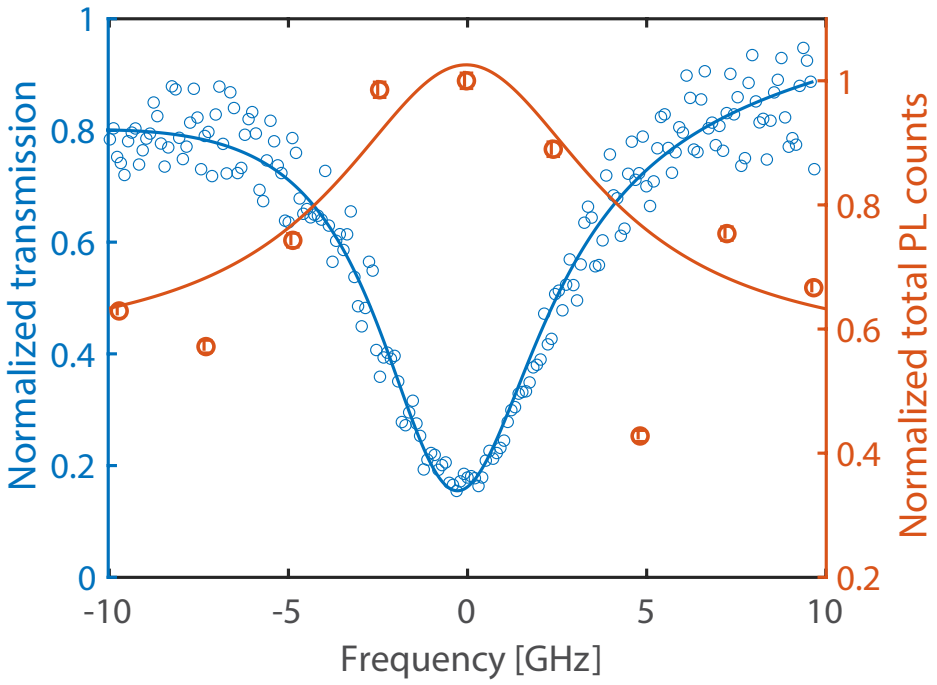

Figure 3.12. The normalized transmission signal of 919nm cavity dip (blue curve) and the corresponding normalized total PL counts (red curve)

3.3.3 Absorption effect by Yb^{3+} ions

Similar experiment as in 2.3.3 has been done to study the role of atoms in impedance-matched cavity in the LN ring resonator. We observe that the minimum transmission of the cavity (T_{min}) around 918nm, where Yb^{3+} absorption is expected, is much smaller than the minimum transmission away from that transition. This is attributed to the atom-induced absorption and thus change of the effective optical depth (Fig. 3.13.(a)). In Fig 3.13.(b), the blue dots show the intrinsic resonator Q factor as a function of wavelength at which cavity linewidth is measured. We measure the resonator linewidth for the fundamental TE mode at almost every free-spectral range (FSR) and plot the quality factor.

The electric-dipole selection rules for Yb^{3+} in LN crystal indicate that the E-field polarized perpendicular to the crystal c axis is σ polarized and the E-field polarized parallel to the c axis is π polarized [41]. As our LNOI wafer is z-cut and crystal c axis is aligned with the z axis, the TE mode excites the σ transition, which is slightly stronger than π around 919nm.

From the Q value data in Fig. 3.13.(b), we see that the atomic absorption takes place around 920nm. The red data indicate the relative contrast (or reduced transmission, $1-T_{min}$) as a function of wavelength. In the over-coupled regime, as the intra-cavity light frequency approaches the atomic transition, the atom-induced loss is expected to bring the resonator closer to the critical coupling regime. The results in Fig. 3.13.(a) and .(b) show that the intrinsic Q and also minimum transmission drop near the atomic resonance.

Using the equation 2.2, the minimum transmission can be calculated in this case well. By fitting the data in Fig. 3.13.(b) and appropriately weighting the errors, we infer $\kappa_e/(\kappa_c + \alpha_{max}) \simeq 4$. Because of the 55° sidewall angle of LN waveguide, the gap between the ring and the bus waveguide has changed from our original design, which changed our initial

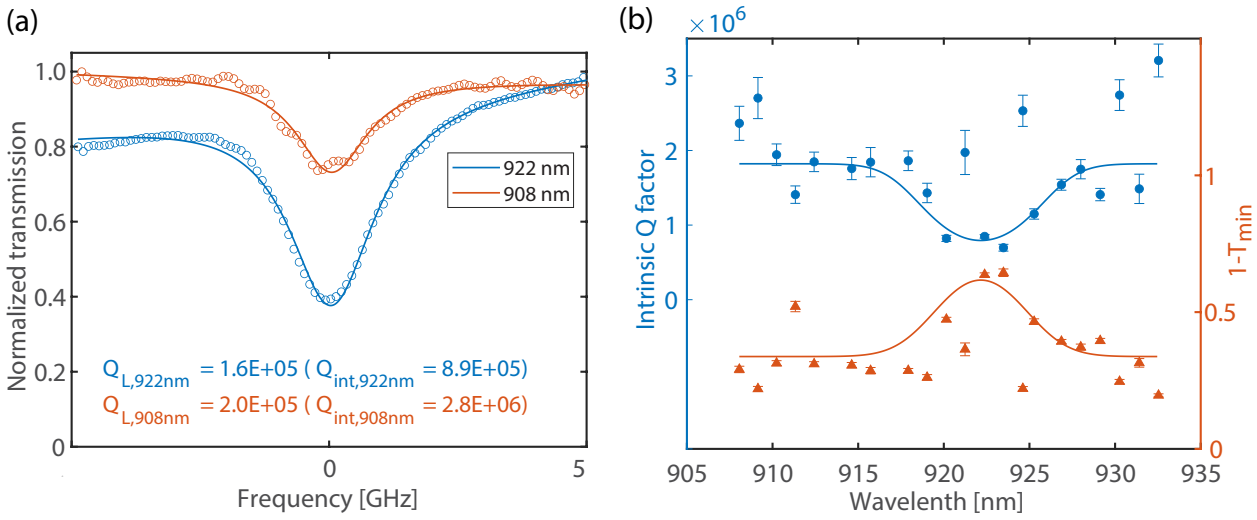

Figure 3.13. (a) Cavity transmission signals centered around 908nm and 922nm. The data show that the intrinsic quality factor at 922nm is about 3 times smaller than the intrinsic Q value at 908nm due to the atomic induced absorption; (b) The blue dots show the intrinsic quality factor vs wavelength suggesting that the quality factor decreases around the expected Yb^{3+} transition. The red dots show the contrast or the minimum transmission at the cavity resonance (T_{min}) as a function of wavelength indicating the effect of atoms in reaching near-critical coupling condition. The large errorbars in some data points are the result of light-to-chip coupling fluctuations inside the cryostat. Reproduced from D. Pak *et al.*, J. Appl. Phys. **128**, 084302 (2020), with the permission of AIP Publishing.

calibration. Using this calibration, the exact critical coupling condition, $\kappa_e = \kappa_c + \alpha(\lambda)$, can be engineered by careful design of the waveguide-ring gap and/or density of atoms.

3.4 Conclusion

In this chapter, we introduce a fabrication method for fully-etched thin-film LN micro-ring resonators and carry out implantation of Yb^{3+} ions in the LN structures. After post-implantation annealing, the loaded optical quality factor of the resonator reaches 2×10^5 (intrinsic Q $>2 \times 10^6$) and we investigate the emission spectrum and population lifetime of Yb^{3+} ions in the cm-long waveguides and micro-resonators, respectively. We find that the PL decay of Yb^{3+} ions are Purcell-enhanced when resonantly pumped, which indicates increased light-atom interactions in the cavity. Moreover, we observe atomic absorption by probing the cavity Q as a function of wavelength and study the role of atoms in designing impedance-matched resonators around one of the Yb^{3+} absorption transitions.

We note that in the case of memories based on atomic ensembles in cavities, critical coupling condition is more desirable than the strong coupling condition. In the case of an atomic ensemble, even a small single-atom cooperativity can give rise to large collective cooperativity and thus strong cavity blocking effect, which results in inefficient storage. The near-impedance matched or critically coupled cavity designed here can be used for efficient and on-chip storage of quantum optical data [19] while fast tuning of resonant frequency via the electro-optical effect of LN [76] can be used to control the storage time of the memory. Moreover, precision implantation of arrays of ions in crystalline micro-resonators may enable study of ensemble effects to control loss, absorption and emission [45], [77].

4. LONG-RANGE COOPERATIVE RESONANCES IN RARE-EARTH ION ARRAYS INSIDE PHOTONIC RESONATORS

Credit line - Material of this chapter is from: 'Pak, D., Nandi, A., Titze, M. *et al.*, Long-range cooperative resonances in rare-earth ion arrays inside photonic resonators, Commun Phys **5**, 89 (2022), Springer Nature'

4.1 Introduction

Engineering interaction Hamiltonian of photons with an ensemble of atoms or defect centers in solid-state photonics is of great interest from both fundamental and applied aspects. Recent advances in ion implantation enable deterministic engineering of multiple or arrays of ions in the crystalline matrix [45], [78]. In the case of long one-dimensional arrays, the ability to control collective dynamics in such mesoscopic systems can lead to suppression of spontaneous emission and losses in the ensemble [79]. The rich physics of many-body interactions in these systems may lead to the discovery of new interaction regimes in solids for nonlinear quantum photonic applications such as on-chip photon-atom entanglement. The implementation of collective interactions in solid-state photonics can also help to overcome fundamental limitations of the current quantum communication devices stemming from probabilistic and not-scalable entangling interactions [80].

It has been proposed that cooperative modes within emitter arrays can be harnessed to mediate tunable, long-range interactions between other impurities coupled to the chain [81]. In the cooperative regime, the strength of absorption or emission can scale quadratically with the atom number [82]. By tuning the inter-atomic separation, the dispersion relation can be engineered to observe localized photonic states. There has been limited research investigating collective interactions of light with solid-state emitters. The inhomogeneous broadening of optical transitions in solids and the lack of ability to deterministically control emitters' locations and ensemble geometry had so far limited realization of controllable collective

interactions in solid-state photonics. It has been shown that emission lifetime can change depending on the local concentrations of quantum dots and defects in diamond [83], [84].

Rare-earth ions (REIs) in crystalline solids exhibit inhomogeneous broadening as low as 10 MHz [48], [85], [86] compared to 0.1-1 THz for defects in diamonds and quantum dots. Unlike defect centers and quantum dots, REIs are actual atoms with sub-nanometer footprints, and thanks to their internal electronic structures, the atomic excitations are relatively insensitive to the environment. These unique properties together with the telecom-band optical transitions of some REIs are of important interest for quantum applications, in particular, in quantum light storage [10], [20], [87], [88] and microwave-to-optical transduction [24], [25]. To date, world-record coherence time has been observed in rare-earth crystals exceeding 6 hours [18]. The weak optical transition strength in REIs, however, prevents efficient optical pumping to a particular ground sub-level as the ground-state population lifetime is comparable to the excited state decay time. For this reason, nanophotonic cavities integrated on bulk yttrium orthosilicate (YSO) crystals have been considered to introduce Purcell enhancement of emission to improve the preparation efficiency [26], [88], [89]. This approach has resulted in enhancement factors of 700 [26], however, with the price of reducing the bandwidth and number of atoms available for interactions.

Integrated solid-state photonics based on silicon or lithium niobate (LN) materials provide salable platforms as hosts for REIs. Ion implantation in photonic materials has shown remarkably low inhomogeneous and homogeneous broadenings [3], [90], [91]. We have previously shown that it is possible to arrange REIs into an ordered array inside silicon nitride photonic resonators [45]. Integrating REIs with nonlinear crystals such as LN has also been demonstrated [42], [68], [69]. The LN photonic devices integrated with REIs can be promising candidates for multi-functional quantum optical devices where quantum light generation [92], storage [10], modulation [93], and wavelength conversion [67] can all occur within the same device.

When an ensemble of REIs inside micro-ring resonators forms an ordered array, in certain parameter regimes, ions can cooperatively interact with light [94]. In this regime, absorption and directional emission can increase without increasing the ion concentration. This is important because, in the case of REIs, high concentration leads to undesirable strong ion-

ion interactions. This induces spin diffusion and dephasing [73], lowering the coherence time of ions. In contrast, the cooperative interaction enables strong and broadband light-atom interactions at not-high atomic densities. Moreover, enhanced emission in this regime leads to increased pumping efficiency that can enable efficient quantum storage of light without affecting the memory bandwidth. The cooperative effect can also reduce the loss and increase the storage fidelity. For example, the emergence of dark states due to the coherent spin-spin interaction can be a promising candidate for photonic quantum memories [95]. When far from saturation, the collective effects are expected to lead to a memory unit with minimized transport and dephasing loss.

To deterministically create ion arrays, we use precision ion implantation. We select isotopically pure $^{169}Tm^{2+}$ ions using a velocity selector (Wien filter) and use a focused ion beam (FIB) to implant ions with a beam spot size of 37 nm $\times$ 36 nm. Rare-earth Tm^{2+} change to Tm^{3+} after annealing. As the result, ions are localized in a segment of width and depth of about 36 nm across the waveguide as shown in Fig. 4.4(a). The spatial and frequency spread of ions in each segment can be described by semi-Gaussian distributions. By repeating the implantation in multiple segments around the micro-ring, ordered arrays (with regular segment spacing) and disordered arrays (with random segment spacing) can be created. Although ions in each segment have different frequencies due to the inhomogeneous broadening, resonant excitation and resonant photoluminescence help to study the interaction of a narrow frequency class of ions. Moreover, Tm^{3+} are non-Kramers REIs in the crystalline matrix with the ability to, in principle, reach long coherence times as shown for other non-Kramers ions [18]. Also, the presence of optical transitions at both 0.8 µm and 1.6 µm enables applications in quantum communication for both free-space and fiber channels. Here, lithium niobate-on-insulator (LNOI) materials are chosen as the host materials for their multi-functional properties [96] and ease of nanofabrication [9], [28] compared to other crystalline hosts. The applications of Tm-incorporated lithium niobate waveguides for integrated optical and quantum photonics have been highlighted by recent experimental studies [69], [97].

4.2 Theory of collective emission from atomic arrays in micro-ring resonators

I would like to acknowledge that the following theory in sub-chapter 4.2 was developed with the help of Prof. Hadiseh Alaeian in ECE/Physics at Purdue University.

Figure 4.1 shows the system considered to devise a model describing light-atom interactions within an emitter array [98].

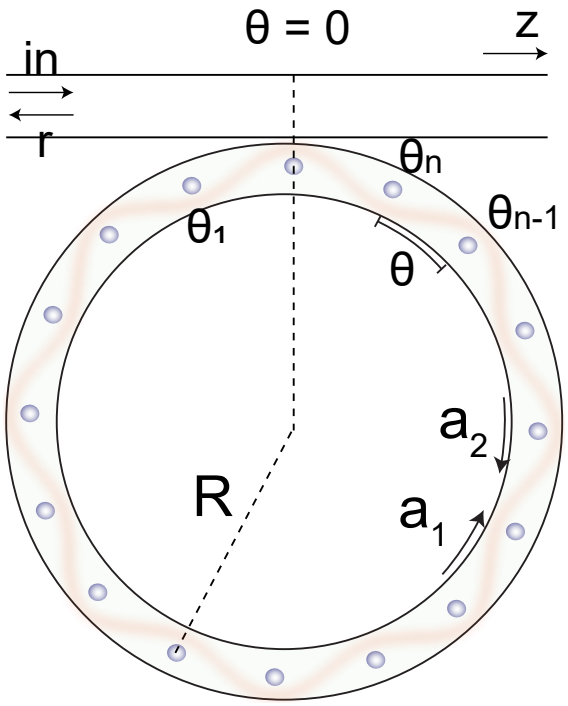

Figure 4.1. Schematic figure of a ring resonator hosting periodic arrays of atomic segments. Material from: 'Pak, D. *et al.*, Long-range cooperative resonances in rare-earth ion arrays inside photonic resonators, Commun Phys **5**, 89 (2022), Springer Nature'.

From Fig. 4.1, $\theta_{\rm i}$ refers to the location of ion segments in the ring resonator, and clockwise (CW) and counter-clockwise (CCW) modes are considered to be degenerate with field operators $\hat{A}_1(\theta,t)$, $\hat{A}_2(\theta,t)$, respectively. Via Fourier decomposition these field operators can be written in the momentum space as

$$\hat{A}_n(\theta,t) = \frac{1}{\sqrt{2\pi}}\int_0^\infty dk\ \hat{a}_n(k,t)\mathrm{e}^{\pm \mathrm{i}kR\theta}, \tag{4.1}$$

where $\pm$ refers to the CCW and CW modes, respectively.

Here, we write the mode in its most general form as a continuum. Considering the periodic boundary condition, i.e. $2\pi kR = 2\pi N \Rightarrow kR = N$, ($N$ = 1,2,3, $\cdots$), cavity resonance modes can be obtained.

To derive the ion spins and photonic modes equations of motion we use the density matrix formalism as $\dot{\rho} = -\mathrm{i}[\hat{H}, \rho] + D(\hat{\rho})$. Within the validity range of the rotating wave approximation (RWA), the Hamiltonian of an N-spin array coupled to the CW and CCW cavity modes will be given as

$$\begin{aligned}\hat{H} = &\int_0^\infty dk\ \omega_0(k)\ \{\hat{a}_1^\dagger(k,t)\hat{a}_1(k,t) + \hat{a}_2^\dagger(k,t)\hat{a}_2(k,t)\}\ +\ \omega_a \sum_{n=1}^{N} \hat{\sigma}_{\mathrm{ee}}^{(n)}(t) \\ &+\ g_0 \sum_{n=1}^{N} \hat{\sigma}_{\mathrm{eg}}^{(n)} \int_0^\infty dk\{\hat{a}_1(k,t)\mathrm{e}^{\mathrm{i}kR\theta} + \hat{a}_2(k,t)\mathrm{e}^{-\mathrm{i}kR\theta}\} \\ &+\ g_0 \sum_{n=1}^{N} \hat{\sigma}_{g\mathrm{e}}^{(n)} \int_0^\infty dk\{\hat{a}_1^\dagger(k,t)\mathrm{e}^{\mathrm{i}kR\theta} + \hat{a}_2^\dagger(k,t)\mathrm{e}^{-\mathrm{i}kR\theta}\},\end{aligned} \tag{4.2}$$

and the dissipation reads as

$$\begin{aligned}D(\hat{\rho}) = &\frac{\Gamma_0}{2} \sum_{n=1}^{N} (2\sigma_{g\mathrm{e}}^{(n)} \rho \sigma_{\mathrm{eg}}^{(n)}\ -\ \{\sigma_{\mathrm{ee}}^{(n)}, \rho\}) \\ &+\ \frac{\kappa}{2}(2\hat{a}_1 \rho \hat{a}_1^\dagger - \{a_1^\dagger a_1, \rho\}) \\ &+\ \frac{\kappa}{2}(2\hat{a}_2 \rho \hat{a}_2^\dagger - \{a_2^\dagger a_2, \rho\}),\end{aligned} \tag{4.3}$$

where $\omega_0(k)$ is the mode dispersion, $\hat{\sigma}_{\mathrm{eg}}^{(n)}$ is the n^{th} spin rising operator, g_0 is the vacuum Rabi coupling, and Γ_0 and κ are decay rates of the spin to non-cavity modes and cavity decay rate, respectively. We assume the vacuum Rabi frequency g_0 is the same for all atoms and we ignore vacuum-induced dipole-dipole interactions.

In the Heisenberg picture, the equations of motion for the photonic fields can be determined as

$$\frac{\mathrm{d}}{\mathrm{d}t}\hat{a}_1(k,t)\ =\ -\mathrm{i}\left(\omega_0(k) - \mathrm{i}\frac{\kappa}{2}\right)\ \hat{a}_1(k,t)\ -\ \mathrm{i}g_0 \sum_{m=1}^{N} \hat{\sigma}_{g\mathrm{e}}^{(m)}(t)\ \mathrm{e}^{-\mathrm{i}kR\theta_m} \tag{4.4}$$

$$\frac{\mathrm{d}}{\mathrm{d}t}\hat{a}_2(k,t) \;=\; -\mathrm{i}\left(\omega_0(k) - \mathrm{i}\frac{\kappa}{2}\right)\,\hat{a}_2(k,t) \;-\; \mathrm{i}g_0\sum_{m=1}^{N}\hat{\sigma}_{ge}^{(m)}(t)\,\mathrm{e}^{+\mathrm{i}kR\theta_m} \tag{4.5}$$

In equations 4.4 and 4.5, the first term describes the free evolution of the field operator and the second term contains the effect of spin radiated photons in modifying the cavity fields. Furthermore, the spin coherence evolves as

$$\begin{aligned}\frac{\mathrm{d}}{\mathrm{d}t}\hat{\sigma}_{ge}^{(n)}(t) \;=\; & -\mathrm{i}\left(\omega_a - \mathrm{i}\frac{\Gamma_0}{2}\right)\,\hat{\sigma}_{ge}^{(n)}(t) \\ & +\; \mathrm{i}g_0\left(\hat{\sigma}_{ee}^{(n)} - \hat{\sigma}_{gg}^{(n)}\right)\int_0^\infty dk\,\{\hat{a}_1(k,t)\mathrm{e}^{\mathrm{i}kR\theta_n} + \hat{a}_2(k,t)\mathrm{e}^{-\mathrm{i}kR\theta_n}\}\end{aligned} \tag{4.6}$$

Here in the equation 4.6, the first term describes the free-atom evolution and the second term describes the driven atom dynamics.

To obtain a spin model solely based on atomic degrees of freedom (DoF), we integrate out the photonic DoF as in equations 4.4 and 4.5 to obtain

$$\hat{a}_1(k,t) \;=\; \hat{a}_1(k,0)\,\mathrm{e}^{-\mathrm{i}\left(\omega_0(k)-\mathrm{i}\frac{\kappa}{2}\right)t} \;-\; \mathrm{i}g_0\sum_{m=1}^{N}\mathrm{e}^{-\mathrm{i}kR\theta_m}\int_0^t dt\;\hat{\sigma}_{ge}^{(m)}(t)\mathrm{e}^{-\mathrm{i}\left(\omega_0(k)-\mathrm{i}\frac{\kappa}{2}\right)(t-t)} \tag{4.7}$$

$$\hat{a}_2(k,t) \;=\; \hat{a}_2(k,0)\,\mathrm{e}^{-\mathrm{i}\left(\omega_0(k)-\mathrm{i}\frac{\kappa}{2}\right)t} \;-\; \mathrm{i}g_0\sum_{m=1}^{N}\mathrm{e}^{+\mathrm{i}kR\theta_m}\int_0^t dt\;\hat{\sigma}_{ge}^{(m)}(t)\mathrm{e}^{-\mathrm{i}\left(\omega_0(k)-\mathrm{i}\frac{\kappa}{2}\right)(t-t)} \tag{4.8}$$

The last term $\mathrm{e}^{-\mathrm{i}\left(\omega_0(k)-\mathrm{i}\frac{r}{2}\right)(t-t)}$ in equation 4.7 and 4.8 is the total delayed scattered field of each spin in the chain. From equation 4.7 and 4.8, we can determine the field operators via the inverse Fourier transform:

$$
\begin{aligned}
\hat{A}_1(\theta,t) &= \frac{1}{\sqrt{2\pi}}\int_0^k dk\ \hat{a}_1(k,t)\mathrm{e}^{\mathrm{i}kR\theta} \\
&= \frac{1}{\sqrt{2\pi}}\int_0^\infty dk\ \mathrm{e}^{-\frac{\kappa}{2}t}\mathrm{e}^{\mathrm{i}(kR\theta-\omega_0(k)t)}\ \hat{a}_1(k,0) \\
&- \mathrm{i}\frac{g_0}{\sqrt{2\pi}}\sum_{m=1}^{N}\int_0^t dt\hat{\sigma}_{\mathrm{ge}}^{(m)}(t)\ \mathrm{e}^{-\frac{\kappa}{2}(t-t)}\ \int_0^\infty dk\ \mathrm{e}^{\mathrm{i}((\theta-\theta_m)kR-\omega_0(k)(t-t))}
\end{aligned}
\tag{4.9}
$$

Assume a linear mode dispersion with the phase velocity of v_p we have $\omega_0(\mathrm{k}) = \pm v_p k$, where + means CCW, - means CW, respectively. Unless close to the mode cutoff, a linear dispersion is quite valid assumption.

With this assumption, the field operator is simplified to:

$$
\begin{aligned}
\hat{A}_1(\theta,t) &= \mathrm{e}^{-\frac{\kappa}{2}t}\ \hat{A}_1^{(\mathrm{in})}\ (\theta-\frac{v_p}{R}t)\ -\ \mathrm{i}g_0\ \sum_{m=1}^{N}\int_0^t dt\hat{\sigma}_{\mathrm{ge}}^{(m)}(t)\mathrm{e}^{-\frac{\kappa}{2}(t-t)}\delta(v_pt-v_pt+R(\theta-\theta_m)) \\
&= \mathrm{e}^{-\frac{\kappa}{2}t}\ \hat{A}_1^{(\mathrm{in})}\ (\theta-\frac{v_p}{R}t) - \frac{\mathrm{i}g_0}{v_p}\ \sum_{m=1}^{N}\int_0^t dt\hat{\sigma}_{\mathrm{ge}}^{(m)}(t)\mathrm{e}^{-\frac{\kappa}{2}(t-t)}\delta(t-(t-\frac{R(\theta-\theta_m)}{v_p})) \\
&= \mathrm{e}^{-\frac{\kappa}{2}t}\ \hat{A}_1^{(\mathrm{in})}\ (\theta-\frac{v_p}{R}t) - \frac{\mathrm{i}g_0\sqrt{2\pi}}{v_p}\ \sum_{m=1}^{N}\ \Theta(\theta-\theta_m)\mathrm{e}^{-\frac{\kappa}{2}\frac{R}{v_p}(\theta-\theta_m)}\ \hat{\sigma}_{\mathrm{ge}}^{(m)}(t-\frac{R}{v_p}(\theta-\theta_m))
\end{aligned}
\tag{4.10}
$$

Similarly, for the CW cavity field operator, we have

$$
\hat{A}_2(\theta,t) = \mathrm{e}^{-\frac{\kappa}{2}t}\ \hat{A}_2^{(\mathrm{in})}\ (\theta+\frac{v_p}{R}t) - \frac{\mathrm{i}g_0\sqrt{2\pi}}{v_p}\ \sum_{m=1}^{N}\ \Theta(\theta_m-\theta)\mathrm{e}^{-\frac{\kappa}{2}\frac{R}{v_p}(\theta-\theta_m)}\ \hat{\sigma}_{\mathrm{ge}}^{(m)}(t+\frac{R}{v_p}(\theta-\theta_m))
\tag{4.11}
$$

In equations 4.10 and 4.11, the terms $\mathrm{e}^{-\frac{\kappa}{2}t}\ \hat{A}_{1,2}^{(\mathrm{in})}\ (\theta\mp\frac{v_p}{R}t)$, describe the delayed and attenuated input fields, and $\Theta(\theta_m-\theta)$ is the Heaviside function. Further, $\mathrm{e}^{-\frac{\kappa}{2}\frac{R}{v_p}(\theta-\theta_m)}$ in the spin scattered field contributions describes the attentuation of these cavity fields, and the last term in the form of $(t+\frac{R}{v_p}(\theta-\theta_m))$ corresponds to the delayed contribution of each spin to the total field.

Using the equations 4.6-4.10 , we can now write the equation of motion for atomic coherence as:

$$\begin{aligned}\frac{\mathrm{d}}{\mathrm{d}t}\hat{\sigma}_{ge}^{(n)}(t) &= -\mathrm{i}\left(\omega_a - \mathrm{i}\frac{\Gamma_0}{2}\right)\hat{\sigma}_{ge}^{(n)}(t) \\ &+ \mathrm{i}g_0\sqrt{2\pi}\,\mathrm{e}^{-\frac{\kappa}{2}}\,[\hat{A}_1^{(in)}(\theta_n - \frac{v_p}{R}t) + \hat{A}_2^{(in)}(\theta_n + \frac{v_p}{R}t)]\hat{\sigma}_z^{(n)} \\ &+ \frac{2\pi g_0^2}{v_p}\hat{\sigma}_z^{(n)}\sum_{m=1}^{N}\mathrm{e}^{-\frac{\kappa}{2}\frac{R}{v_p}|\theta_n-\theta_m|t}\,\hat{\sigma}_{ge}^{(m)}\,(t - \frac{R}{v_p}|\theta_n - \theta_m|),\end{aligned} \tag{4.12}$$

where $\hat{\sigma}_z^{(n)} \equiv \hat{\sigma}_{ee}^{(n)} - \hat{\sigma}_{gg}^{(n)}$ is the spin inversion.

The first line of the equation 4.12 describes the free-atom evolution. The second line explains the role of the input excitation in the nth atom dynamics. The third line describes all contributions from the spins in the chain via local modification of the Rabi frequency.

In the case of one-sided excitation, i.e., $A_2^{(in)} = 0$, with a coherent laser at frequency ω_0 and the momentum k_0, we can rewrite the equation 4.12 in the laser frame by removing $\mathrm{e}^{\mathrm{i}\omega_0 t}$ dependency. Furthermore, employing the Markovian approximation, the the delayed polarization can be simplified as

$$\hat{\sigma}_{ge}^{(m)}(t - \frac{R}{v_p}|\theta_n - \theta_m|) \approx \hat{\sigma}_{ge}^{(m)}(t)\mathrm{e}^{\mathrm{i}k_0 R|\theta_n-\theta_m|} \tag{4.13}$$

Finally, we arrive at the simplified effective spin equation of motion as

$$\begin{aligned}\frac{\mathrm{d}}{\mathrm{d}t}\hat{\sigma}_{ge}^{(n)}(t) &= -\mathrm{i}\left(\delta - \mathrm{i}\frac{\Gamma_0}{2}\right)\hat{\sigma}_{ge}^{(n)}(t) \\ &+ \mathrm{i}g_0\sqrt{2\pi}\,\hat{\sigma}_z^{(n)}\,\mathrm{e}^{-\frac{\kappa}{2}t}\,E_0\mathrm{e}^{\mathrm{i}k_0 R\theta_n} \\ &+ \frac{2\pi g_0^2}{v_p}\,\hat{\sigma}_z^{(n)}\sum_{m=1}^{N}\mathrm{e}^{-\frac{\kappa}{2}\frac{R}{v_p}|\theta_n-\theta_m|t}\,\mathrm{e}^{\mathrm{i}k_0 R|\theta_n-\theta_m|}\,\hat{\sigma}_{ge}^{(m)}(t)\,,\end{aligned} \tag{4.14}$$

where $\delta = \omega_a - \omega_0$ is the detuning.

In the Eq (4.14), the 1st line is free-atom evolution, the 2nd line is the evolution due to the laser field, and the 3rd line means that atoms become polarized and scatter the intra-cavity light such that the local field at m-th atom segment is modified. This can be seen as an effective interaction between atomic segments mediated via the cavity modes. Note that in considering the input field contributions shown in the second line of Eq (4.14), we implicitly assumed a strong coherent field whose quantum fluctuations can be ignored.

We note that the term $e^{ikR|\theta_n-\theta_m|}$ is complex suggesting the total field both has a coherent and an incoherent effect. In the limit of $N = 1$, the spin's radiated field and its coupling to the cavity modify the local field, which indeed is the Purcell factor.

Equation 4.14 can be used to determine the waveguide-mediated Green's function. From the most general form of the spin model we have [99]

$$\begin{aligned} \hat{H} &= H_F + \sum_{m,n} \frac{J_{mn}}{2}(\sigma_{eg}^{(m)}\sigma_{ge}^{(n)} + h.c.) \\ D(\hat{o}) &= \sum_{m,n} \frac{\Gamma_{mn}}{2}(2\sigma_{eg}^{(m)}\hat{o}\sigma_{ge}^{(n)} - \{\sigma_{eg}^{(m)}\sigma_{ge}^{(n)}, \hat{o}\}) \end{aligned} \tag{4.15}$$

Here, $J_{mn} = -3\pi\Gamma_0 \mathrm{Re}(G_{mn})$, $\frac{\Gamma_{mn}}{2} = 3\pi\Gamma_0\, \mathrm{Im}(G_{mn})$, and $\hat{H}$ and $D(\hat{o})$ describe the conserved and dissipative dynamics, respectively. G_{mn} is the effective Green's function of the system. It is straightforward to see that the spins Heisenberg equations of motion are given by

$$\frac{d}{dt}\hat{\sigma}_{ge}^{(n)} = -i(\Delta - i\frac{\Gamma_0}{2})\hat{\sigma}_{ge}^{(n)} - i\Omega_n\hat{\sigma}_z^{(n)} - i\Omega_n\hat{\sigma}_z^{(n)} \sum_k (-J_{kn} + i\frac{\Gamma_{kn}}{2})\hat{\sigma}_{ge}^{(k)} \tag{4.16}$$

Furthermore, we can also derive the equation of motion for population term $\hat{\sigma}_{ee}^{(n)}(t)$:

$$\frac{d}{dt}\hat{\sigma}_{ee}^{(n)}(t) = -\Gamma_0\hat{\sigma}_{ee}^{(n)} + i\Omega_n\hat{\sigma}_{eg}^{(n)} + i\hat{\sigma}_{eg}^{(n)} \sum_m 3\pi\Gamma_0 G_{mn}\hat{\sigma}_{ge}^{(n)} + h.c. \tag{4.17}$$

If we compare Eq (4.17) with a driven single atom's Bloch equation, we can define an effective Rabi frequency as:

$$\Omega_n^{(eff)} = \Omega_0 + 3\pi\Gamma_0 \sum_m G_{mn} \langle \hat{\sigma}_{ge}^{(m)} \rangle \tag{4.18}$$

Here, the first term(Ω_0) describes the incident field and the second term describes the scattering from all atoms modifying the local field. Note the conceptual resemblance of the equation 4.18 with the classical picture of dipole-dipole interaction.

By comparing the equation 4.14 with the equation 4.16, the Green's function of the waveguide can be determined as:

$$G_R(\theta, \theta') \;=\; \mathrm{i}\,\frac{2}{3}\,\frac{g_0^2}{v_p \Gamma_0}\,\mathrm{e}^{\mathrm{i}kR|\theta-\theta'|} \tag{4.19}$$

The bare atom-light coupling rate g_0 is proportional to the square root of the atom number that is a function of position and frequency, v_p is the phase velocity, R is the ring radius, $\theta_{m/n}$ is the angular location of the ion segment in the ring, $k = 2\pi/\lambda_L$ and $\lambda_L/2$ is the lattice spacing.

Using:

$$\sum_{m=1}^{M_s} \cos\left(mkR\theta\right) = \frac{\sin^2\left(M_s kR\delta\theta\right)}{\sin^2\left(kR\delta\theta/2\right)} \tag{4.20}$$

where $\delta\theta$ is the angular spacing between two segments, we see that scattering shows oscillation with a wavelength of λ_L/M_s assuming $sin^2(kR\delta\theta/2) \simeq 1$. This is the modified field due to the other segment scattering calculated in the arrayed case. Because we have rotational symmetry, this modified factor is the same for all segments and for the ordered array it leads to an oscillatory behavior. This oscillation can be observed by either changing the

spacing between segments, e.g. $R\delta\theta$, or pumping wavelength ($R\delta\theta \equiv \lambda/2$) thanks to the inhomogeneous broadening in the system.

To delineate the single-body effect due to the cavity and the many-body effect due to the array's cooperative effects, let us consider the special case of $\sigma_{\mathrm{ee}}^{(n)} \approx 0$ (i.e. the non-depleted regime). There, we can solve the coupled spin equations in a closed-form. For simplicity we also assume $\gamma \to 0$.

From the equation 4.14 we have:

$$\begin{aligned} \frac{\mathrm{d}}{\mathrm{d}t}\langle\hat{\sigma}_{ge}^{(n)}\rangle &= \left(-\frac{\Gamma_0}{2} - \mathrm{i}\delta\right)\langle\hat{\sigma}_{ge}^{(n)}\rangle \\ &- \mathrm{i}g_0\sqrt{2\pi}E_0\mathrm{e}^{\mathrm{i}k_0R\theta_n} \\ &- \frac{2\pi g_0^2}{v_p}\sum_m \langle\hat{\sigma}_{ge}^{(m)}\rangle\mathrm{e}^{\mathrm{i}k_0R|\theta_n-\theta_m|}\,. \end{aligned} \tag{4.21}$$

The last term leads to a maximize collective effect when the scattering terms interfere constructively which for an ordered array it means, $\theta_n = n\theta_0 \Rightarrow 2kR\theta_0 = 2\pi n \Rightarrow k_0R\theta_0 = \pi n$. When plugged back into Eq (4.21) we get

$$\langle\hat{\sigma}_{ge}\rangle = -\frac{\mathrm{i}g_0\sqrt{2\pi}E_0}{-\mathrm{i}\delta + \Gamma_0/2 + \frac{2\pi g_0^2}{v_p}\eta} \tag{4.22}$$

The contribution of different phenomena is clear in the denominator of this final form. 1) The first term in $(-\mathrm{i}\delta)$ represents the detuning, 2) the second term $(\Gamma_0/2)$ describes the decay of the spin radiations to non-cavity modes, and 3) the last term $(\frac{2\pi g_0^2}{v_p}\eta)$ is the additional modification of the decay due the cavity $(\frac{2\pi g_0^2}{v_p})$ plus a collective effect scaled as η, which is related to the effective number of collective excitations.

Considering N atoms present in the system, the population of n-excited states is given by $\mathrm{P}_n = \mathrm{Tr}(\hat{P}_n\hat{\rho})$, where the density matrix $\hat{\rho} = \otimes_n(|\mathrm{e}_n\rangle\langle\mathrm{e}_n| + |g_n\rangle\langle g_n|)/2N$, and $\hat{P}_n = \Sigma_{\wp}\otimes_{\mathrm{j}=1}^{n}$ $|\mathrm{e_j}\rangle\langle\mathrm{e_j}| \otimes_{m=n+1}^{N}|\mathrm{g}_m\rangle\langle\mathrm{g}_m|$, with $\wp$ the N!/n!(N-n)! permutations of a set with n excited atoms and (N-n) in the ground state. The number of excitation is influenced by factors such as

spatial and spectral broadening. For large number of excitations $n > N/2$ the system emits superadiantly, and for $n < N/2$ subradiant decay is dominant. The lifetime of the decay linearly scales with n/N as experimentally shown in Ref. [100].

In the present case, the resonant pump excitation enables us to select a narrow frequency class of the atoms. Considering only two atoms, for simplicity, at high pump powers the system can be equally excited to one of the following states $(|\mathrm{eg}\rangle \pm |\mathrm{ge}\rangle)/\sqrt{2}$, $|\mathrm{gg}\rangle$ and $|\mathrm{ee}\rangle$. At lower pump powers, population of $|\mathrm{ee}\rangle$ state is negligible and population of $(|\mathrm{eg}\rangle \pm |\mathrm{ge}\rangle)/\sqrt{2}$ states both scale linearly with the pump power [101]. In practice, excitation of subradiant states, i.e. $(|\mathrm{eg}\rangle$ - $|\mathrm{ge}\rangle)/\sqrt{2}$ is harder in arrays [102]–[104] due to the complicated long-range interactions and many-body features of the atomic ensembles and also higher sensitivity of subradiant states to broadening in the system compared to the superradiant states. At high atom numbers, the existence of various decay paths described by the permutation in the $\hat{P}_n$ equation creates complicated dynamics between sub- and super-radiant states that are subject to variation of the driving field power [100].

As also described in Ref. [105] and considering the effective Rabi frequency above, $\Omega_n^{(eff)} = \Omega_0 + 3\pi\Gamma_0 \sum_m G_{mn} \langle \hat{\sigma}_{ge}^{(m)} \rangle$, apart from the inversion described by the first term, the pump-induced correlations between the atoms described by the second term also play a role in driving superradiant states. At low pump powers, the interaction energy prevents efficient population of subradiant states. Uniform directional pumping along the cavity axis, gives rise to correlations that grow with duration or power of the pump light. This is evidenced by the observation of pump-dependent decay time and lineshift in atomic ensembles (with random spatial distribution) [105], [106].

4.3 Device fabrication and ion implantation

The micro-ring resonators are fabricated on a 600 nm thick z-cut LNOI wafer using the same recipe described in Ref. [42]. The device pattern (bus waveguides, micro-ring resonators) is defined on an HSQ e-beam resist film by an electron beam lithography system with the dose of 2000 μC/cm^2. Then, the 600 nm LN thin-film is half-etched using an $Ar/Cl_2/BCl_3$-based recipe for waveguides and micro-ring resonators. The width of the

waveguide is 600 nm and the waveguide dimension is designed such that the fundamental TE mode is still dominant while minimizing sidewall scattering loss, a significant loss channel of the LN waveguide [28]. The ring radius used is 50 µm, and the gap between the bus waveguide and the ring resonator is 430 nm, resulting in around 60% bus-ring coupling efficiency. Also, the gap between the ring and the drop-port waveguide is 535 nm, resulting in around 10% waveguide-to-ring coupling. For precision ion implantation, the Ti/Au alignment marks are deposited by the lift-off process. 5 nm Ti layer is deposited below the 100 nm Au alignment marks as an adhesive layer. At this step, the sample is implanted with Tm^{2+} ions from Sandia National Laboratories. Finally, for stable light coupling to the waveguide, the remaining LN layer is fully etched with the same LN etching recipe, and the bottom Si layer is deep-etched (∼80 µm) by Bosch process for the fiber-to-chip coupling (U-grooves).

To verify the collective effects, we use two micro-rings, one hosting an ordered array (Fig. 4.2(a)) and one a disordered array of ion segments (Fig. 4.2(b)). The total number of ions and the total number of ion segments for both ordered and disordered samples are the same. Each ion segment has the same number of ions implanted with a fixed ion fluence. Also, both ordered and disordered samples have the same number of ion segments ($M_s = 1750$). The only difference between the two samples is the segment spacing and its regularity. In the ordered sample, the spacing is fixed and close to $\lambda_L/2n_{eff}$ while in the disordered array the spacing between ion segments varies randomly around the micro-ring resonator.

When the spacing between each ion segment is $\lambda_L/2n_{eff}$ (=184 nm), maximum cooperative interaction is expected. Because of the mismatch between the theoretical and experimental values of n_{eff}, the actual spacing between ion segments is 179.5 nm. As a reference, we also implant a ring resonator with a disordered array (with the same number of segments) where the spacing between ion segments was randomly varied for comparison. We use the focused-ion beam system in the Sandia National Laboratories with a minimum spot size as small as 10nm for implantation. In our case of Tm^{2+} implantation, the mass spectrometry was first carried out using an AuSiTm source before the implantation to select a specific isotope and ion using a combination of electric and magnetic fields (Fig. 4.3). The Tm^{2+} ions were implanted into rectangular segments of width 37 nm using the energy and fluence of 200 keV and 1×10^{14} ions/cm^2, respectively. The obtained ion segments are much

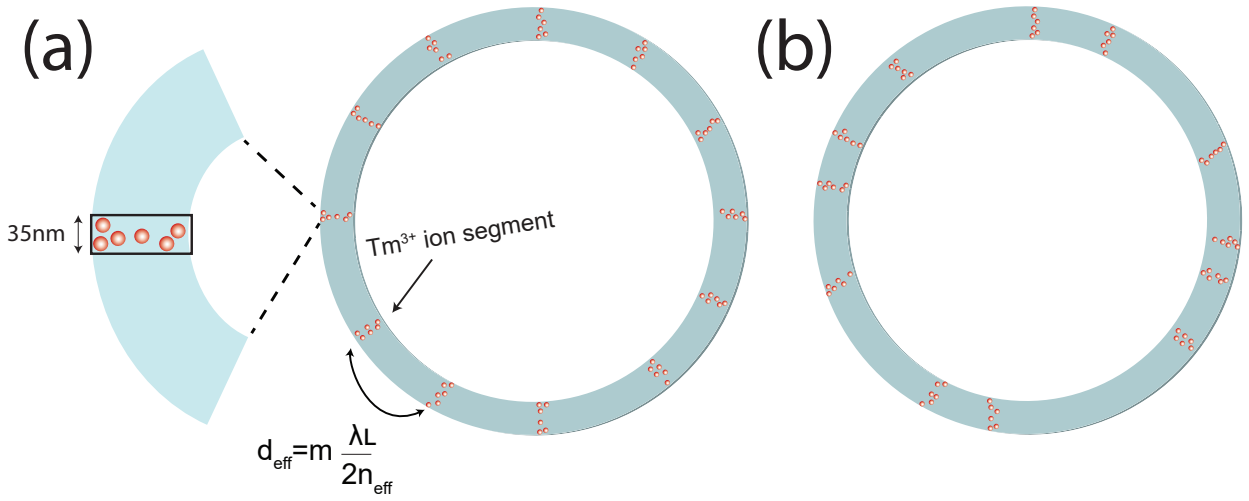

Figure 4.2. (a) schematic diagram of a ring resonator implanted with periodic ion segments. Each ion segment is separated by close to $\lambda_L/2n_{eff}$. Each ion segment is defined by a 35nm × 600nm rectangular implantation mask; (b) schematic of a ring resonator implanted with disordered ion segments for comparison. In both cases, the ions are randomly implanted within each segment. Material from: 'Pak, D. *et al.*, Long-range cooperative resonances in rare-earth ion arrays inside photonic resonators, Commun Phys **5**, 89 (2022), Springer Nature'.

smaller than the optical wavelength (∼0.8 µm), enabling a point-like approximation of each segment of ions. After the implantation process, post-implantation annealing is performed at 500°C for 8 hours under a Nitrogen atmosphere to repair crystal damage caused by the implantation. After the annealing procedure, Tm ions bond with the crystalline matrix and they change such that only Tm^{3+} ions with the optical transition of interest can create stable bonds.

4.4 LN Photonic micro-ring resonators integrated with Tm^{3+}

Figure 4.4(a) shows the schematic figure of the fabricated micro-ring resonator with the Tm^{3+} arrays. Each ion segment is a rectangular box within which about $N_s = 2.2 \times 10^4$ ions are randomly implanted. A collection of $M_s = 1750$ segments create an array with fixed segment spacing (ordered array) or random spacing (disordered array). To couple light into the micro-ring cavity via the bus waveguide, the LN layer was fully etched on the edges of

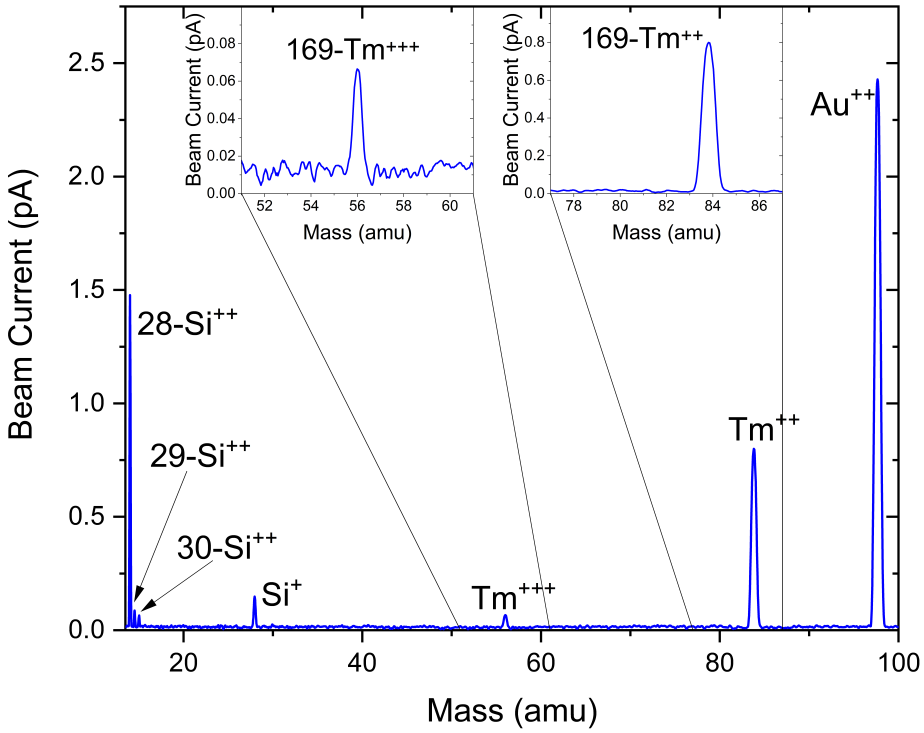

Figure 4.3. An AuSiTm mass spectrum, showing a clear signal from the implanted Tm^{2+} ions. Material from: 'Pak, D. *et al.*, Long-range cooperative resonances in rare-earth ion arrays inside photonic resonators, Commun Phys **5**, 89 (2022), Springer Nature'.

the wafer to allow fiber-to-chip coupling. An additional input waveguide port (drop-port) designed on the other side of the micro-ring enables coupling of light to the micro-ring from the opposite side.

After the ions are excited using a pump injected from the drop-port, the scattered light in the clockwise and counter-clockwise directions inside the micro-ring can interfere to create a standing wave [107]. When the array is regularly spaced with spacing close to $\lambda_L/2n_{eff}$, where n_{eff} (= 2.159) is the effective refractive index of the cavity mode (in this case TE mode) and λ_L is the wavelength where the light is commensurate with the atomic lattice, ions can experience the electric field from the other ions in the array with the same phase. In the commensurate lattice (CL) condition, the peak intensity of the standing wave perfectly coincides with the location of the ions in the arrays. Ideally, in this case, all the ions can coherently and cooperatively emit light even though the extent of the array is much larger

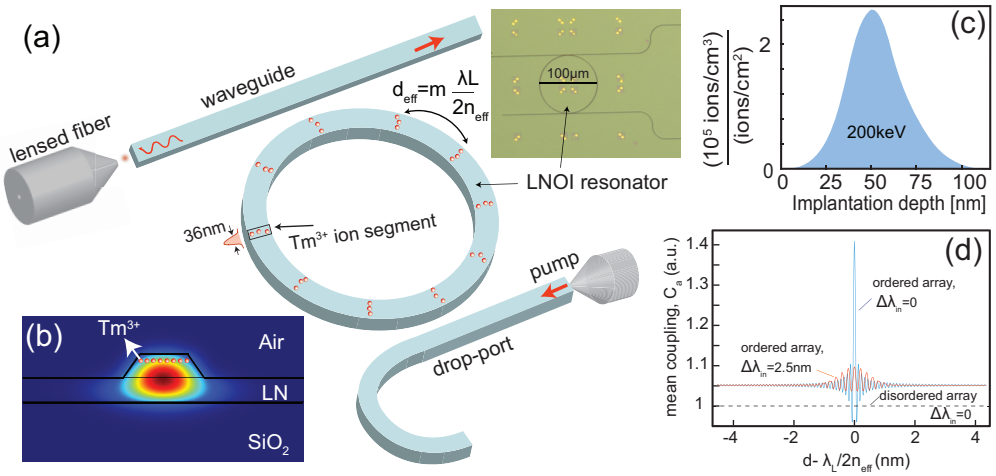

Figure 4.4. (a) Schematics of an LN micro-ring resonator incorporated with Tm^{3+} ion arrays engineered to have spacing close to $\lambda_L/2n_{eff}$. The top-right inset is an optical microscope image showing the fabricated LN micro-ring resonator with Au alignment marks used for implantation; (b) Comsol simulation showing the fundamental TE mode confinement in the half-etched LN waveguide with the implanted Tm^{3+} ions. The width of the waveguide is 600 nm; (c) SRIM-software simulation showing the distribution of the implanted Tm ions in the LN layer. When implanted with 200 keV energy, the peak ion distribution lies around 51 nm below the top LN surface with a Gaussian distribution width of around 16 nm. The peak of the ion distribution corresponds to 0.1% ion concentration; (d) Mean atom-atom coupling rate (C_a) of an ordered array normalized to that of a disordered array. $\Delta\lambda_{in}$ represents the width of the inhomogenous broadening of ions. Material from: 'Pak, D. *et al.*, Long-range cooperative resonances in rare-earth ion arrays inside photonic resonators, Commun Phys **5**, 89 (2022), Springer Nature'.

than the light's wavelength ($\sim$ 0.8μm). Figure 4.4(b) shows the finite-element calculation of the E-field in the cross-section of the micro-ring. The etched sidewall angle of LN thin-film is 55° and the fundamental TE mode is well confined inside the partially-etched waveguide. As it is confirmed by the SRIM simulation (Figure 4.4(c)), the peak of ion concentration is around 51 nm below the top LN surface with a Gaussian distribution width of around 16 nm. Figure. 4.5 describes the electric field distribution in the LN waveguide. When taking into account the Gaussian distribution width ($\sim$16 nm), the E-field amplitude at the position of ions, $\frac{E(ions)}{E_{max}}$, is 0.437 $\pm$ 0.07.

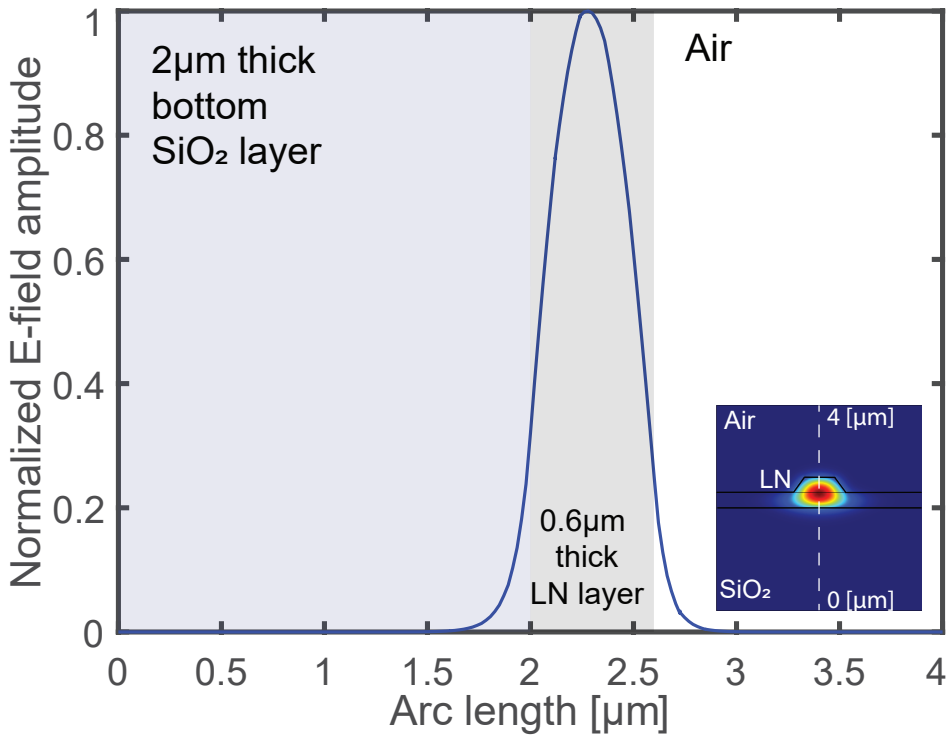

Figure 4.5. Normalized E-field distribution in the LN waveguide. Material from: 'Pak, D. *et al.*, Long-range cooperative resonances in rare-earth ion arrays inside photonic resonators, Commun Phys **5**, 89 (2022), Springer Nature'.

To see how the cooperative coupling changes with the lattice spacing, we define a mean atom-atom coupling (See 4.2) as

$$C_a = \sqrt{\int\int \mathcal{N}^2(\theta,\omega)\sin^2(kR\theta)d\theta d\omega} \tag{4.23}$$

where $\mathcal{N}(\theta,\omega)$ describes the angular distribution of atoms and inhomogeneous broadening of transition frequencies both described by Gaussian distributions, and R is the ring radius. Fig. 4.4(d) shows the calculated value of C_a normalized to that of a disordered array. The enhanced atom-atom coupling is seen for ordered arrays in both the commensurate ($d = \lambda_L/2n_{eff}$) and the incommensurate ($d \neq \lambda_L/2n_{eff}$) conditions. The effect of inhomogeneous broadening of width $\Delta\lambda_{in}$ can be seen as broadening of C_a envelope. In our case, the periodic ion array is not exactly commensurate with the optical wavelength.

4.5 Cavity-induced Purcell enhancement of Tm at cryogenic temperatures

After the fabrication and implantation processes, we characterize the optical properties of the micro-ring and ions. We first measure the effect of micro-ring enhancing emission from the ions. The quality factor (Q) of the micro-ring resonator was measured to be about 2.2×10^4 at 796.85 nm, as shown in Figure 4.7(a). To measure the photoluminescence (PL) lifetime of Tm^{3+} ions in the micro-ring resonator, a pump light around 795 nm was pulsed (2 ms) and injected into the micro-ring from the drop-port. The second AOM is used to further reduce the noise from the pump.

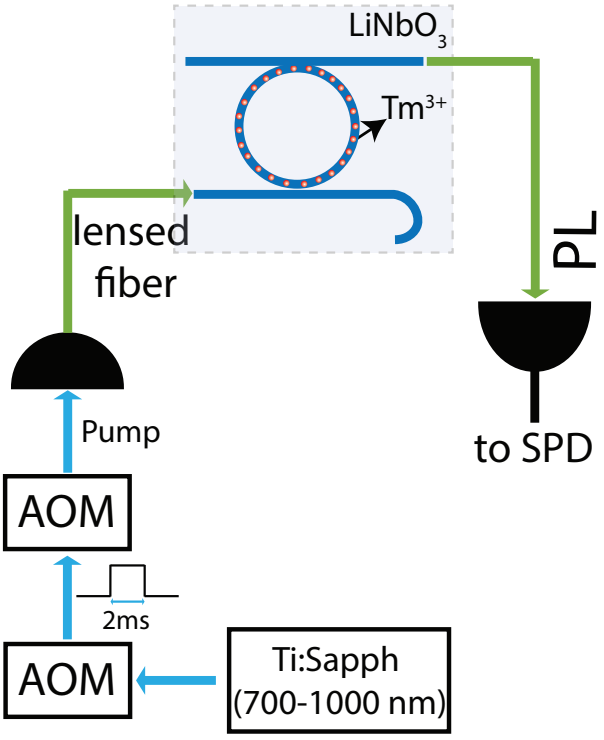

Figure 4.6. (a) Schematic diagram of the experimental setup to measure the PL lifetime of Tm ions.

Because of the geometry of the designed drop-port, most of the pump light exiting the micro-ring is guided to one side of the bus waveguide. By positioning a lensed fiber on the other side of the waveguide, we can effectively screen the pump light while measuring the PL signal from Tm^{3+} ions. The emitted PL signal is then detected using a single-photon detector (Fig. 4.6).

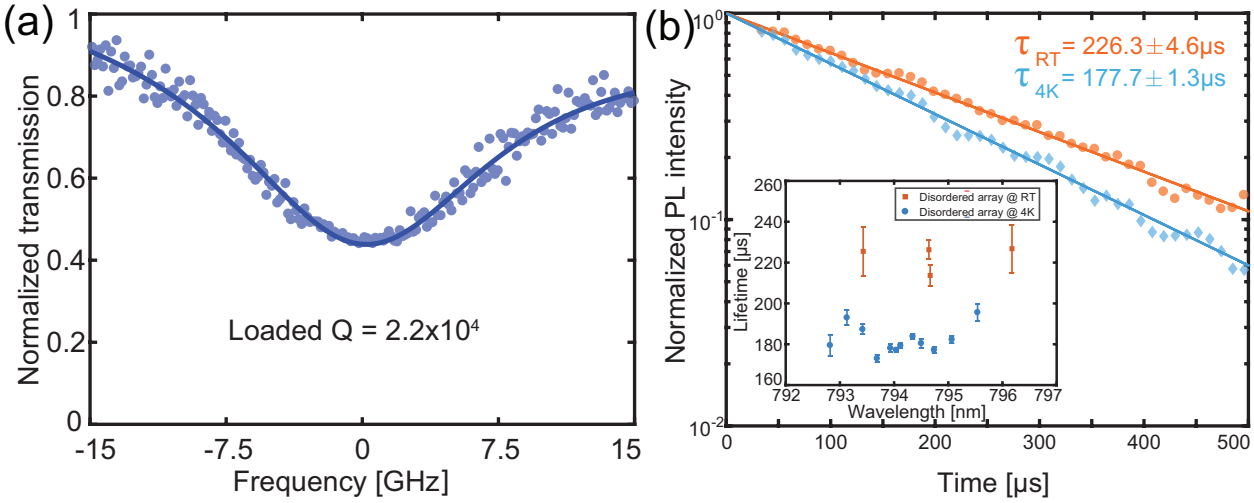

Figure 4.7. (a) The transmission signal at 796.85 nm showing the micro-ring cavity resonance and the corresponding Lorentzian fit (with asymmetry described by a linear parameter) with a loaded quality factor of 2.2×10^4. (b) Two PL decay curves of Tm^{3+} ions measured at room temperature (red) and 4K (blue) from the LN micro-ring resonator of the disordered array, both pumped at 795nm, are shown. The fitted lifetime of RT and 4 K PL curves are 226.3 μs and 177.7 μs, respectively. The inset shows PL lifetime at both RT (red) and 4 K (blue) as a function of the resonant pump wavelength. Error bars defined here represent 95% confidence interval. Material from: 'Pak, D. *et al.*, Long-range cooperative resonances in rare-earth ion arrays inside photonic resonators, Commun Phys **5**, 89 (2022), Springer Nature'.

To study the effect of the cavity on light emission, a micro-ring with randomly spaced ion segments (with no periodic array structure) is used for PL measurement at both room temperature (RT) and 4 K. The temperature dependency of PL decay in presence of multidimensional decay processes [29], [30] provides means to measure the Purcell factor of ion emission by comparing decay rates at cryogenic and room temperatures in the same device. For rare-earth ions at room temperature, the ions' homogeneous linewidth is much greater than the cavity linewidth that suppresses the Purcell effect [30], [32]. At cryogenic temperatures, the homogeneous linewidth or the dephasing rate is expected to significantly decrease and be narrower than the cavity decay rate, where the Purcell factor can be fully recovered (for more detailed explanation about the temperature-dependent Purcell effect, please refer to the section where the Purcell effect is explained in detail (Eqn. 1.4)). Figure 4.7(b) shows the normalized PL intensity of Tm^{3+} ions pumped on the cavity resonance near the atomic

transition (λ_{pump} = 794.5 nm) for both RT and 4 K. The lifetime of Tm^{3+} ions at 4 K is reduced compared to the PL lifetime at the elevated temperatures. The inset of Fig. 4.7(b) shows the PL lifetime as a function of the pump wavelength for both RT and 4 K. The data confirm the lifetime shortening at 4K compared to RT emission. We attribute this lifetime shortening at 4K to the Purcell enhancement provided by the micro-ring. Theoretically, the maximum Purcell factor can be calculated by the equation 4.24, taking into the account the spatial overlap of the ions' position.

$$F_p = \frac{3}{4\pi^2}(\frac{\lambda}{n_{eff}})^3(\frac{Q}{V_{mode}})(|\frac{E(Tm)}{E(peak)}|)^2 \tag{4.24}$$

where $V_{mode} = \frac{\int dV\epsilon(r)|E(r)|^2}{max(\epsilon(r)|E(r)|^2)}$ is the mode volume of the ring resonator, $\frac{E(Tm)}{E(peak)}$ is the relative amplitude of the E-field at the ions' location. Here, the mode volume is $\sim 64.9\mu m^3$ and $\frac{E(Tm)}{E(peak)}$ is $\sim$0.437, calculated using COMSOL. Considering our parameters, the theoretical maximum Purcell factor (assuming a branching ratio of unity) becomes about 0.25.

Also, the experimental Purcell factor is calculated by τ_{RT}/τ_{4K}-1 $\approx 0.27 \pm 0.1$. The theoretical maximum Purcell factor is very close to the measured value. In the case of Tm ions in a LN crystal, the branching ratio of Tm ions for $^3H_4$ - $^3H_6$ transition is 0.73 (Fig. 4.8) [108], [109]. In our care, because we use isotopically pure Tm ions, the transition probability for relaxation to $^3H_6$ in $LiNbO_3$ can be even higher. For this reason, we use the maximum theoretical Purcell factor (assuming a branching ratio of unity) for comparison to the experimental results.

Based on our previous studies [50], we expect a negligible non-radiative decay at room temperatures. In the case of REIs doped in crystalline hosts such as LN, the nonradiative decay by the phonon decay processes is the dominant nonradiatve decay mechanism [110], [111]. Based on the recent study also performed in a Tm:LNOI sample [69], the nonradiative decay of Tm ions in LNOI waveguide is negligible compared to the bulk LN sample. Given that the measured PL lifetime in our implanted sample (at both room temperature and 4K) is longer than the Tm-doped LNOI [69], [108], we conclude that nonradiative decay is negligible in our system. Otherwise, the experimental Purcell enhancement factor obtained

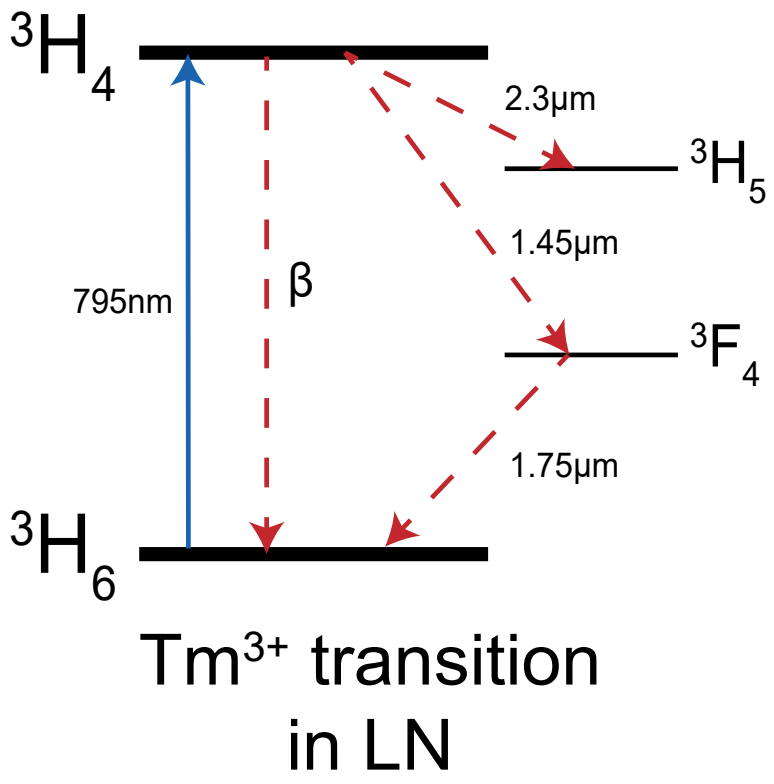

Figure 4.8. A schematic figure of the simplified Tm^{3+} transition in LN. Material from: 'Pak, D. *et al.*, Long-range cooperative resonances in rare-earth ion arrays inside photonic resonators, Commun Phys **5**, 89 (2022), Springer Nature'.

above is an underestimation. The Purcell enhancement is a single-body effect provided by the mode confinement in the cavity. Below we discuss the results of cooperative emission as a collective effect resulting in an additional enhancement of light emission from an ordered ion array.

4.6 Array-induced enhanced light scattering

To verify the effect of the array on emission, we fabricated two identical micro-ring resonators with an identical number of ion segments. In one case, ion segments were randomly distributed along the micro-ring (also used for data in Figure 4.7), while the other micro-ring hosts an ordered ion array (with loaded Q= 1.8×10^4).

In order to measure the scattering/reflection signals from the ions in the ring resonator, the light around 790 nm is continuously pumped from the Ti:Sapphire laser (M Squared SolsTis) with the power of 7.5W. The pump laser is then divided into 2 light paths by a beam sampler (BS) with a ratio of 9 to 1. The main pump path which contains most of the power (90%), denoted as P1, is then connected to a fiber coupler. The lensed fiber is then connected to the drop-port of the ring-resonator. As described in the main text, because of the designed geometry, most of the input light after coupling to the ring is guided to one direction of the bus waveguide. By placing a lensed fiber on the other side of the bus waveguide, we can measure the scattering/reflection signal effectively. The output signal is then connected to a Femto-watt detector (For PL measurement, the output is connected to a single photon detector), and the output signal is normalized by the other input path (10% power), denoted as P2. The schematic diagram of the measurement setup is plotted in Fig. 4.9.

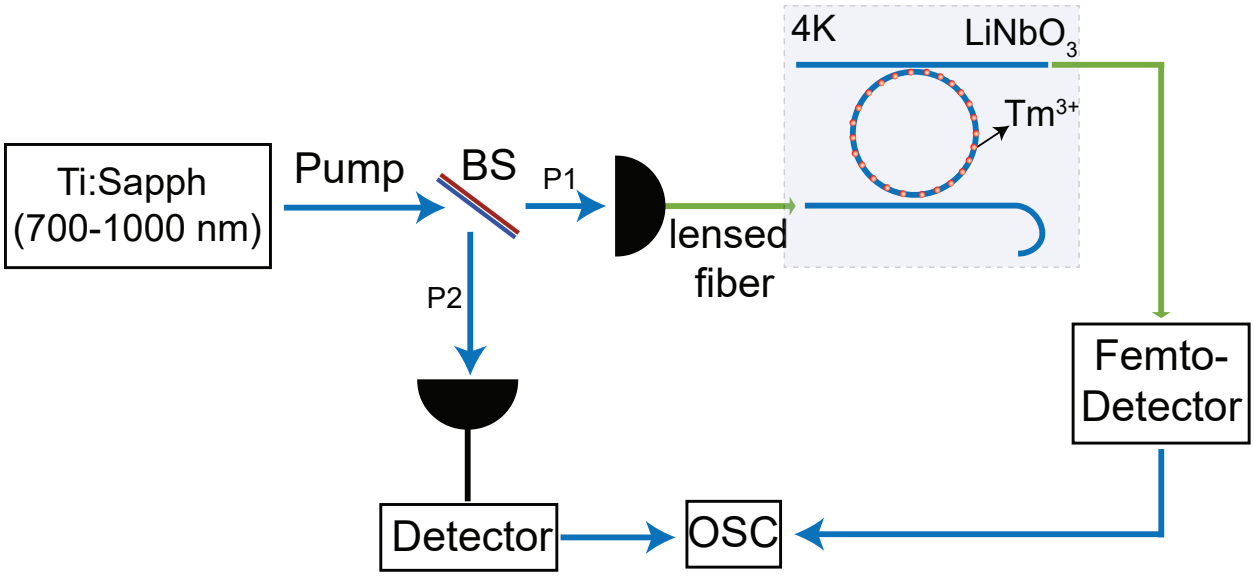

Figure 4.9. A schematic figure of the measurement setup for the scattering/reflection experiments. Material from: 'Pak, D. *et al.*, Long-range cooperative resonances in rare-earth ion arrays inside photonic resonators, Commun Phys **5**, 89 (2022), Springer Nature'.

Figure 4.10(a) shows the resulting normalized scattering signals for both the periodic array and the randomly distributed ensemble. On the atomic resonance condition, the

periodic array shows about 60% more scattering compared to the disordered array. The scattering spectrum from the disordered array matches the absorption spectrum of Tm ions in LN waveguides [69], [97] with splitting due to ^{6}Li and ^{7}Li. The ordered array, however, shows peculiar oscillations originating from two distinct processes, as explained below.

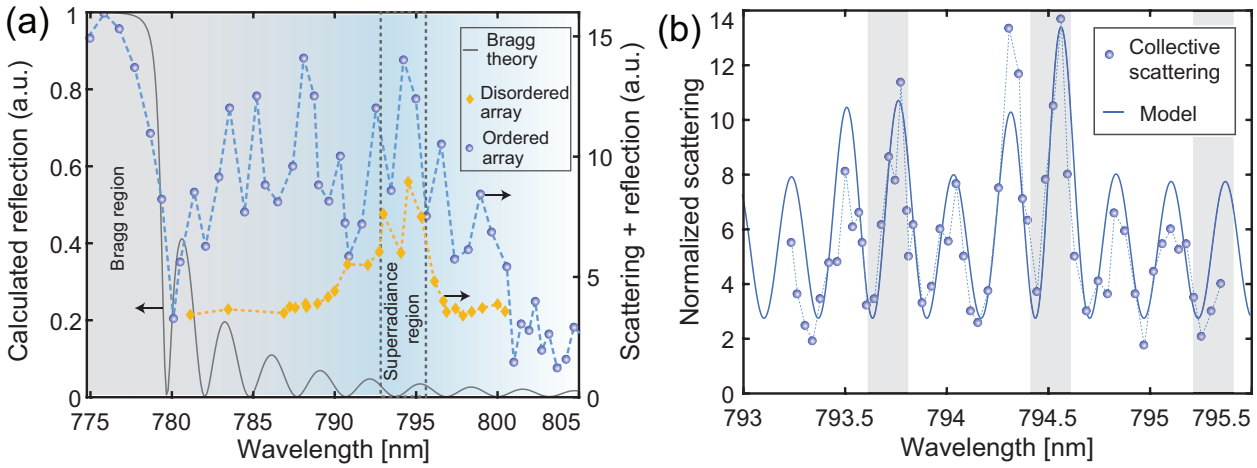

Figure 4.10. (a) Normalized scattering data for the ordered ion arrays (blue) and disordered (randomly distributed) arrays (yellow) as a function of resonant pump wavelength. The scattering from the array near the atomic resonance (∼795 nm) shows an enhancement of about 60% for the ordered array compared to the disordered one. The gray curve shows the calculated Bragg resonance that results from the ion implantation process (see text); (b) A zoomed-in scattering data near-atomic resonance shows modulation of the scattering signal with a period of λ/M_s, where $M_s = 1750$ is the number of ion segments in the array. The periodic oscillation is in agreement with the model of sinusoidal oscillation (solid line) with a double-peak Gaussian envelope of center and width corresponding to that of the disordered array (total width) data in Fig. 3(a). The shaded regions indicate the predicted cavity resonances based on measurement of the cavity spectrum obtained from a different experiment run while taking into the account the uncertainty due to the drift in the cavity resonances. The dashed lines in both plots are guide to the eye. Material from: 'Pak, D. *et al.*, Long-range cooperative resonances in rare-earth ion arrays inside photonic resonators, Commun Phys **5**, 89 (2022), Springer Nature'.

Below 785 nm the signal and its oscillation are dominated by the Bragg scattering induced by the implantation process. Regardless of the ion's optical transition, the process of ion implantation can damage the crystalline matrix inducing a slight change in the refractive index. Some of these damages can be recovered by the annealing process. But as high-

temperature annealing is not an option (due to different thermal expansion coefficients of LNOI layers) [75], a non-negligible index change near the implantation regions may remain. The modulation of the refractive index caused by the periodic implantation of ions can then manifest itself as Bragg-induced back-reflection of the pump light. This is why the reflection signal (originated from the ring) spans beyond the Tm emission band. We expect the signals from both Bragg and superradiance to show the same periodicity. As the result, the signals add up in the wavelength region of 785-790nm while around 775nm and 795nm the Bragg and superradiance effects can primarily be observed, respectively. We note that in Fig. 4.10(a), the fast oscillation with the periodicity of λ_L/M_s is not observed due to the low sampling of the pump wavelength.

Between 790-797 nm, which is the absorption window of Tm^{3+} ions, the effect of Bragg back-scattering is negligible compared to the collective scattering from the array. By fine scanning the pump wavelength near-atomic resonance (see Figure 4.10.(b)), the scattered light intensity shows clear oscillations with a periodicity of λ_L/M_s, where M_s is the number of ion segments. The oscillation of the scattering signal is one signature of the cooperative resonance [94] from the ion array. The theory used to model the oscillation in Fig. 4.10(b) is given by a modulated double-Gaussian profile centered around Tm transitions ($\lambda_{1,2}$) described by $(Ae^{-(\lambda-\lambda_1)^2/(2\Delta\lambda_{in}^2)} + Be^{-(\lambda-\lambda_2)^2/(2\Delta\lambda_{in}^2)})\sin^2(\frac{2\pi}{\lambda_L}M_s\lambda + \theta_0)$, where $\lambda_L/2$ is the lattice spacing, $\Delta\lambda_{in}$ is the width of the inhomogeneous broadening of ions extracted from Fig. 4.10(a) and A, B and θ_0 are free parameters.

As the free-spectral range of the cavity is about 0.8nm, the majority of points measured in Fig. 4.10 were obtained where the pump was off the cavity resonances (shaded regions in Fig. 4.10(b)). The drop-port coupling is only ∼5% and the effect of the cavity resonances is expected to be small compared to the size of the oscillations observed in Fig. 4.10.

To verify that the near-resonance scattering signal is originated from the cooperative effect of ions, we also measure the emission lifetime of Tm ions for both ordered and disordered arrays at 4K (Figure 4.11(a) and (b)). Compared with the disordered array that does not exhibit a noticeable change in the lifetime near the Tm optical transitions, the ordered array shows reduced lifetime at $^3H_4 \rightarrow {}^3H_6$ transitions (with splitting from ^{6,7}Li centered around 793.5 nm and 794.5 nm). The maximum lifetime change is $\tau_2/\tau_1 \simeq 1.25$, which is expected

to scale linearly with effective number of excitations, contributing to the cooperative emission. The data in Fig. 4.11(b) also show a minor trend as a function of pump wavelength. Near the cavity resonances shown as shaded regions, the enhanced Purcell factor is expected, which explains the lifetime reduction near 793.5 nm and 795 nm. It can be seen that near the atomic resonant frequencies, i.e. 794.5nm and 793.5nm, the lifetime is slightly higher. This can be explained by light re-absorption or radiation trapping [112] also observed in our previous studies [45], [50].

We observe that the quality of the LN sample degrades over time whose effect is to reduce the efficiency of fiber-to-chip coupling. This results in lowering the signal-to-noise ratio for some data points taken later (Fig. 4.11(a)) compared to earlier data (Fig. 4.11(b)). We believe this is because of the undercutting (etching) of the bus waveguide edge near the U-grooves (Fig. 4.12) that breaks up over time after few thermal cycling processes.

Figure 4.11(c) shows the result of decay time measurement as a function of pump power. As the pump power changes the fraction of ions excited, the lifetime linearly changes with the pump power below the saturation regime [105]. We discuss these results in more detail below.

4.7 Discussion

When emitters are confined to a region much smaller than the wavelength, directional and enhanced emission is expected that is accompanied by the lifetime modification [113]. Apart from the high atomic densities, low coherence time and small inhomogeneous broadening are required to reach this superradiance regime. In this regime, coherent emission can occur where atoms collectively emit photons with the same phase. As a result, the spontaneous emission rate is modified by the collective enhancement factor, η, which linearly scales with the number of collective excitations. Moreover, the total photon number directionally emitted in the detection is expected to scale quadratically with the number of collective excitations. This is accompanied by a reduction in the free-space scattering.

In the case of rare-earth ions, high-density implantation gives rise to increased decoherence due to the dipole-dipole dephasing that suppresses the superradiant scattering from

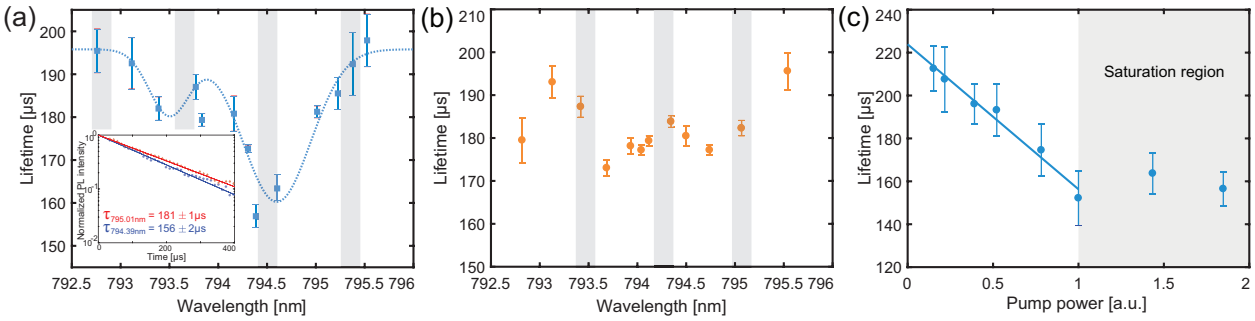

Figure 4.11. (a) PL lifetimes of the Tm^{3+} ions as a function of wavelength in the periodic array, indicating the lifetime shortening near the atomic resonance as a result of cooperative resonances. The solid curve is a fit using a double-Lorentzian function with center wavelengths and widths matching that of scattering profile from the disordered array (Fig. 4.10(a)). The inset shows two PL decay curves of the Tm^{3+} ions: one away from the atomic resonance (red), the other close with the resonance (blue); (b) PL lifetimes of the Tm^{3+} ions as a function of wavelength in the sample with disordered ion array, showing the lifetime is mainly unchanged near the atomic resonance; We note that the slight difference in quality factors of rings used in (a) and (b) causes small differences in Purcell-enhanced emission in the two cases and therefore the off-resonant lifetimes are not exactly the same. The shaded regions indicate the predicted cavity resonances based on measurement of the cavity spectrum obtained from a different experiment run while taking into the account the uncertainly due to the drift in the cavity resonances; (c) PL lifetimes of the Tm^{3+} ions as a function of input resonant pump power in the periodic array at a fixed wavelength of 794.4 nm. The lifetime linearly changes with the pump power that is a proxy for ion numbers in the array. Above some critical power, the lifetime remains unchanged as the pump saturates the ions. The y-intercept of the linear fit is ∼224 μs. The lifetime data in Fig. 4(a) and (b) are taken with the pump power in the saturation region of Fig. 4(c). Error bars defined here represent 95% confidence interval. Material from: 'Pak, D. *et al.*, Long-range cooperative resonances in rare-earth ion arrays inside photonic resonators, Commun Phys **5**, 89 (2022), Springer Nature'.

local ensembles. Instead, an array of local ensembles commensurate with the oscillation of the intra-cavity E-field collectively behaves as a high-density ensemble enabling observation of superradiance in the extended ensemble, or "long-range superradiance". Due to the distribution of ion frequencies (i.e. inhomogeneous broadening), more ions are at the center of the absorption/emission spectrum. Therefore, at the center of the atomic resonance the highest collective effect is expected.

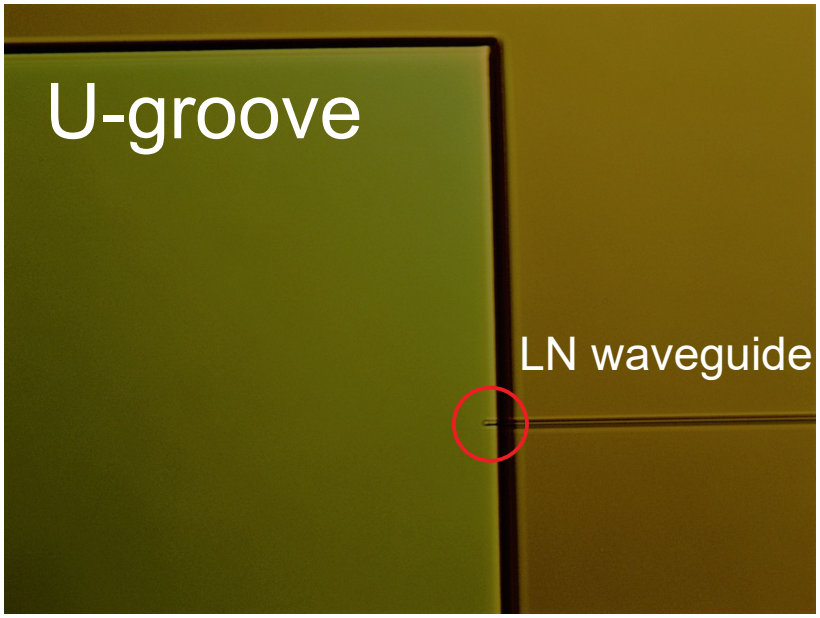

Figure 4.12. Optical microscope image showing an LN waveguide and a U-groove. Because of the non-ideal alignment between U-grooves and waveguides, the LN waveguide is sticking out to the U-groove side by $\sim 5\mu$m. This part breaks up during the thermal cycling process, causing the drop in the fiber-to-chip coupling efficiency over time. Material from: 'Pak, D. *et al.*, Long-range cooperative resonances in rare-earth ion arrays inside photonic resonators, Commun Phys **5**, 89 (2022), Springer Nature'.

The lifetime shortening can occur due to both the cavity confinement and the collective effect. When the pump is off-resonant from the cavity resonance but still within the ions' absorption spectrum, the pump can still be coupled to the cavity and the lifetime shortening due to the collective effect can be observed. When the pump is on both atomic and cavity resonances, both cavity and collective effects contribute to the lifetime shortening. In the absence of the cavity, the interaction drops as $1/d^3$, for d being the atom spacing, while the micro-ring cavity leads to a semi-infinite-range (all-to-all) interactions between the emitters. This happens because all emitters efficiently couple to the same mode in a specific direction rather than a coupling via a free-space photon randomly emitted in all directions.

In the presence of the inhomogeneous broadening, mesoscopic cooperative decay of the symmetric and time-Dicke states [102], [113], [114] can be observed as a simultaneous presence of sub and superradiant modes when all atoms are excited [115]. In our experiment,

the signal-to-noise ratio is not high enough to confirm the slow decay signature of subradiant states after the initial fast decay. Also in arrays, excitation of subradiant states can be harder than the superradiant ones [102]–[104] due to the complicated long-range interactions and many-body features of the atomic ensembles. Both inversion and pump-induced correlations between the atoms play a role in driving superradiant states [105]. At low pump powers, the interaction energy prevents efficient population of subradiant states. Uniform directional pumping along the cavity axis, gives rise to correlations that increase with duration or power of the pump light. Below saturation, we therefore take the pump power to be a proxy for η. In Figure 4.11(c) we vary the pump power and measure the decay time. The results show that below saturation, the emission lifetime linearly decreases with the pump power. The data provide early evidence of cooperative effects of arrays in solids and further investigation is needed to understand the complicated decay dynamics and the transition from sub- to super-radiance regime.

To theoretically describe the collective effects inside the cavity, we use the effective spin model [98] and write an effective Rabi frequency for the nth ion segment in the array as $\Omega_n = \Omega_0^{(n)} + 3\pi\Gamma_0 \sum_{m\neq n} G_{mn}\langle\hat{\sigma}_{\mathrm{ge}}^{(m)}\rangle$, where $\Omega_0^{(n)}$ is the Rabi frequency of the pump in the cavity at the ion segment n, $\hat{\sigma}_{\mathrm{ge}}^{(m)}$ is coherence between ground and excited states of atomic segment m, G_{mn} is the Green's function of the mth ion at nth ion location, and Γ_0 is the ion natural decay rate. The second term describes the scattering from all other segments that modify the local field of the nth segment, leading to an effective dipole-dipole interaction. The Green's function of the ring can be determined as $G_{mn} = \mathrm{i}\,\frac{2}{3}\,\frac{g_0^2}{c_p\Gamma_0}\,\exp(\mathrm{i}kR|\theta_n - \theta_m|)$, where g_0 is the single-atom vacuum Rabi frequency, c_p is the mode phase velocity, R is the ring radius, and θ_{i} is the angular position of ion segment i. This clearly shows the role of the ring in creating an all-to-all infinite-range spin interactions (See 4.2 for a detailed discussion).

In the limit of the non-depleted ion, i.e. $\sigma_{\mathrm{ee}} \approx 0$, we can determine the steady-state coherence of the order-array equations of motion to arrive at $\langle\sigma_{ge}\rangle = -\mathrm{i}g_0\sqrt{2\pi}E_o/(-\mathrm{i}\delta + \Gamma_0/2 + \frac{2\pi g_0^2}{\kappa}\eta)$. Here, κ is the cavity decay rate and the last term in the denominator is the effective coupling rate enhanced by η, the collective enhancement factor. The ratio of the scattering rate into the cavity mode compared to free space can then be calculated as

$\gamma_2/\gamma_1 = 1 + \frac{4\pi g_0^2}{\kappa\Gamma_0}\eta$, having the signatures of both cavity-enhanced emission via a Purcell effect and the cooperative array effect.

Comparing the lifetimes of the Purcell-enhanced disordered array (Fig. 4.7(b)) and array-enhanced emission (Fig. 4.11(a)), we can estimate an experimental value for the effective number of collective enhancement factor $\eta \simeq 1.8$. In absence of imperfections such as inhomogeneous broadening, the enhancement factor is equal to the number of collective excitations. In our case, the enhancement factor quantifies the average effect of cooperative emission. The measured value of $\eta > 1$ suggests that at least two ions cooperatively emit. To identify the exact number of ions collectively emitting into the detection mode, one needs to measure lifetime for varying implantation density or segment number and perform numerical calculation in a multi-dimensional space [83]. The result can be improved by operating in the commensurate condition and enhancing the atom number and coherence time by, for example, novel multi-step implantation and annealing techniques [116] and further operating at lower temperatures and higher magnetic fields [97]. Considering an enhancement of the coherence time at lower temperatures and higher magnetic fields by two orders of magnitude (as evidenced in Ref. [97]) and increasing the cavity Q to about one million (experimentally within reach [28], [42], [67], [68]), a substantial increase in cooperative effects can be observed where $\eta > 100$ can be realized.

4.8 Conclusion

To the best of our knowledge, this is the first time the long-range cooperative resonance has been achieved in any solid-state photonic platform. The enhanced directional emission can reduce the noise (spontaneous free-space decay) when the system is used for quantum light storage. Moreover, the collective optical-density increase due to all-to-all infinite-range coupling leads to enhanced absorption albeit with low densities avoiding density-associated dephasing. Despite the large inhomogeneous broadening of ions in solids compared to the laser trapped atomic arrays [117], [118], the deterministic ion localization, and significantly larger ion numbers and array lengths make it easier to study many-body and cooperative phenomena. Ideally, in the regime of strong atom-atom interactions dark states [95], [119],

[120] and blockade effects [121] may emerge leading to a peculiar regime of light-atom interactions on-chip.

5. SUMMARY AND FUTURE WORK

5.1 Summary

In summary, this dissertation explores 1) the fabrication process of long waveguides and ring resonators in thin-film SiN, LN and 2) optical characterizations of Yb^{3+} ions at room and cryogenic temperatures in the micro SiN and LN structures, and 3) cooperative resonances of Tm^{3+} ion arrays inside LN micro-ring resonators.

In chapter 2, the fabrication process of the long waveguide and ring resonator in SiN, showing the vertical sidewall angle, is introduced. Yb^{3+} ions are implanted into the SiN waveguides and then, the lifetimes of Yb^{3+} ions in the waveguide and the resonator were independently measured at 4K. The lifetime in the ring resonator is slightly reduced by the cavity. However, because of the low Q-factor of the resonator, the Purcell effect was not obvious. Also, impedance-matched condition modified by atoms is also studied by probing the cavity intrinsic quality factor and relative contrast of the cavity as a function of wavelength.

In chapter 3, the fabrication techniques to fully etch thin-film LN waveguides using ICP-RIE are investigated. Because LN is a hard-to-etch material and easily re-deposited onto the surface, the optimized etching recipe is highly required. I have successfully etched LN and achieved clean and smooth LN waveguides. Similarly, Yb^{3+} ions are implanted into the LN waveguides and the loaded quality factor reaches about 2×10^5 and the corresponding intrinsic quality factor reaches about 2×10^6 after annealing. The photoluminescence spectrum of Yb^{3+} ions is measured and Purcell enhancement of the PL decay of Yb^{3+} ions are observed when resonantly pumped, which implies the cavity increased light-atom interactions. Furthermore, more PL counts were detected when the pump is resonant with the cavity because of increased intra-cavity pump power on resonance. Finally, atomic absorption effects probed by the cavity intrinsic quality factor and relative contrast of the cavity as a function of wavelength are observed. I study the condition of impedance-matched cavities and the role of atoms in designing impedance-matched cavities.

In chapter 4, I partially etched LN thin-film and implanted Yb^{3+} ions with a fixed spacing close to $\lambda_L/2n_{eff}$ to form periodic ion arrays. For comparison, I fabricated 2 rings with the exact same parameter: one for periodic arrays and the other for randomly distributed

segments. The cavity-induced Purcell enhancement is observed when the PL decay of Tm^{3+} ions are measured in the randomly distributed sample. I also observed that the scattering signal from periodic arrays is oscillating with a periodicity of λ_L/M_s. We believe this is one sign of the cooperative resonance from ion arrays. Furthermore, the PL decay of Tm^{3+} ions showed further enhancement near the atomic resonance in periodic arrays driven by the cooperative array effect, giving the signatures of both Purcell effect and cooperative effect.

5.2 Future Work

One of the future works includes improving the quality factor of the LN ring resonator. In chapter 3, we reported the Q factor of 2×10^5 at 0.9μm, and in chapter 4, we reported the Q factor of 2×10^4 at 0.8μm. The quality factor of LN micro-ring resonators in chapter 3 was one order of magnitude higher than that of chapter 4. This is because the LN waveguide in chapter 3 was optimized for 1.5μm. Since one of the significant loss channels in the LN waveguide is the sidewall scattering [28], having the wider waveguide width gave the higher Q at the expense of having the multimode in the waveguide.

Also, we observed that the LN ring resonators etched with both physical and chemical etch (the recipe we used - BCl_3, Cl_2, Ar) showed about two orders of magnitude smaller quality factor ($\sim 10^4$) [71] than that of the LN resonators etched only with physical sputtering (Ar) ($\sim 10^6$) measured at a similar wavelength (1.5μm) [28], [68]. As the loss mostly comes from lattice reconstructions at the edge of the etched sidewall of the waveguide and the etching process damages the lattice structure [39], I believe the isotropic nature of chemical etching increases the roughness of the sidewall of the waveguides, resulting in lower quality factors. Therefore, the optimized LN etching recipe only utilizing the physical Ar sputtering can be developed to further increase the quality factor of LN ring resonators.

In the near future, some of the promising research directions based on the results of the Dissertation can be

1) To develop on-chip quantum memories using ion ensembles embedded in photonic devices in the weak coupling regime. One approach to accomplish this application is to

utilize on-chip electrodes to control the light storage process by applying stark shift to the ions. LN is known for having electro-optical properties [7] and REIs have dipoles, therefore applying electric field can introduce Stark shift to the ions [76]. To control light-atom coupling, frequency tuning of ions to the cavity resonance can be utilized [122]. In our case, by linearly changing the gap of the electrodes, making a gradient of the electric field to control the storage process becomes possible. The Fig. 5.1 shows the fabricated waveguides and Au electrodes to apply voltage. The Au electrodes are deposited using the lift-off process.

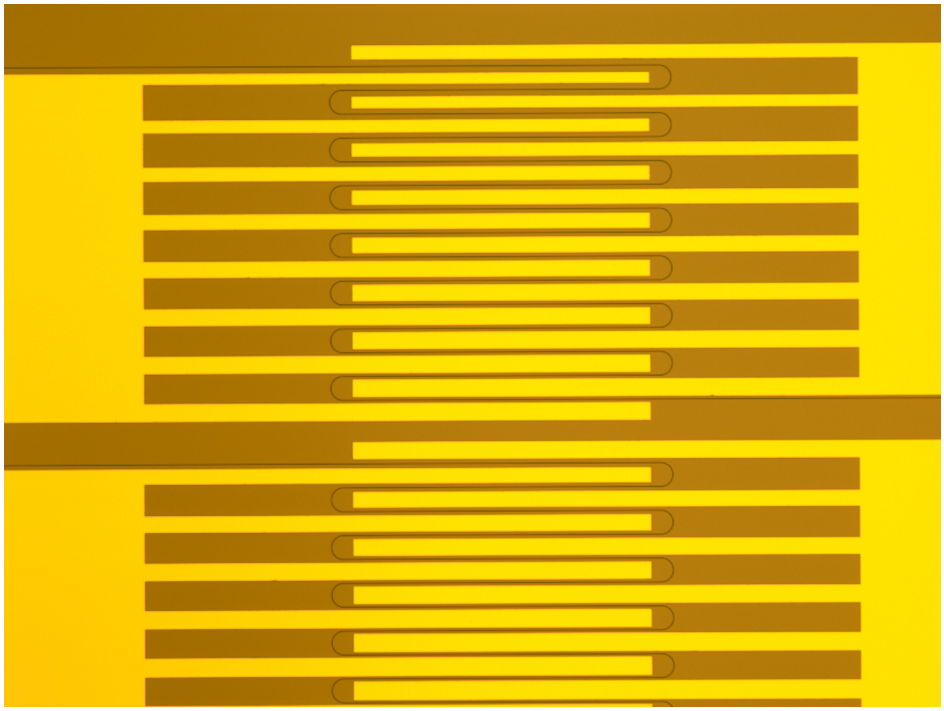

Figure 5.1. The optical microscope image showing the fabricated LN waveguide and Au electrodes for the stark shift experiment

2) To develop on-chip quantum transducers using IDTs (Inter-Digital Transducers) with rare-earth ions on bulk LN wafers. Recently, Yb^{3+} ions have exhibited both microwave and optical coherence [24], which shows the possibility of future applications for microwave to optical transduction [25]. The transduction of microwave to optical signals at cryogenic temperatures is critical for future superconducting quantum computers [26], [123]. Lithium niobate is chosen for this application because LN is known for having piezoelectric properties [7] and LN has been widely used as a host platform for various REIs [42], [68], [69].

In one approach, utliizing on-chip IDTs to control the rare-earth ions has been proposed. By utilizing IDTs and applying a voltage, surface acoustic waves (SAWs) can be created on the surface. When SAWs are present on the chip, we expect only the atoms whose velocity is matching with that of SAWs can stay, and all the other ions whose velocity is not matching with that of SAWs move away from the surface. Therefore, SAWs can be used as an atomic filter and, as a result, can reduce the linewidth of the atoms. As a first step, I fabricated IDTs on the bulk LN wafer. The Fig. 5.2 shows the fabricated IDTs. Similarly, the Au layer is deposited using the lift-off process.

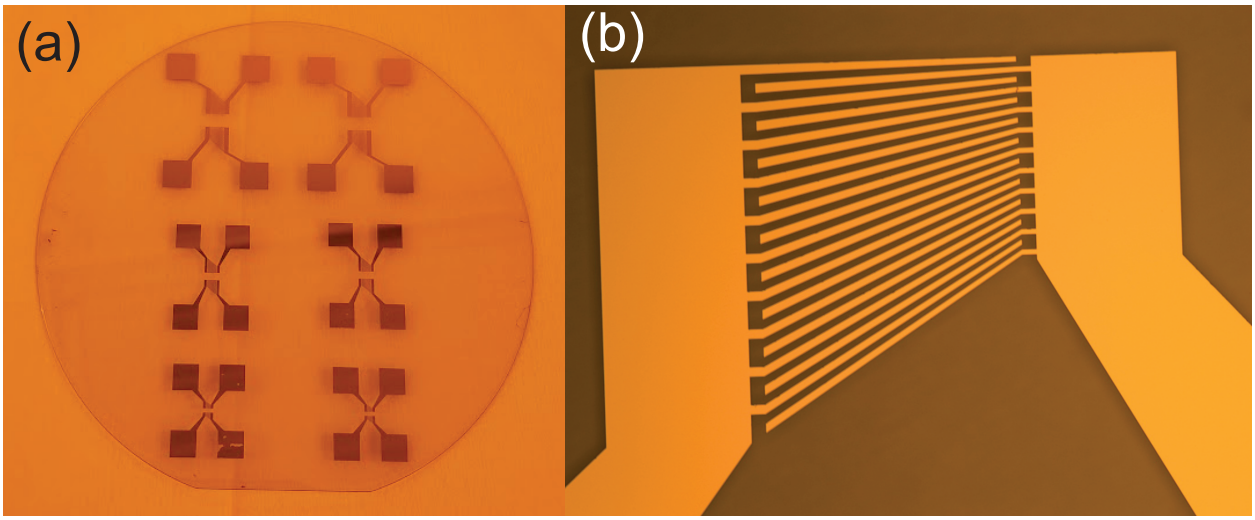

Figure 5.2. (a) Fabricated IDTs on a 4-inch bulk LN wafer; (b) Optical microscope image of the fabricated IDT through the lift-off process

REFERENCES

[1] R. Cone, C. Thiel, Y. Sun, T. Böttger, and R. Macfarlane, "Rare-earth-doped materials with application to optical signal processing, quantum information science, and medical imaging technology," in *Advances in Photonics of Quantum Computing, Memory, and Communication V*, International Society for Optics and Photonics, vol. 8272, 2012, 82720E.

[2] T. J. Kane and R. L. Byer, "Monolithic, unidirectional single-mode nd: Yag ring laser," *Optics letters*, vol. 10, no. 2, pp. 65–67, 1985.

[3] L. Weiss, A. Gritsch, B. Merkel, and A. Reiserer, "Erbium dopants in nanophotonic silicon waveguides," *Optica*, vol. 8, no. 1, pp. 40–41, 2021.

[4] M. J. Shaw, J. Guo, G. A. Vawter, S. Habermehl, and C. T. Sullivan, "Fabrication techniques for low-loss silicon nitride waveguides," in *Micromachining Technology for Micro-Optics and Nano-Optics III*, International Society for Optics and Photonics, vol. 5720, 2005, pp. 109–118.

[5] D. T. Spencer, J. F. Bauters, M. J. Heck, and J. E. Bowers, "Integrated waveguide coupled si 3 n 4 resonators in the ultrahigh-q regime," *Optica*, vol. 1, no. 3, pp. 153–157, 2014.

[6] Y. Xuan, Y. Liu, L. T. Varghese, *et al.*, "High-q silicon nitride microresonators exhibiting low-power frequency comb initiation," *Optica*, vol. 3, no. 11, pp. 1171–1180, 2016.

[7] R. Weis and T. Gaylord, "Lithium niobate: Summary of physical properties and crystal structure," *Applied Physics A*, vol. 37, no. 4, pp. 191–203, 1985.

[8] H. Liang, R. Luo, Y. He, H. Jiang, and Q. Lin, "High-quality lithium niobate photonic crystal nanocavities," *Optica*, vol. 4, no. 10, pp. 1251–1258, 2017.

[9] K. Luke, P. Kharel, C. Reimer, L. He, M. Loncar, and M. Zhang, "Wafer-scale low-loss lithium niobate photonic integrated circuits," *arXiv preprint arXiv:2007.06498*, 2020.

[10] E. Saglamyurek, N. Sinclair, J. Jin, *et al.*, "Broadband waveguide quantum memory for entangled photons," *Nature*, vol. 469, no. 7331, pp. 512–515, 2011.

[11] J. Lu, A. Al Sayem, Z. Gong, J. B. Surya, C.-L. Zou, and H. X. Tang, "Ultralow-threshold thin-film lithium niobate optical parametric oscillator," *Optica*, vol. 8, no. 4, pp. 539–544, 2021.

[12] J. Ilves, S. Kono, Y. Sunada, *et al.*, "On-demand generation and characterization of a microwave time-bin qubit," *npj Quantum Information*, vol. 6, no. 1, pp. 1–7, 2020.

[13] E. Saglamyurek, J. Jin, V. B. Verma, *et al.*, "Quantum storage of entangled telecom-wavelength photons in an erbium-doped optical fibre," *Nature Photonics*, vol. 9, no. 2, pp. 83–87, 2015.

[14] A.-B. Mohamed and N. Metwally, "Enhancing non-local correlations in a dissipative two-qubit system via dipole–dipole interplay," *Quantum Information Processing*, vol. 18, no. 3, p. 79, 2019.

[15] T. Northup and R. Blatt, "Quantum information transfer using photons," *Nature photonics*, vol. 8, no. 5, pp. 356–363, 2014.

[16] C. L. Degen, F. Reinhard, and P. Cappellaro, "Quantum sensing," *Reviews of modern physics*, vol. 89, no. 3, p. 035 002, 2017.

[17] W. Munro, K. Harrison, A. Stephens, S. Devitt, and K. Nemoto, "From quantum multiplexing to high-performance quantum networking," *Nature Photonics*, vol. 4, no. 11, pp. 792–796, 2010.

[18] M. Zhong, M. P. Hedges, R. L. Ahlefeldt, *et al.*, "Optically addressable nuclear spins in a solid with a six-hour coherence time," *Nature*, vol. 517, no. 7533, pp. 177–180, 2015.

[19] M. Afzelius and C. Simon, "Impedance-matched cavity quantum memory," *Physical Review A*, vol. 82, no. 2, p. 022 310, 2010.

[20] M. P. Hedges, J. J. Longdell, Y. Li, and M. J. Sellars, "Efficient quantum memory for light," *Nature*, vol. 465, no. 7301, pp. 1052–1056, 2010.

[21] T. Zhong, J. M. Kindem, J. Rochman, and A. Faraon, "Interfacing broadband photonic qubits to on-chip cavity-protected rare-earth ensembles," *Nature communications*, vol. 8, no. 1, pp. 1–7, 2017.

[22] A. Walther, *Coherent processes in rare-earth-ion-doped solids*. Lund University, 2009.

[23] S. Probst, *Hybrid quantum system based on rare earth doped crystals*. KIT Scientific Publishing, 2016, vol. 16.

[24] A. Ortu, A. Tiranov, S. Welinski, *et al.*, "Simultaneous coherence enhancement of optical and microwave transitions in solid-state electronic spins," *Nature materials*, vol. 17, no. 8, pp. 671–675, 2018.

[25] J. G. Bartholomew, J. Rochman, T. Xie, *et al.*, "On-chip coherent microwave-to-optical transduction mediated by ytterbium in yvo 4," *Nature Communications*, vol. 11, no. 1, pp. 1–6, 2020.

[26] M. Raha, S. Chen, C. M. Phenicie, S. Ourari, A. M. Dibos, and J. D. Thompson, "Optical quantum nondemolition measurement of a single rare earth ion qubit," *Nature communications*, vol. 11, no. 1, pp. 1–6, 2020.

[27] E. T. Miyazono, "Nanophotonic resonators for optical quantum memories based on rare-earth-doped materials," Ph.D. dissertation, California Institute of Technology, 2017.

[28] M. Zhang, C. Wang, R. Cheng, A. Shams-Ansari, and M. Lončar, "Monolithic ultra-high-q lithium niobate microring resonator," *Optica*, vol. 4, no. 12, pp. 1536–1537, 2017.

[29] D. Genov, R. Oulton, G. Bartal, and X. Zhang, "Anomalous spectral scaling of light emission rates in low-dimensional metallic nanostructures," *Physical Review B*, vol. 83, no. 24, p. 245 312, 2011.

[30] D. Ding, L. M. Pereira, J. F. Bauters, *et al.*, "Multidimensional purcell effect in an ytterbium-doped ring resonator," *Nature Photonics*, vol. 10, no. 6, p. 385, 2016.

[31] R. Brundage and W. Yen, "Low-temperature homogeneous linewidths of yb 3+ in inorganic glasses," *Physical Review B*, vol. 33, no. 6, p. 4436, 1986.

[32] Y. Gong, M. Makarova, S. Yerci, *et al.*, "Linewidth narrowing and purcell enhancement in photonic crystal cavities on an er-doped silicon nitride platform," *Optics express*, vol. 18, no. 3, pp. 2601–2612, 2010.

[33] T. Zhong, J. M. Kindem, E. Miyazono, and A. Faraon, "Nanophotonic coherent light–matter interfaces based on rare-earth-doped crystals," *Nature communications*, vol. 6, no. 1, pp. 1–6, 2015.

[34] T. Zhong, J. M. Kindem, J. G. Bartholomew, *et al.*, "Optically addressing single rare-earth ions in a nanophotonic cavity," *Physical review letters*, vol. 121, no. 18, p. 183 603, 2018.

[35] M. Bruel, "Silicon on insulator material technology," *Electronics letters*, vol. 31, no. 14, pp. 1201–1202, 1995.

[36] G. Poberaj, H. Hu, W. Sohler, and P. Guenter, "Lithium niobate on insulator (lnoi) for micro-photonic devices," *Laser & photonics reviews*, vol. 6, no. 4, pp. 488–503, 2012.

[37] W. Bogaerts, P. De Heyn, T. Van Vaerenbergh, *et al.*, "Silicon microring resonators," *Laser & Photonics Reviews*, vol. 6, no. 1, pp. 47–73, 2012.

[38] J. Heebner, R. Grover, and T. Ibrahim, *Optical microresonator theory*. Springer, 2008.

[39] M. Borselli, T. J. Johnson, and O. Painter, "Beyond the rayleigh scattering limit in high-q silicon microdisks: Theory and experiment," *Optics express*, vol. 13, no. 5, pp. 1515–1530, 2005.

[40] K. Sugii, M. Fukuma, and H. Iwasaki, "A study on titanium diffusion into linbo 3 waveguides by electron probe analysis and x-ray diffraction methods," *Journal of Materials Science*, vol. 13, no. 3, pp. 523–533, 1978.

[41] J. Jones, J. De Sandro, M. Hempstead, *et al.*, "Channel waveguide laser at 1 μm in yb-indiffused linbo 3," *Optics letters*, vol. 20, no. 13, pp. 1477–1479, 1995.

[42] D. Pak, H. An, A. Nandi, X. Jiang, Y. Xuan, and M. Hosseini, "Ytterbium-implanted photonic resonators based on thin film lithium niobate," *Journal of Applied Physics*, vol. 128, no. 8, p. 084 302, 2020.

[43] S. A. Campbell, *Fabrication engineering at the micro-and nanoscale*, Sirsi) i9780195320176. 2008.

[44] R. E. Evans, M. K. Bhaskar, D. D. Sukachev, *et al.*, "Photon-mediated interactions between quantum emitters in a diamond nanocavity," *Science*, vol. 362, no. 6415, pp. 662–665, 2018.

[45] A. Nandi, X. Jiang, D. Pak, *et al.*, "Controlling light emission by engineering atomic geometries in silicon photonics," *Optics Letters*, vol. 45, no. 7, pp. 1631–1634, 2020.

[46] A. J. Freeman and R. Watson, "Theoretical investigation of some magnetic and spectroscopic properties of rare-earth ions," *Physical Review*, vol. 127, no. 6, p. 2058, 1962.

[47] J. H. Wesenberg, K. Mølmer, L. Rippe, and S. Kröll, "Scalable designs for quantum computing with rare-earth-ion-doped crystals," *Physical Review A*, vol. 75, no. 1, p. 012 304, 2007.

[48] C. Thiel, T. Böttger, and R. Cone, "Rare-earth-doped materials for applications in quantum information storage and signal processing," *Journal of luminescence*, vol. 131, no. 3, pp. 353–361, 2011.

[49] N. Gisin and R. Thew, "Quantum communication," *Nature photonics*, vol. 1, no. 3, p. 165, 2007.

[50] X. Jiang, D. Pak, A. Nandi, Y. Xuan, and M. Hosseini, "Rare earth-implanted lithium niobate: Properties and on-chip integration," *Applied Physics Letters*, vol. 115, no. 7, p. 071 104, 2019.

[51] S. Romero-García, F. Merget, F. Zhong, H. Finkelstein, and J. Witzens, "Silicon nitride cmos-compatible platform for integrated photonics applications at visible wavelengths," *Optics express*, vol. 21, no. 12, pp. 14 036–14 046, 2013.

[52] J. S. Levy, A. Gondarenko, M. A. Foster, A. C. Turner-Foster, A. L. Gaeta, and M. Lipson, "Cmos-compatible multiple-wavelength oscillator for on-chip optical interconnects," *Nature photonics*, vol. 4, no. 1, pp. 37–40, 2010.

[53] R. Halir, Y. Okawachi, J. Levy, M. Foster, M. Lipson, and A. Gaeta, "Ultrabroadband supercontinuum generation in a cmos-compatible platform," *Optics letters*, vol. 37, no. 10, pp. 1685–1687, 2012.

[54] P. Imany, J. A. Jaramillo-Villegas, O. D. Odele, *et al.*, "50-ghz-spaced comb of high-dimensional frequency-bin entangled photons from an on-chip silicon nitride microresonator," *Optics express*, vol. 26, no. 2, pp. 1825–1840, 2018.

[55] C. Yang and J. Pham, "Characteristic study of silicon nitride films deposited by lpcvd and pecvd," *Silicon*, vol. 10, no. 6, pp. 2561–2567, 2018.

[56] J. Wang, Y. Xuan, C. Lee, *et al.*, "Low-loss and misalignment-tolerant fiber-to-chip edge coupler based on double-tip inverse tapers," in *2016 Optical Fiber Communications Conference and Exhibition (OFC)*, IEEE, 2016, pp. 1–3.

[57] M. Sabooni, Q. Li, S. Kröll, and L. Rippe, "Efficient quantum memory using a weakly absorbing sample," *Physical review letters*, vol. 110, no. 13, p. 133 604, 2013.

[58] R. Macfarlane and R. Shelby, "Coherent transient and holeburning spectroscopy of rare earth ions in solids," in *Modern Problems in Condensed Matter Sciences*, vol. 21, Elsevier, 1987, pp. 51–184.

[59] A. Dibos, M. Raha, C. Phenicie, and J. D. Thompson, "Atomic source of single photons in the telecom band," *Physical review letters*, vol. 120, no. 24, p. 243 601, 2018.

[60] J. M. Kindem, A. Ruskuc, J. G. Bartholomew, J. Rochman, Y. Q. Huan, and A. Faraon, "Control and single-shot readout of an ion embedded in a nanophotonic cavity," *Nature*, pp. 1–4, 2020.

[61] O. Alibart, V. D'Auria, M. De Micheli, *et al.*, "Quantum photonics at telecom wavelengths based on lithium niobate waveguides," *Journal of Optics*, vol. 18, no. 10, p. 104 001, 2016.

[62] G. Griffiths and R. Esdaile, "Analysis of titanium diffused planar optical waveguides in lithium niobate," *IEEE Journal of Quantum electronics*, vol. 20, no. 2, pp. 149–159, 1984.

[63] S. Mailis, C. Riziotis, I. Wellington, P. Smith, C. Gawith, and R. Eason, "Direct ultraviolet writing of channel waveguides in congruent lithium niobate single crystals," *Optics Letters*, vol. 28, no. 16, pp. 1433–1435, 2003.

[64] D. Pak, A. Nandi, X. Jiang, *et al.*, "Integration of rare earth ions and photonic resonators for quantum application," in *CLEO: QELS_Fundamental Science*, Optical Society of America, 2020, FW3C–2.

[65] J. Lu, J. B. Surya, X. Liu, *et al.*, "Periodically poled thin-film lithium niobate microring resonators with a second-harmonic generation efficiency of 250,000%/w," *Optica*, vol. 6, no. 12, pp. 1455–1460, 2019.

[66] L. Shao, M. Yu, S. Maity, *et al.*, "Microwave-to-optical conversion using lithium niobate thin-film acoustic resonators," *Optica*, vol. 6, no. 12, pp. 1498–1505, 2019.

[67] J.-Y. Chen, Z.-H. Ma, Y. M. Sua, Z. Li, C. Tang, and Y.-P. Huang, "Ultra-efficient frequency conversion in quasi-phase-matched lithium niobate microrings," *Optica*, vol. 6, no. 9, pp. 1244–1245, 2019.

[68] S. Wang, L. Yang, R. Cheng, *et al.*, "Incorporation of erbium ions into thin-film lithium niobate integrated photonics," *Applied Physics Letters*, vol. 116, no. 15, p. 151 103, 2020.

[69] S. Dutta, E. A. Goldschmidt, S. Barik, U. Saha, and E. Waks, "An integrated photonic platform for rare-earth ions in thin film lithium niobate," *Nano Letters*, 2019.

[70] B. Desiatov, A. Shams-Ansari, M. Zhang, C. Wang, and M. Lončar, "Ultra-low-loss integrated visible photonics using thin-film lithium niobate," *Optica*, vol. 6, no. 3, pp. 380–384, 2019.

[71] M. Bahadori, Y. Yang, L. L. Goddard, and S. Gong, "High performance fully etched isotropic microring resonators in thin-film lithium niobate on insulator platform," *Optics express*, vol. 27, no. 15, pp. 22 025–22 039, 2019.

[72] Y. He, Q.-F. Yang, J. Ling, *et al.*, "Self-starting bi-chromatic linbo 3 soliton microcomb," *Optica*, vol. 6, no. 9, pp. 1138–1144, 2019.

[73] T. Böttger, C. Thiel, Y. Sun, and R. Cone, "Optical decoherence and spectral diffusion at 1.5 μ m in er 3+: Y 2 sio 5 versus magnetic field, temperature, and er 3+ concentration," *Physical Review B*, vol. 73, no. 7, p. 075 101, 2006.

[74] A. Polman, "Erbium implanted thin film photonic materials," *Journal of applied physics*, vol. 82, no. 1, pp. 1–39, 1997.

[75] S. Li, L. Cai, Y. Wang, Y. Jiang, and H. Hu, "Waveguides consisting of single-crystal lithium niobate thin film and oxidized titanium stripe," *Optics express*, vol. 23, no. 19, pp. 24 212–24 219, 2015.

[76] C. Wang, M. Zhang, B. Stern, M. Lipson, and M. Lončar, "Nanophotonic lithium niobate electro-optic modulators," *Optics express*, vol. 26, no. 2, pp. 1547–1555, 2018.

[77] K. Furuya, A. Nandi, and M. Hosseini, "Study of atomic geometry and its effect on photon generation and storage [invited]," *Opt. Mater. Express*, vol. 10, no. 2, pp. 577–587, Feb. 2020. DOI: 10.1364/OME.380715. [Online]. Available: http://www.osapublishing.org/ome/abstract.cfm?URI=ome-10-2-577.

[78] A. Sipahigil, R. E. Evans, D. D. Sukachev, *et al.*, "An integrated diamond nanophotonics platform for quantum-optical networks," *Science*, vol. 354, no. 6314, pp. 847–850, 2016.

[79] A. Asenjo-Garcia, M. Moreno-Cardoner, A. Albrecht, H. Kimble, and D. E. Chang, "Exponential improvement in photon storage fidelities using subradiance and "selective radiance" in atomic arrays," *Physical Review X*, vol. 7, no. 3, p. 031 024, 2017.

[80] D. E. Chang, L. Jiang, A. Gorshkov, and H. Kimble, "Cavity qed with atomic mirrors," *New Journal of Physics*, vol. 14, no. 6, p. 063 003, 2012.

[81] S. J. Masson and A. Asenjo-Garcia, "Atomic-waveguide quantum electrodynamics," *Physical Review Research*, vol. 2, no. 4, p. 043 213, 2020.

[82] M. A. Norcia, M. N. Winchester, J. R. Cline, and J. K. Thompson, "Superradiance on the millihertz linewidth strontium clock transition," *Science advances*, vol. 2, no. 10, e1601231, 2016.

[83] C. Bradac, M. T. Johnsson, M. van Breugel, *et al.*, "Room-temperature spontaneous superradiance from single diamond nanocrystals," *Nature communications*, vol. 8, no. 1, pp. 1–6, 2017.

[84] M. Scheibner, T. Schmidt, L. Worschech, *et al.*, "Superradiance of quantum dots," *Nature Physics*, vol. 3, no. 2, pp. 106–110, 2007.

[85] R. Macfarlane, R. Meltzer, and B. Malkin, "Optical measurement of the isotope shifts and hyperfine and superhyperfine interactions of nd in the solid state," *Physical Review B*, vol. 58, no. 9, p. 5692, 1998.

[86] R. Ahlefeldt, M. R. Hush, and M. Sellars, "Ultranarrow optical inhomogeneous linewidth in a stoichiometric rare-earth crystal," *Physical review letters*, vol. 117, no. 25, p. 250 504, 2016.

[87] M. Rančić, M. P. Hedges, R. L. Ahlefeldt, and M. J. Sellars, "Coherence time of over a second in a telecom-compatible quantum memory storage material," *Nature Physics*, vol. 14, no. 1, pp. 50–54, 2018.

[88] T. Zhong, J. M. Kindem, J. G. Bartholomew, *et al.*, "Nanophotonic rare-earth quantum memory with optically controlled retrieval," *Science*, vol. 357, no. 6358, pp. 1392–1395, 2017.

[89] S. Chen, M. Raha, C. M. Phenicie, S. Ourari, and J. D. Thompson, "Parallel single-shot measurement and coherent control of solid-state spins below the diffraction limit," *Science*, vol. 370, no. 6516, pp. 592–595, 2020.

[90] A. Gritsch, L. Weiss, J. Früh, S. Rinner, and A. Reiserer, "Narrow optical transitions in erbium-implanted silicon waveguides," *arXiv preprint arXiv:2108.05120*, 2021.

[91] C. M. Phenicie, P. Stevenson, S. Welinski, *et al.*, "Narrow optical line widths in erbium implanted in tio2," *Nano letters*, vol. 19, no. 12, pp. 8928–8933, 2019.

[92] X. Guo, C.-l. Zou, C. Schuck, H. Jung, R. Cheng, and H. X. Tang, "Parametric down-conversion photon-pair source on a nanophotonic chip," *Light: Science & Applications*, vol. 6, no. 5, e16249–e16249, 2017.

[93] C. Wang, M. Zhang, X. Chen, *et al.*, "Integrated lithium niobate electro-optic modulators operating at cmos-compatible voltages," *Nature*, vol. 562, no. 7725, pp. 101–104, 2018.

[94] K. Furuya, A. Nandi, and M. Hosseini, "Study of atomic geometry and its effect on photon generation and storage," *Optical Materials Express*, vol. 10, no. 2, pp. 577–587, 2020.

[95] G. Ferioli, A. Glicenstein, L. Henriet, I. Ferrier-Barbut, and A. Browaeys, "Storage and release of subradiant excitations in a dense atomic cloud," *Physical Review X*, vol. 11, no. 2, p. 021 031, 2021.

[96] D. Zhu, L. Shao, M. Yu, *et al.*, "Integrated photonics on thin-film lithium niobate," *Advances in Optics and Photonics*, vol. 13, no. 2, pp. 242–352, 2021.

[97] N. Sinclair, D. Oblak, E. Saglamyurek, R. L. Cone, C. W. Thiel, and W. Tittel, "Optical coherence and energy-level properties of a tm 3+-doped li nb o 3 waveguide at subkelvin temperatures," *Physical Review B*, vol. 103, no. 13, p. 134 105, 2021.

[98] L. Henriet, J. S. Douglas, D. E. Chang, and A. Albrecht, "Critical open-system dynamics in a one-dimensional optical-lattice clock," *Physical Review A*, vol. 99, no. 2, p. 023 802, 2019.

[99] J. Perczel, J. Borregaard, D. E. Chang, *et al.*, "Topological quantum optics in two-dimensional atomic arrays," *Physical review letters*, vol. 119, no. 2, p. 023 603, 2017.

[100] A. Cipris, N. Moreira, T. do Espirito Santo, *et al.*, "Subradiance with saturated atoms: Population enhancement of the long-lived states," *Physical Review Letters*, vol. 126, no. 10, p. 103 604, 2021.

[101] W. Guerin and R. Kaiser, "Population of collective modes in light scattering by many atoms," *Physical Review A*, vol. 95, no. 5, p. 053 865, 2017.

[102] Y.-X. Zhang and K. Mølmer, "Theory of subradiant states of a one-dimensional two-level atom chain," *Physical review letters*, vol. 122, no. 20, p. 203 605, 2019.

[103] P. Solano, P. Barberis-Blostein, F. K. Fatemi, L. A. Orozco, and S. L. Rolston, "Super-radiance reveals infinite-range dipole interactions through a nanofiber," *Nature communications*, vol. 8, no. 1, pp. 1–7, 2017.

[104] M. Reitz, C. Sommer, and C. Genes, "Cooperative quantum phenomena in light-matter platforms," *PRX Quantum*, vol. 3, p. 010 201, 1 Jan. 2022. DOI: 10.1103/PRXQuantum.3.010201. [Online]. Available: https://link.aps.org/doi/10.1103/PRXQuantum.3.010201.

[105] A. Glicenstein, G. Ferioli, A. Browaeys, and I. Ferrier-Barbut, "From superradiance to subradiance: Exploring the many-body dicke ladder," *arXiv preprint arXiv:2112.10635*, 2021.

[106] D. Das, B. Lemberger, and D. Yavuz, "Subradiance and superradiance-to-subradiance transition in dilute atomic clouds," *Physical Review A*, vol. 102, no. 4, p. 043 708, 2020.

[107] S. Slama, C. Von Cube, M. Kohler, C. Zimmermann, and P. W. Courteille, "Multiple reflections and diffuse scattering in bragg scattering at optical lattices," *Physical Review A*, vol. 73, no. 2, p. 023 424, 2006.

[108] Y. Sun, C. Thiel, and R. Cone, "Optical decoherence and energy level structure of 0.1% tm 3+: Linbo 3," *Physical Review B*, vol. 85, no. 16, p. 165 106, 2012.

[109] C. Thiel, Y. Sun, T. Böttger, W. Babbitt, and R. Cone, "Optical decoherence and persistent spectral hole burning in tm3+: Linbo3," *Journal of luminescence*, vol. 130, no. 9, pp. 1598–1602, 2010.

[110] E. Kustov, V. Loschenov, and I. Basieva, "Decay times of radiative and non-radiative transitions in rare-earth ions," *Physica Scripta*, vol. 2014, no. T163, p. 014 032, 2014.

[111] M. Weber, "Radiative and multiphonon relaxation of rare-earth ions in y *sub*2 o.," Raytheon Research Div., Waltham, Mass., Tech. Rep., 1968.

[112] D. Sumida and T. Fan, "Effect of radiation trapping on fluorescence lifetime and emission cross section measurements in solid-state laser media," *Optics Letters*, vol. 19, no. 17, pp. 1343–1345, 1994.

[113] R. H. Dicke, "Coherence in spontaneous radiation processes," *Physical review*, vol. 93, no. 1, p. 99, 1954.

[114] J. W. Czarnik and P. R. Fontana, "Resonance radiation from interacting atoms," *The Journal of Chemical Physics*, vol. 50, no. 9, pp. 4071–4074, 1969.

[115] T. Shahbazyan, M. Raikh, and Z. Vardeny, "Mesoscopic cooperative emission from a disordered system," *Physical Review B*, vol. 61, no. 19, p. 13 266, 2000.

[116] B. C. Rose, D. Huang, Z.-H. Zhang, *et al.*, "Observation of an environmentally insensitive solid-state spin defect in diamond," *Science*, vol. 361, no. 6397, pp. 60–63, 2018.

[117] H. Sørensen, J.-B. Béguin, K. Kluge, *et al.*, "Coherent backscattering of light off one-dimensional atomic strings," *Physical review letters*, vol. 117, no. 13, p. 133 604, 2016.

[118] N. V. Corzo, B. Gouraud, A. Chandra, *et al.*, "Large bragg reflection from one-dimensional chains of trapped atoms near a nanoscale waveguide," *Physical review letters*, vol. 117, no. 13, p. 133 603, 2016.

[119] A. Albrecht, L. Henriet, A. Asenjo-Garcia, P. B. Dieterle, O. Painter, and D. E. Chang, "Subradiant states of quantum bits coupled to a one-dimensional waveguide," *New Journal of Physics*, vol. 21, no. 2, p. 025 003, 2019.

[120] J. Zhong, N. A. Olekhno, Y. Ke, *et al.*, "Photon-mediated localization in two-level qubit arrays," *Physical review letters*, vol. 124, no. 9, p. 093 604, 2020.

[121] Y. Ke, A. V. Poshakinskiy, C. Lee, Y. S. Kivshar, and A. N. Poddubny, "Inelastic scattering of photon pairs in qubit arrays with subradiant states," *Physical review letters*, vol. 123, no. 25, p. 253 601, 2019.

[122] E. Miyazono, I. Craiciu, A. Arbabi, T. Zhong, and A. Faraon, "Coupling erbium dopants in yttrium orthosilicate to silicon photonic resonators and waveguides," *Optics express*, vol. 25, no. 3, pp. 2863–2871, 2017.

[123] M. Mirhosseini, A. Sipahigil, M. Kalaee, and O. Painter, "Superconducting qubit to optical photon transduction," *Nature*, vol. 588, no. 7839, pp. 599–603, 2020.

VITA

Dongmin Pak was born in Daegu, South Korea in Jan, 1991. He received his Bachelor of Science degree in Electrical Engineering at the University of Texas at Dallas in Dec, 2015. He joined the Elmore Family School of Electrical and Computer Engineering at Purdue University for his Ph.D. studies in Aug, 2016. He had worked with Professor Mahdi Hosseini on fabricaiton and characterization of rare-earth ions in solid host materials such as silicon/silicon nitride and lithium niobate for 5 years before he graduated with a Ph.D. degree in Electrical and Computer Engineering at Purdue University in May, 2022.

PUBLICATIONS

D. Pak, A. Nandi, M. Titze, E.S. Bielejec, H. Alaeian, M. Hosseini, "Long-range cooperative resonances in rare-earth ion arrays inside photonic resonators" *Communications Physics*, 5, 89 (2022).

Y. Xuan, S. Ghatak, A. Clark, Z. Li, S. Khanna, **D. Pak**, M. Agarwal, S. Roy, P. Duda, C.K. Sen, "Fabrication and use of silicon hollow-needle arrays to achieve tissue nanotransfection in mouse tissue in vivo" *Nature Protocols*, Vol. 16, Issue 12, pp. 5707-5738 (2021).

D. Pak, A. Nandi, M. Titze, E.S. Bielejec, M. Hosseini, "Optical Properties of Rare Earth Ion Arrays Embedded into Lithium Niobate Micro-ring Resonators" *2021 IEEE Photonics Conference (IPC).*

D. Pak, H. An, A. Nandi, X. Jiang, Y. Xuan, M. Hosseini, "Ytterbium-implanted photonic resonators based on thin film lithium niobate" *Journal of Applied Physics*, 128, 084302 (2020).

D. Pak, H. An, X. Jiang, A. Nandi, Y. Xuan, M. Hosseini, "Ytterbium implanted lithium niobate ring resonators on insulator: Fabrication and Characterization" *2020 IEEE Photonics Conference (IPC).*

D. Pak, A. Nandi, X. Jiang, D. Perry, E. S. Bielejec, Y. Xuan, M. Hosseini, "Integration of rare earth ions and photonic resonators for quantum application" *2020 CLEO*, FW3C-2.

A. Nandi, X. Jiang, **D. Pak**, D. Perry, K. Han, E. S. Bielejec, Y. Xuan, M. Hosseini, "Controlling light emission by engineering atomic geometries in silicon photonics" *Optics Letters*, Vol. 45, Issue 7, pp. 1631-1634 (2020).

X. Jiang, **D. Pak**, A. Nandi, Y. Xuan, M. Hosseini, "Rare earth-implanted lithium niobate: Properties and on-chip integration" *Applied Physics Letters*, 115,071104 (2019).

X. Jiang, A. Nandi, **D. Pak**, M. Hosseini, "Optomechanical frequency comb memory" *Optics Letters*, Vol. 43, Issue 20, pp. 4973-4976 (2018).